HOKKAIDO UNIVERSITY

Title	Preparation of Electrocatalysts by Bottom-up Methods for Fuel Cell Reactions
Author(s)	,
Citation	. ( ) 11139
Issue Date	2013-09-25
DOI	10.14943/doctoral.k11139
Doc URL	http://hdl.handle.net/2115/56994
Type	theses (doctoral)
File Information	Yukihisa_Okawa.pdf

Instructions for use

Preparation of Electrocatalysts by Bottom-up Methods

for Fuel Cell Reactions

(ボトムアップ法による燃料電池電極触媒の作製)

Yukihisa Okawa

Interfacial Energy Conversion Materials Chemistry Laboratory
Graduate School of Chemical Sciences and Engineering
Hokkaido University

2013

Acknowledgments

I would like to express my sincerest appreciation to my supervisor, Professor Kohei Uosaki for his invaluable suggestion, encouragement, and continuous support throughout the course of this work.

I am also grateful to Professors Kei Murakoshi, Masako Kato, and Hiroki Habazaki for their valuable advices and comments on this dissertation.

I am deeply grateful to Professor Hidenori Noguchi for his advice, guidance, and encouragement throughout this study.

I would like to express my appreciation to Dr. Takuya Masuda for his advice, discussion and assistance.

I am grateful to Associate Professors Katsuyoshi Ikeda and Satoru Takakusagi for their advices and encouragements. Appreciation continues to Drs. Hiromitsu Uehara, Mikio Ito, Hidehiko Asanuma, Satoshi Tominaka, Ying Han, and Hitoshi Fukumitsu for their advices and discussions.

I also would like to express grateful thanks to the colleagues in Physical Chemistry and Interfacial Energy Conversion Materials Chemistry Laboratories in Hokkaido University and Electrochemical Surface Science Laboratory in National Institute for Materials Science. It was my great pleasure to work together with Messrs. Shuto Suzuki, Tariho Hayashi, and Yusuke Waki. I am thankful to their friendship and encouragements. Administrative supports by Mses. Yuko Asano, Kyoko Okada, and Rumiko Enjoji are gratefully acknowledged.

The financial supports from the Global COE Program, "Catalysis as the Basis for Innovation in Materials Science" from the Ministry of Education, Culture, Sports, Science and Technology, Japan and Internship Program of National Institute for Materials Science are gratefully acknowledged.

Finally, I would like to thank my parents for their encouragements and supports through my study.

Yukihisa Okawa

Tsukuba

September, 2013.

CONTENTS

Standard Abbreviations

CV: cyclic voltammogram

LSV: linear sweep voltammogram

RDE: rotating disk electrode

HMRDE: hanging meniscus rotating disk electrode

STM: scanning tunneling microscopy

XPS: X-ray photoelectron spectroscopy

XAFS: X-ray adsorption fine structure

XANES: X-ray absorption near edge structure

EXAFS: extended X-ray absorption fine structure

RDF: radial distribution function

WL: white line

PEFC: polymer electrolyte fuel cell

DMFC: direct methanol fuel cell

SHE: standard hydrogen electrode

HOR: hydrogen oxidation reaction

HER: hydrogen evolution reaction

MOR: methanol oxidation reaction

ORR: oxygen reduction reaction

OER: oxygen evolution reaction

Chapter 1

INTRODUCTION

1.1 General Introduction

Fuel cell systems can be leading energy conversion systems in future because they are expected to overcome the anticipated problems such as shortage of fossil fuels and increase of electricity usage and create the society based on environmentally-preferable, convenient, sustainable, and flexible electricity generation systems.[1-4] They show advantages in terms of energy conversion efficiency as chemical energy is converted into electronic energy directly through electrochemical reactions and such energy conversion does not go through energy forms such as thermal and kinetic energy. Therefore, their energy conversion efficiency can be higher than the energy conversion efficiency of the thermal power energy generation systems whose maximum energy conversion efficiencies are limited by Carnot's rule. The energy conversion efficiency of fuel cell systems does not depend on their size. They can work quieter and generate less toxic materials and their size and location are more flexible than those of thermal power generation systems.

Among the various fuel cell systems, molten carbonate fuel cell (MCFC), solid oxide fuel cell (SOFC), phosphoric acid fuel cell (PAFC) and polymer electrolyte fuel cell (PEFC) have been intensively studied. The MCFC and SOFC work at so high temperature that fuels are easily reacted without precious catalyst such as Pt. The PAFC works at around 200 ℃ and requires Pt as an electrocatalyst. The MCFC, SOFC and PAFC show relatively high energy conversion efficiencies and they have started to be used for the electricity-generation systems. Compared with these fuel cell systems, PEFC systems can work at relatively low temperature and be used as the power source of machines in daily life such as automobiles, laptops and mobiles.[1] Figure 1-1 shows schematic of PEFC systems. PEFC systems are mainly composed of anode, cathode, gas diffusion layer and ion exchange membrane. The ion exchange membrane which is required to show thermal and chemical stability, high proton conductivity and low electron conductivity permeability

to gases allows generated proton to move cathode.[5] PEFC systems generate electricity through electrochemical oxidation reaction of fuels such as hydrogen and organic molecules and reduction reaction of oxygen.

H_2–O_2 PEFC systems show high theoretical energy conversion efficiency (83 %) and high theoretical specific energy (32800 Wh kg^{-1}).[3] They are operated by the inverse reaction of electrolysis of water, i.e., hydrogen oxidation reaction (HOR) and oxygen reduction reaction (ORR). Their electrode reactions are as follows.

Anode: $\quad H_2 \rightarrow 2H^+ + 2e^-$ $\qquad\qquad E^o = 0$ V (vs. SHE) $\qquad$ (1-1)

Cathode: $\quad 1/2 O_2 + 2H^+ + 2e^- \rightarrow H_2O$ $\quad E^o = 1.23$ V (vs. SHE) $\quad$ (1-2)

Overall: $\quad H_2 + 1/2\ O_2 \rightarrow H_2O$ $\qquad\qquad\qquad\qquad$ (1-3)
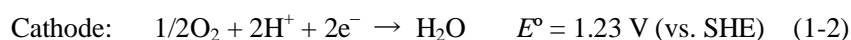
The theoretical electromotive force of the hydrogen fuel cell systems is 1.23 V. From an energetic point of view, hydrogen is more advantageous than lower alcohols and the H_2–O_2 PEFC systems show excellent performance but the difficulty of production and storage of hydrogen prevent the H_2–O_2 PEFC systems from their widespread use.

From the view point of storage and transportation of fuels, PEFC systems operated on organic molecules such as methanol, ethanol, propanol, formic acid and hydrazine are useful and are expected to be
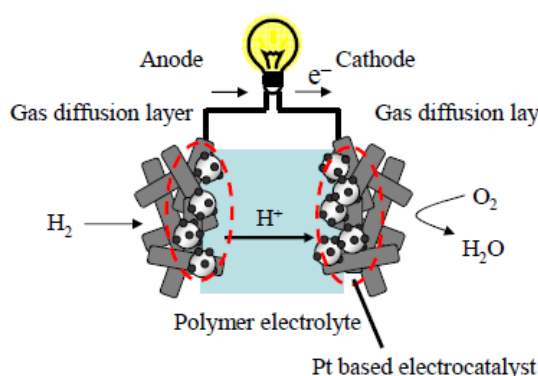
Figure 1-1. Schematic of PEFC systems.   **Figure 1-2.** I-V curve of PEFC.[7]
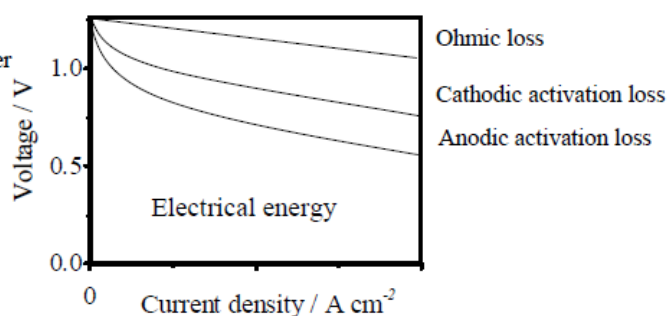
power sources of small and portable electronic devices.[3] The most common and studied fuel is methanol. PEFC systems operated on methanol are direct methanol fuel cell (DMFC) systems. Theoretical energy conversion efficiency of DMFC systems (97%) is higher than that of H_2–O_2 PEFC systems and high theoretical specific energy (6000 Wh kg^{-1}).[3] The electrode reactions of DMFC are as follows.

Anode: $CH_3OH + H_2O \rightarrow CO_2 + 6H^+ + 6e^-$ $E^o = 0.04$ V (vs. SHE)   (1-4)

Cathode: $3/2O_2 + 6H^+ + 6e^- \rightarrow 3H_2O$ $E^o = 1.23$ V (vs. SHE)   (1-5)

Overall: $CH_3OH + 3/2\ O_2 \rightarrow CO_2 + 2H_2O$ (1-6)
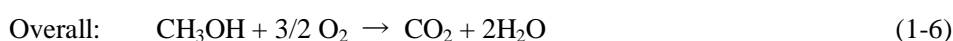
The theoretical electromotive force of the DMFC systems is 1.19 V.

At present, Pt and Pt based alloys are used as electrocatalysts for the PEFC systems as they show higher activity for HOR, methanol oxidation reaction (MOR) and ORR than other noble metals.[6] But their actual electromotive force is lower than the theoretical electromotive force because of slow kinetics even when those metals are used as electrocatalysts. Figure 1-2 shows a current-voltage curve of PEFC systems.[7] The activation loss of the anode and cathode reactions is one of the most critical problems. Furthermore, Pt is a scare and expensive element. It is necessary to prepare electrocatalysts with high activity and stability but low noble metals usage in order to overcome the problems and establish the future energy generation systems.

1.2 Hydrogen Oxidation Reaction (HOR)

Pt shows high hydrogen evolution reaction (HER) and hydrogen oxidation reaction (HOR (1-1)) activity.[8] The activity of metals is determined by the strength of adsorbate–metal interaction.[9] Trasatti et al. summarized the relationship between log i_0 (i_0 = exchange current density of HER) and the M–H bond energy, so-called volcano plot (Figure 1-3)[10] and the high activity of Pt for HER and HOR can be explained. This plot means that the data on the low M–H energy side of the volcano curve refer to rate-determining

discharge of H, while for the stronger M–H energy side they can refer to a rate-determining H desorption step. Pt which is on the top of volcano and has decent hydrogen adsorption/desorption energy shows high HER and HOR activity.

The H_2–O_2 PEFC systems are operated by reformed gas from organic molecules which contains low amount of CO. Pt surface is easily covered with CO and HOR rate will decrease due to the low amount of CO which is included in hydrogen gas.[11-13] Pt alloyed with transition metals such as Ru, Co and Ni shows high tolerance against CO.[14, 15] The valence band structure of Pt can be modified by alloying with other transition metals to reduce the interaction between Pt and CO (Figure 1-4).[15, 16] These CO tolerant catalysts are expected to be good HOR catalysts for hydrogen fuel cell systems.[15, 17]
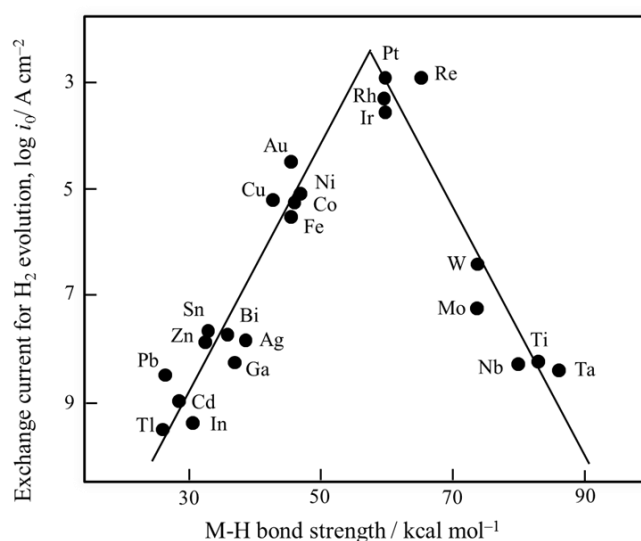
Figure 1-3. Volcano plot for log i_0 values for the HER as a function of M–H bond energy.[10]
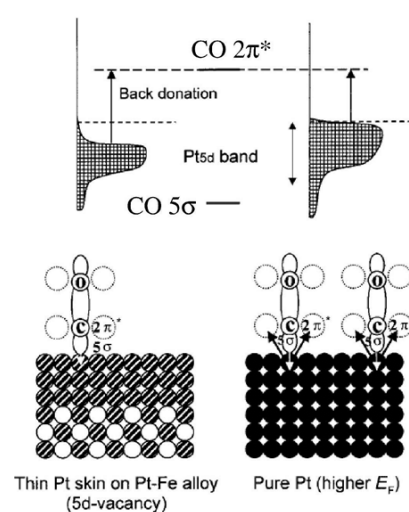
Figure 1-4. The schematic explanation of CO suppression on Pt based alloy surface.[15]

1.3   Methanol Oxidation Reaction (MOR)

1.3.1   Mechanism

Figure 1-5 shows a proposed mechanism of MOR (1-4). MOR is a complicated multielectron reaction and is initiated by the electrosorption of methanol onto the substrate, followed by the reaction with oxygen species formed from water and adsorbed carbon-containing intermediates.[18-20] The rate determining step of MOR is an oxidative desorption of CO. Pt is the best catalyst for MOR among all the elements but not to

decompose CO because the interaction between valence band of Pt (Pt $5d$ states) and the CO $2\pi^*$ and 5σ states is so strong.[21] Figure 1-6 shows a typical cyclic voltammogram (CV) of poly Pt in 0.1 M $HClO_4$ containing 1 M methanol. Kunimatsu et al. confirmed that Pt surface is covered with CO as a result of dissociative adsorption of methanol by infrared reflection absorption spectroscopy (IRRAS).[22] CO which is generated from methanol is a dominant adsorbed species and inhibits MOR on Pt at the negative potential region. After CO was oxidized, CO free Pt surface appears and MOR starts at around 0.65 V. An effective removal of CO from Pt surface at more negative potential region is important to improve not only DMFC but also H_2–O_2 PEFC performance.
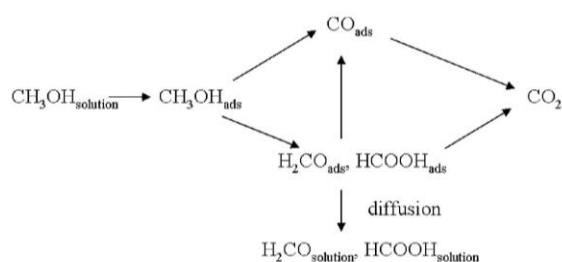
Figure 1-5. A proposed mechanism of MOR.[18-20].
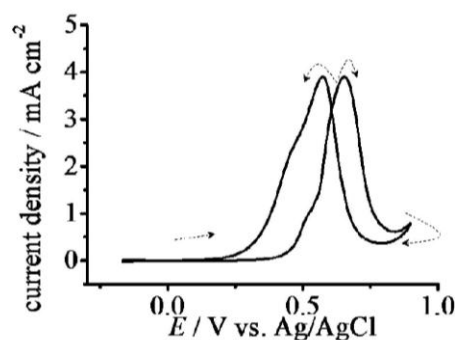
Figure 1-6. A typical CV of poly Pt in 0.1 M $HClO_4$ solution containing 1 M methanol. Scan rate = 50 mV s^{-1}.

1.3.2   MOR catalysts

The MOR activity of Pt was improved by alloying with some transition metals.[23-27] Jassen et al. prepared Pt modified with transition metals and summarized the effect of transition metals on MOR activity (Table 1-1).[28] MOR activity of Pt modified with Pd, Pb, Au etc. is lower than that of Pt. Meanwhile, MOR activity of Pt modified with Ru, Sn, Mo etc. is significantly improved.[29-31]

Table 1-1. A summary of the effect of modification of foreign metals on Pt on MOR activity.[28]

Increase	Decrease	Unchanged
Ti, Mn, Mo, Ru, Sn, Re, Os	Se, Pd, Ag, Au, Hg, Pb, Bi	Zr, Rh, W

Among Pt based alloys, Pt-Ru alloy shows high MOR activity. The structure and composition ratio of

Pt-Ru alloy surface will affect the MOR activity.[32-37] Ru which is relatively stable in electrochemical condition has high adsorption ability against oxygen species and high tolerance against CO.[36, 38, 39] It is considered that Ru acts as a MOR promoter on Pt-Ru alloy surface and MOR on Pt-Ru alloy proceeds on a bi-functional mechanism which was proposed by Watanabe and Motoo.[34, 35]

$$Pt + CH_3OH \rightarrow Pt-(CH_3OH)_{ads} \qquad (1-7)$$

$$Pt-(CH_3OH)_{ads} \rightarrow Pt-(CO)_{ads} + 4H^+ + 4e^- \qquad (1-8)$$

$$Ru + H_2O \rightarrow Ru-OH + H^+ + e^- \qquad (1-9)$$

$$Pt-(CO)_{ads} + Ru-OH \rightarrow Pt + Ru + CO_2 + H^+ + e^- \qquad (1-10)$$
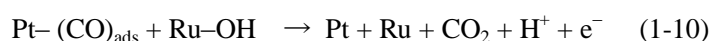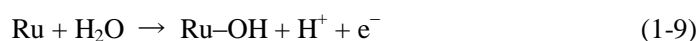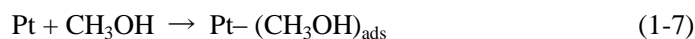
On the bi-functional mechanism, Pt acts as MOR active site and Ru supplies oxidants to assist the oxidative removal of CO adsorbed on Pt.[36, 40, 41] A randomly mixed Pt-Ru alloy at equal ratio of metals can be the most active electrocatalyst for MOR. Although randomly mixed Ag-Rh[42] and Au-Pd[43] alloys can be prepared by conventional methods such as chemical reduction and electrodeposition of metal salts (Figure 1-7), it is difficult to prepare such Pt-Ru alloy by conventional methods because of phase separation[44-46] and difficulty to control surface composition.[47-49]
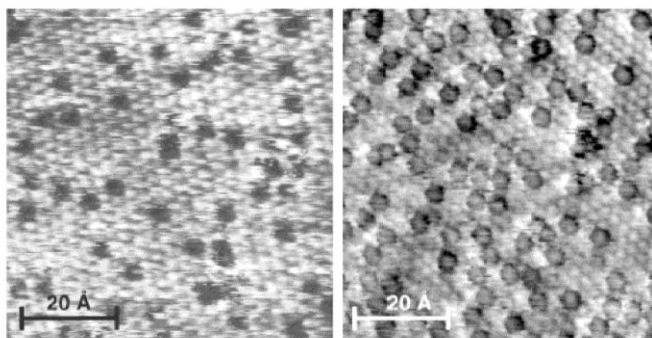
Figure 1-7. STM images of atomically mixed and ratio controlled Au-Pd surface after dissolution of Pd.[43]

1.4   Oxygen Reduction Reaction (ORR)

1.4.1   Mechanism

In aqueous solution, ORR proceeds at electrode surface by adsorption process. Oxygen can be reduced to H_2O (four electron reduction (1-11)) or H_2O_2 (two electron reduction (1-12)).

6

$$O_2 + 4H^+ + 4e^- \rightarrow 2H_2O \qquad E^\circ = 1.23 \text{ V (vs. SHE)} \qquad (1\text{-}11)$$

$$O_2 + 2H^+ + 2e^- \rightarrow H_2O_2 \qquad E^\circ = 0.68 \text{ V (vs. SHE)} \qquad (1\text{-}12)$$
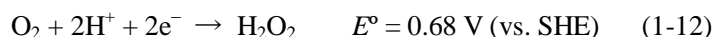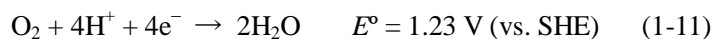
Figure 1-8 shows a proposed mechanism of ORR.[50, 51] Based on this mechanism, O_2 can be reduced to H_2O with or without formation of H_2O_2 intermediate. On Pt, the dominant product of ORR is H_2O in the electrolyte without strong adsorbates.[52-54] On less active catalyst such as Au, ORR proceeds via $2e^-$ reduction process.[55-58] Generation of H_2O_2 is undesirable because it can decrease the cell voltage and degrade the ion exchange membrane.[59] Pt is usable as ORR catalyst because Pt shows high ORR activity and produces less H_2O_2. But the ORR at Pt does not proceed well at positive potential region because the standard electrode potential of ORR via $4e^-$ reduction process is 1.23 V where Pt oxide which is inactive to ORR is formed. Adsorbed OH (OH_{ad}) on Pt also prohibits ORR. Small of interaction between Pt and OH_{ad} will decrease the over potential of ORR.
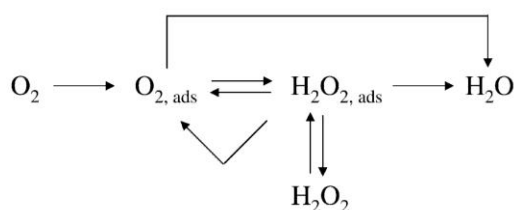
Figure 1-8. A proposed mechanism of ORR.[48, 49]

1.4.2　　ORR catalysts

1.4.2.1　　Noble metal catalysts

It has been reported that various materials and molecules show ORR activity. The ORR active materials and molecules are summarized in Table 1-2.

ORR activity is sensitive to crystal faces and ions in electrolyte solutions.[52-54, 60-62] Controlling the size and shape of Pt nanoparticles leads to improve ORR activity. Wang et al. prepared highly active ORR

Table 1-2. Summary of the ORR active catalysts.

Category		Example/Preparation Method
Pt	Size controlled Pt	Chemical reduction[64]
	Shape controlled Pt	Chemical reduction[63]
	Pt on foreign metals	Pt on noble metals/Galvanic displacement[81]
Pt based alloys	Core/shell structure	Pt-Co, Pt-Ni, Pt-Fe/Sputtering and electrochemical treatment[67]
Pt with metal oxides		Pt-CeO$_x$/Chemical reduction[82] Pt-NbO$_2$/Chemical reduction[83]
Pd	Pd on foreign metals	Pd on Au/Electrodeposition[55, 76]
Pd based alloys	Core/shell structure	Pd-Co alloy/Galvanic displacement[79] Pd-Co and Pd-Ti alloy/Sputtering and electrochemical treatmentt[74, 75]
Other metals	Metal thin film	Tl on Au(111)/Electrodeposition[56]
	Less noble metal	Ag nanoparticle/Chemical reduction[58] (alkaline solution)
Metal complex	Porphyrin	Co and Fe porphyrin/Synthesis[84, 86]
	Phthalocyanine	Co and Fe phthalocyanine/Synthesis[88]
	Others	Cu complex with triazole ligands/Synthesis[87]
N-doped carbon materials with transition metals (Fe, Co)		Decomposition of a mixture of metal salts and organic materials[90-94]
N-doped carbon materials		Chemical vapor deposition[96], decomposition of polymer[99]
N and B-doped carbon materials		Chemical vapor deposition[97]

catalyst from Pt nanoparticles composed of (100) planes.[63] Yamamoto et al. also prepared highly active

ORR catalyst than bulk Pt by using dendrimer as template to prepare 1 nm sized Pt clusters.[64]

Pt alloyed with transition metals such as Ni, Fe and Co shows high activities against ORR.[65-71]

Markovic et al. investigated the relationship between the *d*-band center position of Pt in Pt alloyed with 3*d*

transition metals. A relation between experimentally measured specific activity for the ORR on Pt based alloys in 0.1 M HClO$_4$ solution versus their d-band center position are shown in Figure 1-9. Pt-Co alloy which has decent adsorption/desorption energy against oxygen species shows highest ORR activity among Pt-3d transition metal alloys.[71] The difference of adsorption ability of Pt between Pt based alloys against oxygen species was also confirmed by EC-XPS[72] and theoretical approach.[73] Watanabe et al. reported that the surface coverage of OH on Pt-Fe alloy is lower than that on pure Pt during ORR.[72]

Pd based alloys such as Pd-Co and Pd-Ti show ORR activity comparable to Pt.[74, 75] The mechanism of ORR activity enhancement of Pd based alloys is similar to that of Pt based alloys. The d-band center position of Pd in Pd alloyed with transition metals is changed and OH adsorption on Pd during ORR is inhibited.

The electronic structure of Pt and Pd can be changed by their modification on foreign metals. Uosaki et al. reported that Au single crystal electrodes modified with submonolayer Pd show high activity against ORR.[76] The difference in geometric and electronic structures between Pd submonolayer on Au and bulk Pd were confirmed by surface X-ray scattering (SXS)[77] and second harmonic generation (SHG) measurements.[78] Adzic et al. prepared Pd and Pt monolayer on foreign metals and revealed the relation between d-band center position of ad-metals and their ORR activities.[79-81] They found that Pt monolayer on Pd(111) is a best ORR catalyst among the Pt monolayer on foreign metals. It is confirmed that OH desorption on Pt monolayer on Pd(111) starts more positive than that on Pt(111) by X-ray adsorption fine structure (XAFS) measurements.[79] These catalysts including core/shell structure catalysts achieve not only high ORR activity improvement but also reduction of Pt usage.

The mechanism of enhancement on ORR activity at Pt on metal oxides such as Pt-CeO$_x$ and Pt-NbO$_2$ is different from that of metallic alloy catalysts.[82, 83] In the case of the Pt-CeO$_x$, Pt oxide formation at positive potential region is inhibited by the oxidation reaction of Ce^{3+} to Ce^{4+}.[82] In the case of the Pt-NbO$_2$, the repulsion between OH on Pt and oxygen species of NbO$_2$ surface causes reduction of OH adsorption on Pt.[83]
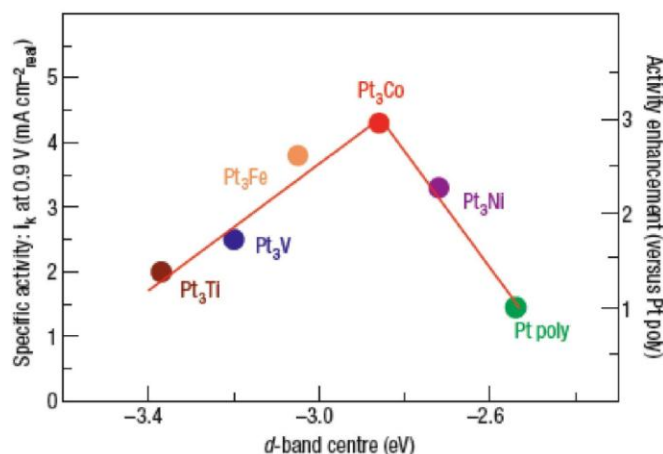
Figure 1-9. A relationship between experimentally measured specific activity for the ORR on Pt based alloys in 0.1 M $HClO_4$ solution versus their *d*-band center position.[71]

1.4.2.2   Non-noble metal catalysts

Some metal complexes such as metal porphyrin and phthalocyanine are known to show ORR activity.[84-89] Usually, the ORR at these metal complexes proceeds via $2e^-$ reduction process but ORR at co-facial Co porphyrin proceeds via $4e^-$ reduction process because μ-peroxo complex can be formed between O_2 and co-facial Co porphyrin[84]
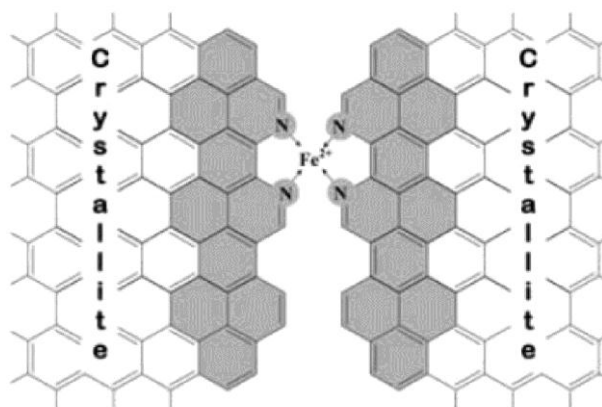
Figure 1-10. A proposed structure of nitrogen doped carbon materials containing Fe.[91]

Nitrogen doped carbon materials containing transition metals such as Fe and Co also show ORR activity and some of them show high ORR activity comparable to Pt.[90-93] These materials are often prepared by decomposition of mixture of metal salts and nitrogen containing organic materials. Some researchers suggested that porphyrin and phthalocyanine-like structures as shown in Figure 1-10 are main ORR active site in the materials.[91, 94]

1.4.2.3 Metal-free catalysts

Recently, ORR catalysts without noble metals such as nitrogen doped carbon materials have been paid much attention.[95-97] Nitrogen doped carbon materials for ORR catalyst are prepared by NH_3 treatment for carbon materials,[98] chemical vapor deposition[96] and decomposition of nitrogen containing polyaromatic molecules and polymers.[99-101] It is important to control nitrogen concentration and C–N bonding configurations.
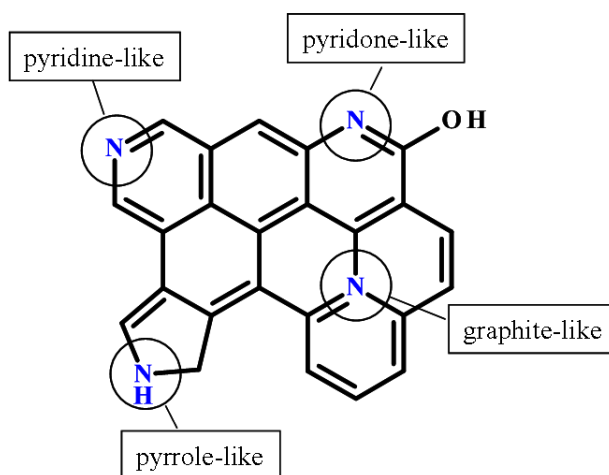
Figure 1-11. Schematic structure of C–N bonding configurations in nitrogen doped carbon materials.

But the nitrogen doped carbon materials prepared by these methods contain various C–N bonding configurations as shown in Figure 1-11.

Currently, studies on preparation of structural controlled non noble metal electrocatalysts are limited. Structure controlled carbon materials can be synthesized from organic molecules.[102-111] Osuka et al. synthesized highly fused porphyrin tapes. Their optical and electrochemical properties vary with the number of fused porphyrins (Figure 1-12).[106] Mullen et al. synthesized graphene sheet with 222 carbon atoms and graphene ribbon whose length is 12 nm (Figure 1-13).[109] Large graphene structures can be prepared not only in solution but also on solid surface. Fasel et al. reported synthesizing graphene structures from polyaromatic molecules with halogen group on single crystal metal surfaces in ultra high vacuum (UHV).[110, 111] Graphene structures can be obtained by heat induced coupling and dehydrogenation reactions of the molecules adsorbed on metal surface (Figure 1-14). The reactions proceed at relatively mild temperature (400ºC) at which organic molecules are not decomposed.
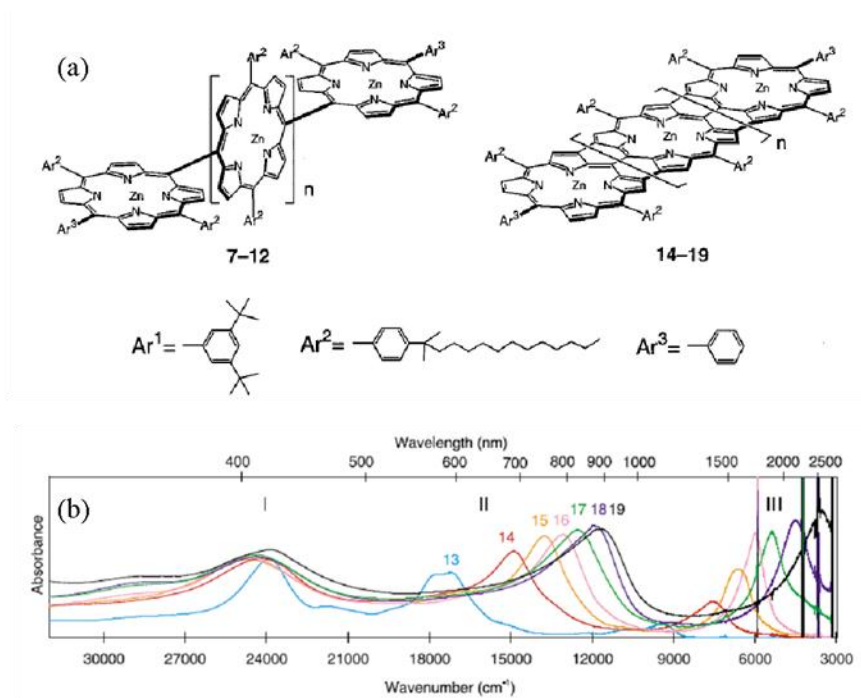
Figure 1-12. (a) Schematic structures of fused porphyrine tapes. (b) Their ultraviolet-visible-infrared spectra.[106]
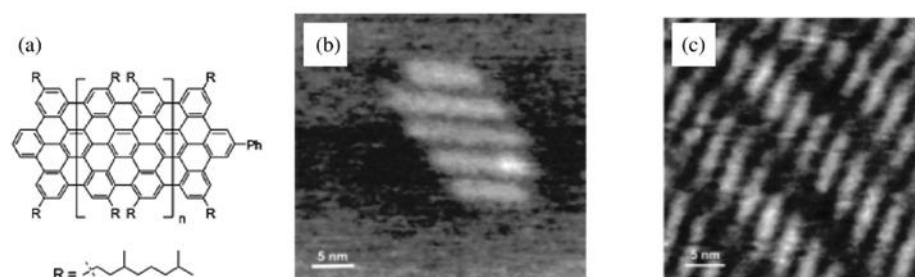
Figure 1-13. (a) A schematic structure of graphene ribbon. (b) and (c) STM images of graphene ribbons.[109]
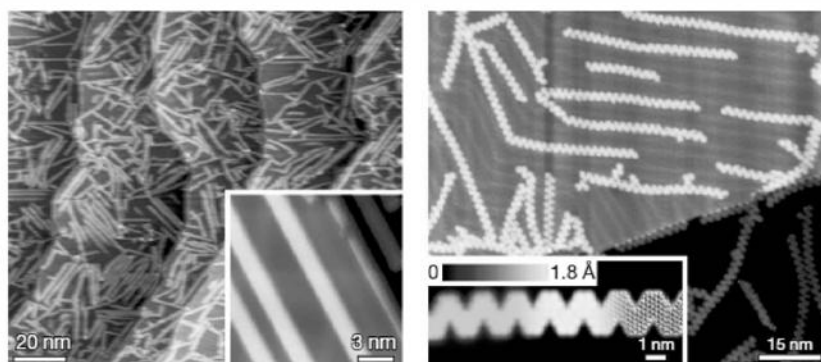
Figure 1-14. STM images of graphene ribbons prepared on Au(111) surface.[110]

1.5   Surface Characterization Techniques

The characterization of bulk and surface structure of electrocatalysts is important to understand the origin of electrocatalytic activity and develop novel electrocatalysts. The activity of catalysts described above strongly depends on their geometric and electronic structure. Some UHV techniques such as electron microscopy, low energy electron diffraction (LEED), auger electron spectroscopy (AES), X-ray photoelectron spectroscopy (XPS) give us geometric and electronic structure of electrocatalysts. But they can not be performed at the aqueous electrochemical condition because these measurements require electron as probe. The electrode reaction proceed on electrode surfaces through many complicated steps like adsorption, bond dissociation, electron transfer, desorption and diffusion and the electrode reaction activity depends on its crystal face.[60, 112, 113] The structure of electrode surface and electrode/electrolyte interface under the electrochemical condition can be observed by following methods (Table 1-3).

The electrode surface structure, including the structure of ad-metals and ad-molecules can be imaged by scanning tunneling microscopy (STM) and atomic force microscopy (AFM) in atomic level. Vibrational

Table 1-3. A summary for the surface characterization techniques.

Methods	Measuring objects
Scanning tunneling microscope (STM)	Surface local/electronic structure
Atomic force microscope (AFM)	Surface local structure, friction, magnetic property
Surface X-ray scattering (SXS)	Interface geometric structure
X-ray adsorption fine structure (XAFS)	Local structure, oxidation state, coordination number
Sum frequency generation (SFG)	Adsorbed molecular identification
Second harmonic generation (SHG)	Surface symmetry, electronic structure
Infrared reflection adsorption spectroscopy (IRRAS)	Adsorbed molecular identification
Surface enhanced Raman scattering (SERS)	Adsorbed molecular identification
Ellipthometry	Thickness of adsorbate
Quartz crystal microbalance (QCM)	Mass of adsorbate

13

spectroscopic methods such as infrared reflection absorption spectroscopy (IRRAS),[22, 36] sum frequency generation (SFG)[114-116] and surface enhanced Raman scattering (SERS)[117-119] are powerful technique to observe the adsorbed molecules on the electrode surface.

Hard X-ray measurements like surface X-ray scattering (SXS) and X-ray adsorption fine structure (XAFS) can provide not only surface but also bulk structure at electrochemical condition. SXS can investigate the three dimensional interfacial structures of single crystals.

XAFS is one of the most powerful techniques to probe the local structure of elements in materials. As an example, a typical Cu K edge XAFS spectrum of Cu foil is shown in Figure 1-15 (a). XAFS spectrum can be divided into two regions: the X-ray absorption near edge structure (XANES) and the extended X-ray absorption fine structure (EXAFS). The peak just above the edge is so-called white line (WL) and sensitive to the oxidation state because electrons of X-ray adsorbed atoms in materials are excited from core level to unoccupied state (Figure 1-15 (b)). At the higher energy region, the electrons are exited to unoccupied state and emitted as photoelectron. The emitted photoelectron is backscattered by the neighboring atoms and interfered with each other as shown in Figure 1-15 (c). The interference wave is called as EXAFS oscillation. XANES shows the local symmetry and electronic structure of the absorbing atom. EXAFS shows the identity, bond distance and coordination number of neighboring atoms of the absorbed atoms. To detect the surface structure of electrocatalysts, fluorescence XAFS is usable. The incident angle of X-ray is aligned to obtain total reflection of X-ray or fluorescence X-ray with high intensity from atoms and
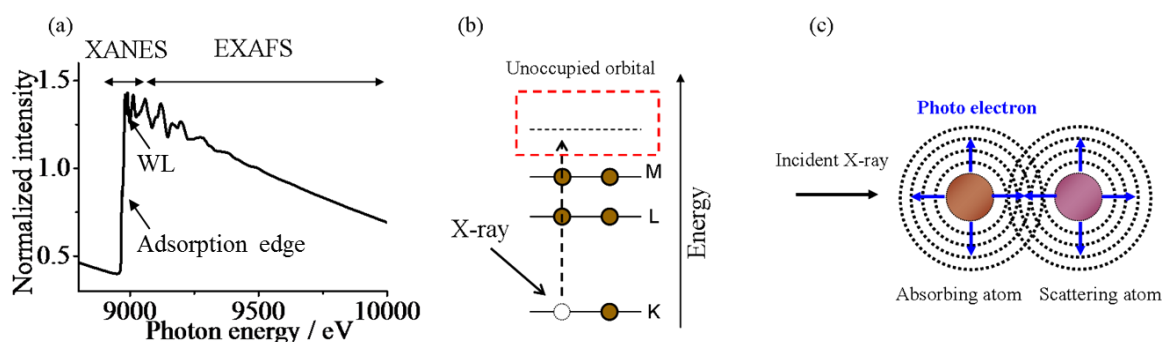
Figure 1-15. (a) Cu K edge XAFS spectrum of Cu foil. Schematic illustrations of (b) X-ray adsorption and (c) interference of photoelectron.

molecules in monolayer level.[82, 120-122]

1.6   Objective and Outline of the Present Thesis

In this thesis, electrocatalysts for fuel cell reactions were prepared from molecules by bottom-up methods and the relation between their structure and activity was investigated by various characterization techniques.

This thesis consists of 6 chapters.

In chapter 1, the background of the present study is described.

Chapter 2 describes the experimental details.

In chapter 3, Pt-Ru alloy was prepared from hetero binuclear Pt-Ru complex monolayer on Au(111) surface. The effect of Pt-Ru alloy coverage on MOR activity in acidic and alkaline solutions was investigated. The electrocatalytic activity of the Pt-Ru alloy with high coverage for MOR, CO oxidation reaction, HOR and ORR was compared with Pt-Ru alloy prepared from a mixture of K_2PtCl_4 and $RuCl_3$.

In chapter 4, structural difference between Pt-Ru alloys prepared from Pt-Ru complex and mixture of Pt and Ru salts was investigated by XPS and XAFS. The origin of enhancement of MOR activity and durability of Pt-Ru alloy prepared from Pt-Ru complex was revealed.

In chapter 5, nitrogen doped carbon materials were prepared by the pylorysis of penta-2-(*p*-ethynylphenyl)-ethynylpyridine (pepy) and the effect of heat treatment temperature on their structures and ORR activities was investigated. A brand new approach to prepare structure controlled graphene structures was also proposed and attempted.

Finally, chapter 6 summarizes the present thesis.

References

1. K. V. Kordesch and G. R. Simader, *Chem. Rev.*, 1995, **95**, 191-207.

2. L. Carrette, K. A. Friedrich and U. Stimming, *Fuel Cells*, 2001, **1**, 5-39.

3. U. B. Demirci, *J. Power Sources*, 2007, **169**, 239-246.

4. F. T. Wagner, B. Lakshmanan and M. F. Mathias, *J. Phys. Chem. Lett.*, 2010, **1**, 2204-2219.

5. N. W. Deluca and Y. A. Elabd, *J. Polym. Sci. Part B: Polym. Phys.*, 2006, **44**, 2201-2225.

6. M. W. Breiter, *Electrochim. Acta*, 1963, **8**, 973.

7. M. Arita, *Fuel Cells*, 2002, **2**, 10-14.

8. K. C. Neyerlin, W. B. Gu, J. Jorne and H. A. Gasteiger, *J. Electrochem. Soc.*, 2007, **154**, B631-B635.

9. B. Hammer and J. K. Norskov, *Nature*, 1995, **376**, 238-240.

10. S. Trasatti, *J. Electroanal. Chem.*, 1972, **39**, 163-&.

11. H. Igarashi, T. Fujino and M. Watanabe, *J. Electroanal. Chem.*, 1995, **391**, 119-123.

12. H. A. Gasteiger, N. M. Markovic and P. N. Ross, *J. Phys. Chem.*, 1995, **99**, 8290-8301.

13. H. A. Gasteiger, N. M. Markovic and P. N. Ross, *J. Phys. Chem.*, 1995, **99**, 16757-16767.

14. M. Watanabe, Y. M. Zhu and H. Uchida, *J. Phys. Chem. B*, 2000, **104**, 1762-1768.

15. H. Igarashi, T. Fujino, Y. M. Zhu, H. Uchida and M. Watanabe, *Phys. Chem. Chem. Phys.*, 2001, **3**, 306-314.

16. L. J. Wan, T. Moriyama, M. Ito, H. Uchida and M. Watanabe, *Chem. Comm.*, 2002, 58-59.

17. T. Takeguchi, T. Yamanaka, K. Asakura, E. N. Muhamad, K. Uosaki and W. Ueda, *J. Am. Chem. Soc.*, 2012, **134**, 14508-14512.

18. X. H. Xia, T. Iwasita, F. Ge and W. Vielstich, *Electrochim. Acta*, 1996, **41**, 711-718.

19. A. Hamnett, *Catal. Today*, 1997, **38**, 445-457.

20. T. H. M. Housmans and M. T. M. Koper, *J. Phys. Chem. B*, 2003, **107**, 8557-8567.

21. B. Hammer, Y. Morikawa and J. K. Norskov, *Phys. Rev. Lett.*, 1996, **76**, 2141-2144.

22. B. Beden, C. Lamy, A. Bewick and K. Kunimatsu, *J. Electroanal. Chem.*, 1981, **121**, 343-347.

23. E. Antolini, J. R. C. Salgado and E. R. Gonzalez, *Appl. Catal. B-Environ.*, 2006, **63**, 137-149.

24. K. W. Park, J. H. Choi, B. K. Kwon, S. A. Lee, Y. E. Sung, H. Y. Ha, S. A. Hong, H. Kim and A. Wieckowski, *J. Phys. Chem. B*, 2002, **106**, 1869-1877.

25. J. S. Spendelow, G. Q. Lu, P. J. A. Kenis and A. Wieckowski, *J. Electroanal. Chem.*, 2004, **568**, 215-224.

26. X. Zhang and K. Y. Chan, *J. Mater. Chem.*, 2002, **12**, 1203-1206.

27. Y. J. Ando, K. Sasaki and R. Adzic, *Electrochem. Commun.*, 2009, **11**, 1135-1138.

28. M. M. P. Janssen and J. Moolhuysen, *Electrochim. Acta*, 1976, **21**, 869-878.

29. A. Katayama, *J. Phys. Chem.*, 1980, **84**, 376-381.

30. G. Samjeske, H. S. Wang, T. Loffler and H. Baltruschat, *Electrochim. Acta*, 2002, **47**, 3681-3692.

31. S. Mylswamy, C. Y. Wang, R. S. Liu, J. F. Lee, M. J. Tang, J. J. Lee and B. J. Weng, *Chem. Phys. Lett.*, 2005, **412**, 444-448.

32. M. Wakisaka, S. Mitsui, Y. Hirose, K. Kawashima, H. Uchida and M. Watanabe, *J. Phys. Chem. B*, 2006, **110**, 23489-23496.

33. J. Munk, P. A. Christensen, A. Hamnett and E. Skou, *J. Electroanal. Chem.*, 1996, **401**, 215-222.

34. M. Watanabe and S. Motoo, *J. Electroanal. Chem.*, 1975, **60**, 267-273.

35. M. Watanabe and S. Motoo, *J. Electroanal. Chem.*, 1975, **60**, 275-283.

36. T. Yajima, H. Uchida and M. Watanabe, *J. Phys. Chem. B*, 2004, **108**, 2654-2659.

37. C. L. Green and A. Kucernak, *J. Phys. Chem. B*, 2002, **106**, 11446-11456.

38. J. X. Wang, N. S. Marinkovic, H. Zajonz, B. M. Ocko and R. R. Adzic, *J. Phys. Chem. B*, 2001, **105**, 2809-2814.

39. S. Hadzijordanov, H. Angersteinkozlowska, M. Vukovic and B. E. Conway, *J. Electrochem. Soc.*, 1978, **125**, 1471-1480.

40. T. Frelink, W. Visscher, A. P. Cox and J. A. R. Vanveen, *Electrochim. Acta*, 1995, **40**, 1537-1543.

41. E. Ticanelli, J. G. Beery, M. T. Paffett and S. Gottesfeld, *J. Electroanal. Chem.*, 1989, **258**, 61-77.

42. K. Kusada, M. Yamauchi, H. Kobayashi, H. Kitagawa and Y. Kubota, *J. Am. Chem. Soc.*, 2010, **132**, 15896-15898.

43. F. Maroun, F. Ozanam, O. M. Magnussen and R. J. Behm, *Science*, 2001, **293**, 1811-1814.

44. C. Roth, N. Martz, A. Morlang, R. Theissmann and H. Fuess, *Phys. Chem. Chem. Phys.*, 2004, **6**, 3557-3562.

45. R. Chetty, W. Xia, S. Kundu, M. Bron, T. Reinecke, W. Schuhmann and M. Muhler, *Langmuir*, 2009, **25**, 3853-3860.

46. A. Crown, C. Johnston and A. Wieckowski, *Surf. Sci.*, 2002, **506**, L268-L274.

47. L. S. Sarma, C. H. Chen, S. M. S. Kumar, G. R. Wang, S. C. Yen, D. G. Liu, H. S. Sheu, K. L. Yu, M. T. Tang, J. F. Lee, C. Bock, K. H. Chen and B. J. Hwang, *Langmuir*, 2007, **23**, 5802-5809.

48. H. Nitani, T. Nakagawa, H. Daimon, Y. Kurobe, T. Ono, Y. Honda, A. Koizumi, S. Seino and T. A. Yamamoto, *Appl. Catal. A: Gen.*, 2007, **326**, 194-201.

49. B. A. L. Demishima, H. T. Mishima and G. Castro, *Electrochim. Acta*, 1995, **40**, 2491-2500.

50. H. S. Wroblowa, Y. C. Pan and G. Razumney, *J. Electroanal. Chem.*, 1976, **69**, 195-201.

51. N. M. Markovic, T. J. Schmidt, V. Stamenkovic and P. N. Ross, *Fuel Cells*, 2001, **1**, 105-116.

52. N. M. Markovic, H. A. Gasteiger, B. N. Grgur and P. N. Ross, *J. Electroanal. Chem.*, 1999, **467**, 157-163.

53. V. Stamenkovic, N. M. Markovic and P. N. Ross, *J. Electroanal. Chem.*, 2001, **500**, 44-51.

54. N. M. Markovic, H. A. Gasteiger and P. N. Ross, *J. Phys. Chem.*, 1995, **99**, 3411-3415.

55. M. Harada, H. Noguchi, N. Zanetakis, S. Takakusagi, W. B. Song and K. Uosaki, *Sci. Technol. Adv. Mater.*, 2011, **12**.

56. R. R. Adzic, J. Wang and B. M. Ocko, *Electrochim. Acta*, 1995, **40**, 83-89.

57. F. H. B. Lima, J. Zhang, M. H. Shao, K. Sasaki, M. B. Vukmirovic, E. A. Ticianelli and R. R. Adzic, *J. Phys. Chem. C*, 2007, **111**, 404-410.

58. J. S. Guo, A. Hsu, D. Chu and R. R. Chen, *J. Phys. Chem. C*, 2010, **114**, 4324-4330.

59. A. P. Young, J. Stumper, S. Knights and E. Gyenge, *J. Electrochem. Soc.*, 2010, **157**, B425-B436.

60. N. M. Markovic, H. A. Gasteiger and N. Philip, *J. Phys. Chem.*, 1996, **100**, 6715-6721.

61. D. Strmcnik, K. Kodama, D. van der Vliet, J. Greeley, V. R. Stamenkovic and N. M. Markovic, *Nature Chem.*, 2009, **1**, 466-472.

62. J. Omura, H. Yano, M. Watanabe and H. Uchida, *Langmuir*, 2011, **27**, 6464-6470.

63. C. Wang, H. Daimon, T. Onodera, T. Koda and S. H. Sun, *Angew. Chem. Int. Ed.*, 2008, **47**, 3588-3591.

64. K. Yamamoto, T. Imaoka, W. J. Chun, O. Enoki, H. Katoh, M. Takenaga and A. Sonoi, *Nature Chem.*, 2009, **1**, 397-402.

65. T. Toda, H. Igarashi, H. Uchida and M. Watanabe, *J. Electrochem. Soc.*, 1999, **146**, 3750-3756.

66. V. Stamenkovic, T. J. Schmidt, P. N. Ross and N. M. Markovic, *J. Phys. Chem. B*, 2002, **106**, 11970-11979.

67. N. Wakabayashi, M. Takeichi, H. Uchida and M. Watanabe, *J. Phys. Chem. B*, 2005, **109**, 5836-5841.

68. V. Stamenkovic, B. S. Mun, K. J. J. Mayrhofer, P. N. Ross, N. M. Markovic, J. Rossmeisl, J. Greeley and J. K. Norskov, *Angew. Chem. Int. Ed.*, 2006, **45**, 2897-2901.

69. V. R. Stamenkovic, B. S. Mun, K. J. J. Mayrhofer, P. N. Ross and N. M. Markovic, *J. Am. Chem. Soc.*, 2006, **128**, 8813-8819.

70. V. R. Stamenkovic, B. Fowler, B. S. Mun, G. F. Wang, P. N. Ross, C. A. Lucas and N. M. Markovic, *Science*, 2007, **315**, 493-497.

71. V. R. Stamenkovic, B. S. Mun, M. Arenz, K. J. J. Mayrhofer, C. A. Lucas, G. F. Wang, P. N. Ross and N. M. Markovic, *Nature Mater.*, 2007, **6**, 241-247.

72. M. Wakisaka, H. Suzuki, S. Mitsui, H. Uchida and M. Watanabe, *J. Phys. Chem. C*, 2008, **112**, 2750-2755.

73. J. R. Kitchin, J. K. Norskov, M. A. Barteau and J. G. Chen, *J. Chem. Phys.*, 2004, **120**, 10240-10246.

74. K. Lee, O. Savadogo, A. Ishihara, S. Mitsushima, N. Kamiya and K. Ota, *J. Electrochem. Soc.*, 2006, **153**, A20-a24.

75. J. L. Fernandez, V. Raghuveer, A. Manthiram and A. J. Bard, *J. Am. Chem. Soc.*, 2005, **127**, 13100-13101.

76. H. Naohara, S. Ye and K. Uosaki, *Electrochim. Acta*, 2000, **45**, 3305-3309.

77. M. Takahasi, Y. Hayashi, J. Mizuki, K. Tamura, T. Kondo, H. Naohara and K. Uosaki, *Surf. Sci.*, 2000, **461**, 213-218.

78. T. Awatani, I. Yagi, H. Noguchi and K. Uosaki, *J. Electroanal. Chem.*, 2002, **524**, 184-193.

79. M. H. Shao, T. Huang, P. Liu, J. Zhang, K. Sasaki, M. B. Vukmirovic and R. R. Adzic, *Langmuir*, 2006, **22**, 10409-10415.

80. J. Zhang, Y. Mo, M. B. Vukmirovic, R. Klie, K. Sasaki and R. R. Adzic, *J. Phys. Chem. B*, 2004, **108**, 10955-10964.

81. J. L. Zhang, M. B. Vukmirovic, Y. Xu, M. Mavrikakis and R. R. Adzic, *Angew. Chem. Int. Ed.*, 2005, **44**, 2132-2135.

82. T. Masuda, H. Fukumitsu, K. Fugane, H. Togasaki, D. Matsumura, K. Tamura, Y. Nishihata, H. Yoshikawa, K. Kobayashi, T. Mori and K. Uosaki, *J. Phys. Chem. C*, 2012, **116**, 10098-10102.

83. K. Sasaki, L. Zhang and R. R. Adzic, *Phys. Chem. Chem. Phys.*, 2008, **10**, 159-167.

84. J. P. Collman, P. Denisevich, Y. Konai, M. Marrocco, C. Koval and F. C. Anson, *J. Am. Chem. Soc.*, 1980, **102**, 6027-6036.

85. K. Itaya, N. Shoji and I. Uchida, *J. Am. Chem. Soc.*, 1984, **106**, 3423-3429.

86. S. Yoshimoto, A. Tada and K. Itaya, *J. Phys. Chem. B*, 2004, **108**, 5171-5174.

87. M. S. Thorum, J. Yadav and A. A. Gewirth, *Angew. Chem. Int. Ed.*, 2009, **48**, 165-167.

88. A. Morozan, S. Campidelli, A. Filoramo, B. Jousselme and S. Palacin, *Carbon*, 2011, **49**,

4839-4847.

89.   N. Nishimura, M. Ooi, K. Shimazu, H. Fujii and K. Uosaki, *J. Electroanal. Chem.*, 1999, **473**, 75-84.

90.   R. Bashyam and P. Zelenay, *Nature*, 2006, **443**, 63-66.

91.   M. Lefevre, E. Proietti, F. Jaouen and J. P. Dodelet, *Science*, 2009, **324**, 71-74.

92.   G. Wu, K. L. More, C. M. Johnston and P. Zelenay, *Science*, 2011, **332**, 443-447.

93.   F. Jaouen, E. Proietti, M. Lefevre, R. Chenitz, J. P. Dodelet, G. Wu, H. T. Chung, C. M. Johnston and P. Zelenay, *Energy Environ. Sci.*, 2011, **4**, 114-130.

94.   J. M. Ziegelbauer, T. S. Olson, S. Pylypenko, F. Alamgir, C. Jaye, P. Atanassov and S. Mukerjee, *J. Phys. Chem. C*, 2008, **112**, 8839-8849.

95.   K. P. Gong, F. Du, Z. H. Xia, M. Durstock and L. M. Dai, *Science*, 2009, **323**, 760-764.

96.   L. T. Qu, Y. Liu, J. B. Baek and L. M. Dai, *ACS Nano*, 2010, **4**, 1321-1326.

97.   S. Y. Wang, L. P. Zhang, Z. H. Xia, A. Roy, D. W. Chang, J. B. Baek and L. M. Dai, *Angew. Chem. Int. Ed.*, 2012, **51**, 4209-4212.

98.   D. S. Geng, Y. Chen, Y. G. Chen, Y. L. Li, R. Y. Li, X. L. Sun, S. Y. Ye and S. Knights, *Energy Environ. Sci.*, 2011, **4**, 760-764.

99.   T. Iwazaki, R. Obinata, W. Sugimoto and Y. Takasu, *Electrochem. Commun.*, 2009, **11**, 376-378.

100.   J. I. Ozaki, S. I. Tanifuji, N. Kimura, A. Furuichi and A. Oya, *Carbon*, 2006, **44**, 1324-1326.

101.   A. Pacula, K. Ikeda, T. Masuda and K. Uosaki, *J. Power Sources*, 2012, **220**, 20-30.

102.   L. T. Scott, M. M. Boorum, B. J. McMahon, S. Hagen, J. Mack, J. Blank, H. Wegner and A. de Meijere, *Science*, 2002, **295**, 1500-1503.

103.   R. Jasti, J. Bhattacharjee, J. B. Neaton and C. R. Bertozzi, *J. Am. Chem. Soc.*, 2008, **130**, 17646-+.

104.   S. Hitosugi, T. Yamasaki and H. Isobe, *J. Am. Chem. Soc.*, 2012, **134**, 12442-12445.

105.   L. Grill, M. Dyer, L. Lafferentz, M. Persson, M. V. Peters and S. Hecht, *Nature Nanotechnol.*, 2007, **2**, 687-691.

106.   A. Tsuda and A. Osuka, *Science*, 2001, **293**, 79-82.

107.   M. Bieri, M. T. Nguyen, O. Groning, J. M. Cai, M. Treier, K. Ait-Mansour, P. Ruffieux, C. A. Pignedoli, D. Passerone, M. Kastler, K. Mullen and R. Fasel, *J. Am. Chem. Soc.*, 2010, **132**, 16669-16676.

108.   C. D. Simpson, J. D. Brand, A. J. Berresheim, L. Przybilla, H. J. Rader and K. Mullen, *Chem. Eur. J*, 2002, **8**, 1424-1429.

109.   X. Y. Yang, X. Dou, A. Rouhanipour, L. J. Zhi, H. J. Rader and K. Mullen, *J. Am. Chem. Soc.*, 2008, **130**, 4216-+.

110.   J. M. Cai, P. Ruffieux, R. Jaafar, M. Bieri, T. Braun, S. Blankenburg, M. Muoth, A. P. Seitsonen, M. Saleh, X. L. Feng, K. Mullen and R. Fasel, *Nature*, 2010, **466**, 470-473.

111.   M. Treier, C. A. Pignedoli, T. Laino, R. Rieger, K. Mullen, D. Passerone and R. Fasel, *Nature Chem.*, 2011, **3**, 61-67.

112.   H. Kita, Y. Z. Gao, T. Nakato and H. Hattori, *J. Electroanal. Chem.*, 1994, **373**, 177-183.

113.   N. M. Markovic, R. R. Adzic, B. D. Cahan and E. B. Yeager, *J. Electroanal. Chem.*, 1994, **377**, 249-259.

114.   H. Noguchi, T. Okada and K. Uosaki, *J. Phys. Chem. B*, 2006, **110**, 15055-15058.

115.   H. Noguchi, T. Okada and K. Uosaki, *Faraday Discuss.*, 2008, **140**, 125-137.

116.   M. Ito, H. Noguchi, K. Ikeda and K. Uosaki, *Phys. Chem. Chem. Phys.*, 2010, **12**, 3156-3163.

117.   H. Yang, Y. Yang and S. Zou, *J. Phys. Chem. C*, 2007, **111**, 19058-19065.

118.   K. Ikeda, J. Sato, N. Fujimoto, N. Hayazawa, S. Kawata and K. Uosaki, *J. Phys. Chem. C*, 2009, **113**, 11816-11821.

119.   K. Ikeda, S. Suzuki and K. Uosaki, *Nano Lett.*, 2011, **11**, 1716-1722.

120.   K. Tamura, H. Oyanagi, T. Kondo, M. Koinuma and K. Uosaki, *J. Phys. Chem. B*, 2000, **104**, 9017-9024.

121.   J. R. I. Lee, R. L. O'Malley, T. J. O'Connell, A. Vollmer and T. Rayment, *J. Phys. Chem. C*, 2009,

113, 12260-12271.

122.   T. Masuda, H. Fukumitsu, S. Takakusagi, W. J. Chun, T. Kondo, K. Asakura and K. Uosaki, *Adv. Mater.*, 2012, **24**, 268-272.

Chapter 2

EXPERIMENTAL

2.1   Materials

H$_2$SO$_4$ (suprapure grade), 30% H$_2$O$_2$ aqueous solution (suprapure grade), KOH (reagent grade), NaOH (reagent grade), 60% HClO$_4$ aqueous solution (reagent grade), Na$_2$SO$_4$ (reagent grade), K$_3$[Fe(CN)$_6$] (reagent grade), methanol (reagent grade), acetone (reagent grade), ethanol (reagent grade), acetonitrile (reagent grade), dichloromethane (reagent grade), carbon tetrachloride (reagent grade), hexane (reagent grade), toluene (reagent grade), diethylether (reagent grade), acetic acid (reagent grade), 1, 5-cyclooctadiene (reagent grade), 2,2'-bipyridine (reagent grade), 2,2':6',2"-terpyridine   (reagent grade), K$_2$PtCl$_4$ (reagent grade), RuCl$_3$ (reagent grade), CuSO$_4$ (reagent grade), AgNO$_3$ (reagent grade), LiCl (reagent grade), NaPF$_6$ (reagent grade), 9, 10-dibromoanthracene (DBA) (reagent grade), N-bromosuccinimide (NBS) (reagent grade) and bromine (reagent grade) were purchased from Wako Pure Chemical Industries, Ltd. Anthron (reagent grade), Sn powder (reagent grade) and 5,15-diphenylporphine (reagent grade) were purchased from Tokyo Chemical Industry Co., Ltd. 2-octylthio-1,3,5-triazine-4,6-dithiol (H$_2$otd) was provided from Sankyo Kasei Co., Ltd. All chemicals were used without further purification. A colloidal solution of Au nanoparticles was purchased from Funakoshi. Water was purified using a Milli-Q purification system (Yamato, WQ-500). Ultrapure-Ar (99.999%), pure O$_2$ (99.95%), pure H$_2$, pure CO and 0.2% CO/H$_2$ mixture were purchased from Taiyo Nippon Sanso Co. Ltd. Au wire (99.999% pure, ϕ = 0.8 mm) and Pt wire (99.999% pure, ϕ = 0.8 mm) were purchased from Tanaka Precious Metals. The Ag and Pt wires used as the reference electrodes and the counter electrodes were purchased from Nilaco.

2.2   Synthesis

2.2.1   [Ru^{II}(bpy)(tpy)(H$_2$O)](PF$_6$)$_2$ and [Pt^{II}(tpy)(OH)]PF$_6$

Literatures were used to prepare these materials[1-5].

2.2.2   [Ru^{II}(bpy)(tpy)(Hotd)](PF$_6$)$_2$[6]

15 ml of ethanol solution of H$_2$otd (65.1 mg, 0.25 mmol) was added drop-wise to 160 ml of ethanol solution containing [Ru^{II}(bpy)(tpy)(H$_2$O)](PF$_6$)$_2$ (180 mg, 0.23 mmol) and triethylamine (31.5 μl, 0.23 mmol) with vigorous stirring at room temperature. The mixture was concentrated by rotary evaporator to obtain red precipitate. Concentrated reaction mixture with precipitate was kept in a freezer for 2 h and then filtered. The residue was dissolved in small amount of acetonitrile and the solution was passed through a Sephadex-LH20 column (ϕ = 3 cm, L = 20 cm, eluting with acetonitrile). The first red band was collected and the eluate was concentrated (ca. 5 mL) by rotary evaporator. The red product was recrystallized from 30 ml of diethylether and stored in a refrigerator overnight. The microcrystalline solid thus obtained was filtered and dried *in vacuo*. Yield, 86.1 mg (37.2%).

2.2.3   [Pt^{II}(tpy)Ru^{II}(bpy)(tpy)(μ-otd)](PF$_6$)$_2$ (Pt-Ru complex)[6]

An acetone suspension of [Pt^{II}(tpy)(OH)]PF$_6$ (14.75 mg, 0.025 mmol) was added drop-wise to 5 ml of acetone solution of [Ru^{II}(bpy)(tpy)(Hotd)](PF$_6$)$_2$ (23.1 mg, 0.025 mmol) with vigorous stirring at room temperature. The mixture was stirred for 40 min and the filtered to remove precipitate. The filtrate solution was collected and the vapor of diethylether was diffused for 4 d. Red microcrystalline compounds were then purified by a Sephadex-LH20 column chromatography eluted with acetonitrile. The first red band was concentrated by rotary evaporator and recrystallized from diethylether. Needle reddish crystals were collected by filtration and dried *in vacuo*. Yield, 15.5 mg (40%). Anal. Calcd for C$_{51}$H$_{47}$F$_{12}$N$_{11}$P$_2$PtRuS$_3$ · H$_2$O: C, 40.45; H, 3.26; N, 10.17; S, 6.35%. Found: C, 40.54; H, 3.33; N, 10.13; S, 6.42%.

2.2.4   [(Pt^{II}(tpy))$_2$(μ-otd)](PF$_6$)$_2$ (Pt-Pt complex)

Synthesis of Pt-Pt complex was performed by Dr. Zhang at Hokkaido University. An acetone

suspension of [Pt^{II}(tpy)(OH)]PF$_6$ (118.0 mg, 0.20 mmol) was added drop-wise to 20 ml of acetone solution

of H$_2$otd (58.0 mg, 0.010 mmol) with vigorous stirring at room temperature. The mixture was stirred for 40

min and the filtered to remove precipitate. The filtrate solution was collected and concentrated by rotary

evaporator. Obtained yellow crystals were washed with small amount of acetone, and dried under *vacuo*.

Yield, 15.5 mg (40%). ^{1}H NMR (*d*-DMSO): δ 8.88 (d, 4H), 8.55 (t, 2H), 8.41 (d, 4H), 8.28 (d, 4H), 8.10 (t,

4H), 7.69 (t, 4H), 3.09 (t, 2H), 1.70 (t, 2H), 1.30 (m, 10H), 0.87 (t, 3H). Anal. Calcd for

C41H39F12N9P2PtRuS3・CH$_3$COCH$_3$: C, 35.42; H, 3.04; N, 8.45; S, 6.45%. Found: C, 35.52; H, 3.02; N,

8.92; S, 5.93%. ^{1}H NMR spectrum of Pt-Pt complex in *d*-DMSO is represented in Figure 2-1.
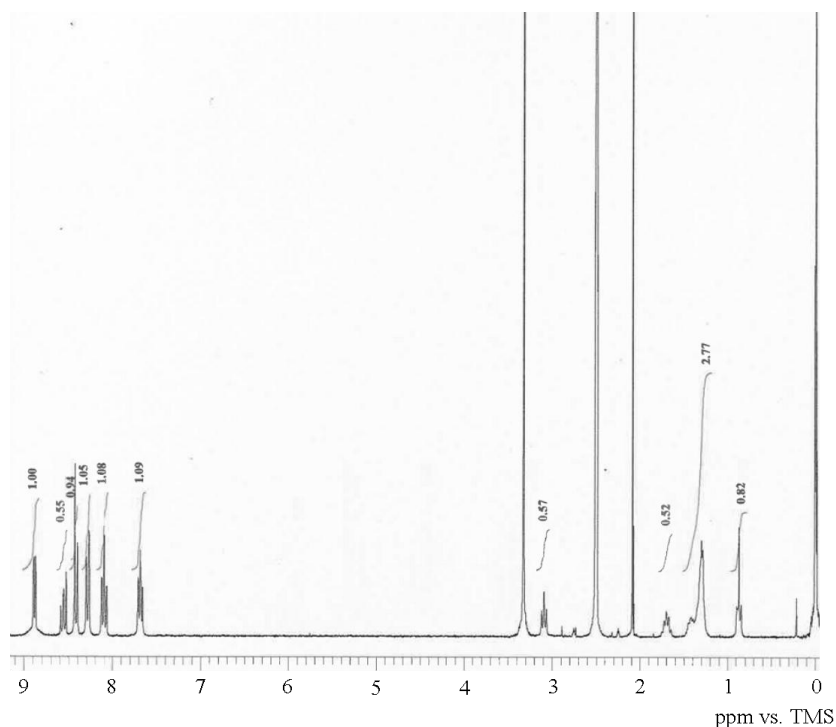
Figure 2-1. ^{1}H NMR spectrum of Pt-Pt complex in *d*-DMSO.

2.2.5   Penta-2-(*p*-ethynylphenyl)-ethynylpyridine (pepy)[7-10]

Synthesis of pepy was performed by Dr. Zhang at Hokkaido University as shown in Scheme 2-1.

^{1}H NMR (*d*-chloroform): δ 7.48–7.68 (m, 20H), 3.22 (m, 5H). ^{1}H NMR spectrum of 9,9'-bianthryl in

CDCl$_3$ is represented in Figure 2-2.

2.2.6   9,9'-bianthryl[11]

Anthron (2 g) was dissolved in a mixture of acetic acid (20 ml) and concentrated hydrochloric acid (8 ml) and to the boiling solution granulated Sn (8 g) was cautiously added. The refluxing was continued fot 1.5 hours. Yield, 1.8 g. ^{1}H NMR (d-chloroform): δ 8.68 (s, 2H), 8.13 (d, 4H), 7.43 (t, 4H), 7.11 (m, 8H). ^{1}H NMR spectrum of 9,9'-bianthryl in CDCl₃ is represented in Figure 2-3.

Figure 2-2. ^{1}H NMR spectrum of pepy in CDCl₃.

Figure 2-3. ^{1}H NMR spectrum of 9,9'-bianthryl in CDCl₃.

27

Scheme 2-1. Synthesis of pepy.

28

2.2.7 10,10'-dibromo, 9,9'-bianthryl (DBBA)[12]

A solution of bromine (0.15 g, 0.93 mmol) in carbon tetrachloride (7.5 ml) was added drop-wise for 10 min to a solution of 9,9'-bianthryl (0.15 g, 0.42 mmol) in carbon tetrachloride (8 ml) at 0 ℃ (ice bath). The ice bath was removed and the mixture was stirred for 1 d at room temperature. 0.1 M sodium thiosulfate solution (5 ml) was added to the mixture and the organic layer was colledted and the solvent was removed. The product was finally purified by chromatography on silica gel with hexane : dichloromethane (20:1), yeiling 10,10'-dibromo, 9,9'-bianthracenyl as a light yellow solid (0.05 g, 23.0 %). ^{1}H NMR (d-chloroform): δ 8.71 (d, 4H), 7.57 (t, 4H), 7.16 (t, 4H), 7.07 (d, 4H). ^{1}H NMR spectrum of DBBA in CDCl$_3$ is represented in Figure 2-4.
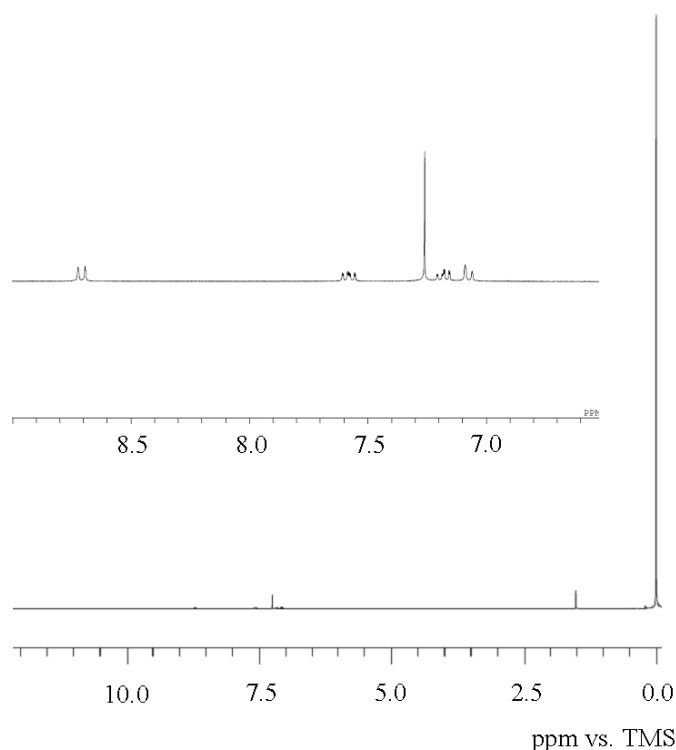
Figure 2-4. ^{1}H NMR spectrum of DBBA in CDCl$_3$.

2.2.8 5,15-dibromo, 10,20-diphenylporphine (DBP)[13]

To a solution of 5,15-diphenylporphine (50 .9 mg, 0.11 mmol) in dichloromethane (100 ml), NBS (39.7 mg, 0.22 mmol) was added and the mixture was stirred for 1 h. The solution was concentrated by rotary evaporator and purified by chromatography on silica gel with hexane : toluene (3:1), yielding 5,15-dibromo,

29

10, 20-diphenylporphyine as a purple solid (20.5 mg, 30.0 %). ^{1}H NMR (d-chloroform): δ 9.68 (d, 4H), 8.88 (d 4H), 8.17 (d, 4H), 7.80 (m, 6H). ^{1}H NMR spectrum of DBP in CDCl$_3$ is represented in Figure 2-5.
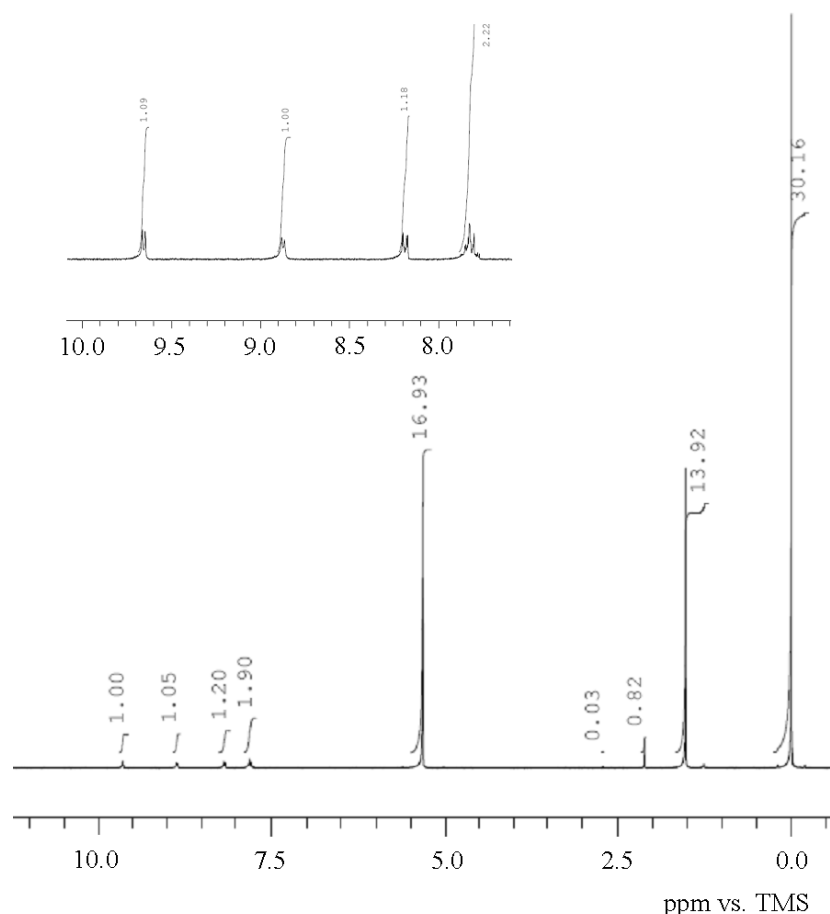
Figure 2-5. ^{1}H NMR spectrum of DBP in CDCl$_3$.

2.3   Sample Preparation

2.3.1   Preparation of Au substrate and poly Pt electrode

An Au(111) single crystal electrode for electrochemical measurements was prepared from Au wire by Clavilier's method.[14] The Au(111) single crystal was annealed in hydrogen flame and quenched with Milli-Q water before a molecular modification. Figure 2-6 shows typical cyclic voltammograms (CVs) of Au(111) in 50 mM H$_2$SO$_4$ solution. Current peaks corresponding to surface reconstruction (0.35 V), sulfate ion adsorption/desorption (0.85 V) Au oxide formation (1.4 V) and Au oxide reduction (0.9 V) were observed The Au(111) surface area can be estimated from the charge of Au oxide reduction reaction (444 μC/cm^2).[15]

Au substrates for X-ray photoelectron spectroscopy (XPS) and X-ray adsorption fine structure (XAFS) measurements (gold thickness: 200 nm) were prepared with a (111) orientation on mica by sputtering at the Nanotechnology Innovation Station of the National Institute of Materials Science (NIMS).
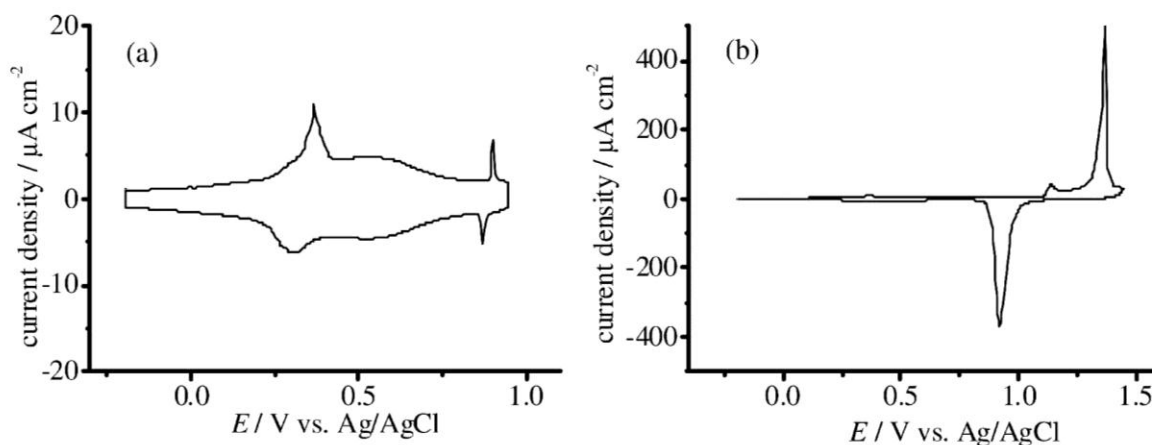
Figure 2-6. CVs of Au(111) prepared by Clavilier's method in 50 mM H_2SO_4 solution. Scan rate = 50 mV s^{-1}.

Poly Pt was prepared from Pt wire. Pt bead without facets prepared by melting Pt wire was polished. Figure 2-7 shows a typical CV of poly Pt in 50 mM H_2SO_4 solution. Current waves corresponding to hydrogen adsorption/desorption (–0.1 V) and OH adsorption/desorption (0.6 V) were observed.
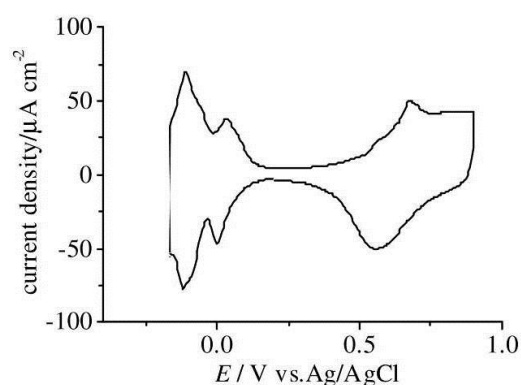
Figure 2-7. A CV of poly Pt in 50 mM H_2SO_4 solution. Scan rate = 50 mV s^{-1}.

2.3.2   Formation of monolayer of Pt-Ru complex and its decomposition

Clean Au(111) was washed with acetone and immersed into 100 μM Pt-Ru complex acetone solution for 30 min. After Au(111) modified with Pt-Ru complex was rinsed with acetone, it was put in an electric furnace and heat treated at 300 ℃ for 1 hour under O_2 flow.

31

2.3.3 Preparation of Pt-Ru alloy catalyst with high coverage on Au(111) from Pt-Ru complex

The cycle of the immersion into 100 μM Pt-Ru complex acetone solution for 30 min and heat treatment at 300 ℃ under O_2 flow was repeated to obtain Pt-Ru alloys with high coverage. The Pt-Ru alloys prepared by repeating the cycle of Pt-Ru complex adsorption and heat treatment are called n-Pt-Ru/Au (n is the number of the Pt-Ru complex adsorption and heat treatment cycle.).

2.3.4 Preparation of Pt-Ru alloy catalyst on Au(111) from a mixture of K_2PtCl_4 and $RuCl_3$

500 μM of K_2PtCl_4 and $RuCl_3$ aqueous solution was sprayed on Au(111) and the thus-modified Au(111) was heat treated at 300 ℃ for 1 hour under O_2 or H_2 flow in the electric furnace. After the heat treatment, the modified Au(111) was rinsed with Milli-Q water to remove remaining KCl. The cycle of modification and decomposition of K_2PtCl_4 and $RuCl_3$ were repeated five times. The Pt-Ru alloys prepared by heating Au(111) modified with K_2PtCl_4 and $RuCl_3$ in O_2 and H_2 are called Pt-Ru$_{mix}$/Au and Pt-Ru$_{mix}$/Au (H_2), respectively.

2.3.5 Preparation of Au(111) modified with Pt from Pt-Pt complex

Clean Au(111) was washed with acetone and immersed into 100 μM Pt-Pt complex acetone solution for 30 min. The Pt-Pt complex modified Au(111) was rinsed with acetone and it was heat treated at 300 ℃ for 1 hour under O_2 flow in the electric furnace. The surface coverage of Pt was increased by repeating the cycle of Pt-Pt complex adsorption and heat treatment. The Pt modified Au(111) are called n-Pt/Au (n is the number of the Pt-Pt complex adsorption and heat treatment cycle.).

2.3.6 Modification of pepy on HOPG and its pyrolysis

5 μl of 100 μM pepy dichloromethane was casted on HOPG for 4 times. The HOPG modified with pepy was heat treated at 500, 600, 700 and 800 ℃ for 30 min under Ar atmosphere and the pepy heat

treated at 500, 600, 700 and 800 ℃ is called 500py, 600py, 700py and 800py, respectively.

2.3.7   Preparation of Au(111) modified with DBA, DBBA and DBP and their heat treatment

Clean Au(111) was immersed in 100 μM DBA dichloromethane, 100 μM DBBA dichloromethane or

0.1 μM DBP dichloromethane solution for 30 min and washed with dichloromethane. A DBA layer with

low coverage was prepared by an immersion of Au(111) in 0.1 μM DBA dichloromethane for 10 s. A

DBBA layer with low coverage was by an immersion of Au(111) in 0.1 μM DBBA dichloromethane for 10

s. The Au(111) modified with the molecules was heat treated at 250 ℃ or 460 ℃ for 30 min under Ar

atmosphere. The temperature was raised from room temperature to the heat treatment temperature at 10

K/min. Before the sample preparation, the cleanness of furnace was confirmed. Figure 2-8 shows a STM

image of bare Au(111) after the heat treatment at 460℃ for 30 min under Ar atmosphere in the furnace. The

surface reconstruction structure of Au(111), √3x22 structure was observed and this result indicates that

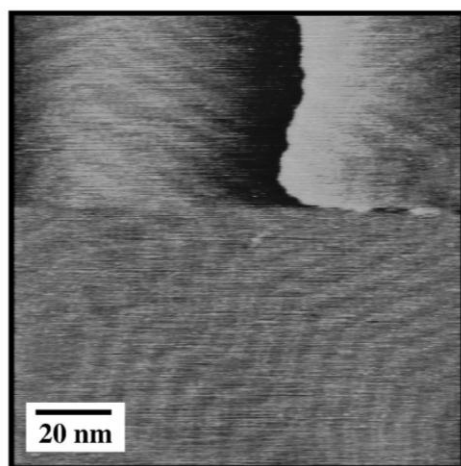furnace was kept clean during the heat treatment.

Figure 2-8. An STM image of heat treated Au(111) at 460℃ under Ar flow in an electronic furnace
for 30 min.

2.4   Characterization Methods

2.4.1   Scanning tunneling microscopy (STM)

STM measurements were carried out with a Pico-SPM (Molecular Imaging) controlled by Nanoscope E

(Digital Instruments) in air at room temperature. A Au(111) facet prepared by Clavilier's method was used for STM measurements. The electrochemical cell with the four-electrode configuration which can accommodate a single crystal bead electrode was used for STM measurements under electrochemical condition.[16] A Pt coil and AuO_x were used as a counter and a reference electrode, respectively. STM tips were mechanically cut Pt/Ir wire (80/20, $\phi = 0.25$ mm) and insulated with Apiezon wax (Nilaco).

2.4.2   X-ray photoelectron spectroscopy (XPS)

XPS measurements were performed with Al K_α X-ray source on a JPS-9200 spectrometer (JEOL) or a theta probe (thermo electrons) those belong to Research Institute for Electronic Science at Hokkaido University and MANA foundry at NIMS, respectively. All binding energy was calibrated with an $Au4f_{7/2}$ peak at 84.0 eV.[17]

Angle resolved XPS measurements for valence band region were performed with Mg K_α X-ray source on a JPS-9010 spectrometer (JEOL) at the Catalysis Research Center, Hokkaido University.

2.4.3   Raman spectroscopy

Raman spectroscopic measurements were conducted by He-Ne laser excitation (632.8 nm). For gap mode Raman spectroscopic measurements,[18-20] metal surfaces modified with molecules were dipped in a commercially available colloidal solution of Au nanoparticles with a diameter of ca. 50 nm for more than 2 h and washed with Milli-Q water.

2.4.4   Electrochemistry

Electrochemical measurements were carried out with a HSV-100 (Hokuto Denko) at room temperature, using a home-made three-electrode electrochemical cell under Ar or O_2 atmosphere. The mechanically polished Au(111) and poly Pt were used as working electrode with hanging meniscus configuration. A Pt coil and an Ag/AgCl wire in saturated NaCl solution were used as a counter and a reference electrode,

respectively. All the potentials in this paper are presented with respect to Ag/AgCl. CO stripping measurement was performed with same system. Pure CO was bubbled in electrolyte for 30 s, 60 s, 120 s, 300 s and 600 s. Excess CO was purged with Ar for more than 30 min. The working electrode was kept at 0.2 V vs. Ag/AgCl in 0.1 M HClO$_4$ solution during CO and Ar bubbling.

Rotating disk electrode (RDE) measurements were carried out using a dynamic electrode unit (Hokuto Denko, HR-201 and HR-202) at room temperature. The mechanically polished Au(111) and poly Pt were used as working electrode with hanging meniscus configuration.[21, 22] A Pt coil and an Ag/AgCl wire in saturated NaCl solution were used as a counter and reference electrode, respectively. Liner sweep voltammograms (LSVs) were recorded at a scan rate of 10 mV/s with rotating rate from 500 to 3500 rpm. Before RDE measurements in 0.1 M HClO$_4$ solution saturated with H$_2$ containing 0.2% CO, the working electrode was scanned from −0.27 to 1.20 V vs. Ag/AgCl and held at −0.26 V for 5 min with rotating rate of 2500 rpm.[23] An accuracy of hanging meniscus RDE (HMRDE) system was confirmed by HMRED measurements in 50 mM Na$_2$SO$_4$ solution containing 1 mM K$_3$[Fe(CN)$_6$]. Figure 2-9 (a) shows LSVs of Au(111) in 50 mM Na$_2$SO$_4$ solution containing 1 mM K$_3$[Fe(CN)$_6$]. Cathodic current starts to flow at around 0.4 V vs. Ag/AgCl corresponds to following reaction.

$$[\text{Fe(CN)}_6]^{3-} + \text{e}^- \rightarrow [\text{Fe(CN)}_6]^{4-} \qquad (2\text{-}1)$$
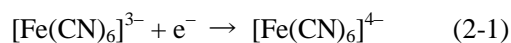
The RDE data in limiting current regime are analyzed using the Levich equation to determine diffusion coefficient of [Fe(CN)$_6$]$^{3-}$.

$$i = 0.62nFAD^{2/3}Cv^{-1/6}\omega^{1/2} = B\omega^{1/2} \qquad (2\text{-}2)$$

where i is the measured limiting current, n is the reaction electron number, F is the Faraday's coefficient (96500 C mol^{-1}), A is the geometric electrode area (0.04 cm^2), D is the diffusion coefficient, C is the

35

concentration of reactant, $[Fe(CN)_6]^{3-}$ in electrolyte, v is the kinematic viscosity of the electrolyte solution

$(0.01 \; cm^2 \; s^{-1})$ and ω is the rotation rate $(rad \; s^{-1})$. From the Levich plot (i/A versus $\omega^{1/2}$) shown in Figure 2-9

(b) for the limiting current at –0.4 V, diffusion coefficient of $[Fe(CN)_6]^{3-}$ was estimated as 8.9 × $10^{-6} \; cm^2$

s^{-1}.
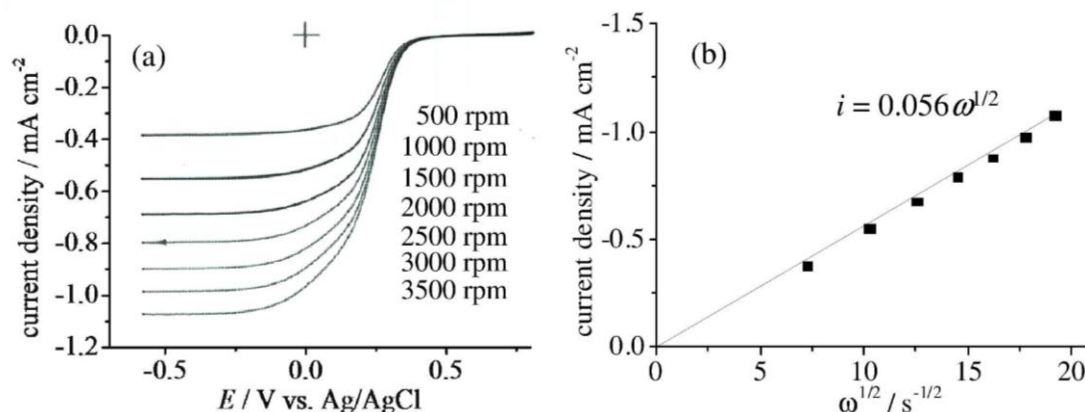
Figure 2-9. (a) LSVs of Au(111) in 50 mM Na_2SO_4 solutions containing 1 mM $K_3[Fe(CN)_6]$. Scan rate = 10 mV s^{-1}. (b) The Levich plot for the LSVs in Figure 2-3 (a).

2.4.5   X-ray adsorption fine structure (XAFS) measurements

The ex-situ fluorescence-mode Ru K edge XAFS measurements of Au(111) modified with Pt-Ru alloys were performed at BL14B1 of SPring8 with an s-polarized X-ray. The storage ring was operated at 8 GeV and 99.5 mA. The X-ray was monochromatized using a Si(111) double crystal monochromator. All measurements, including those for standard samples, were performed in fluorescence mode at room temperature in air. Figure 2-5 shows schematic illustration of optical setup. For XAFS measurements for Pt-Ru alloy modified Au(111), the incident angle of X-ray was aligned (88º) to increase the X-ray irradiation area and intensity of the fluorescence X-ray. The fluorescence signal was collected by a 19-element pure Ge solid-state detector (SSD) (GL0110S; Canberra, USA). The background subtraction with Victoreen's function and curve fitting of EXAFS oscillation based on the plane-wave and single scattering theory was carried out using a REX 2000.

Figure 2-10. A schematic illustration of the optical setup at BL14 of SPring-8.

References

1.   K. J. Takeuchi, M. S. Thompson, D. W. Pipes and T. J. Meyer, *Inorg. Chem.*, 1984, **23**, 1845-1851.

2.   T. K. Aldridge, E. M. Stacy and D. R. Mcmillin, *Inorg. Chem.*, 1994, **33**, 722-727.
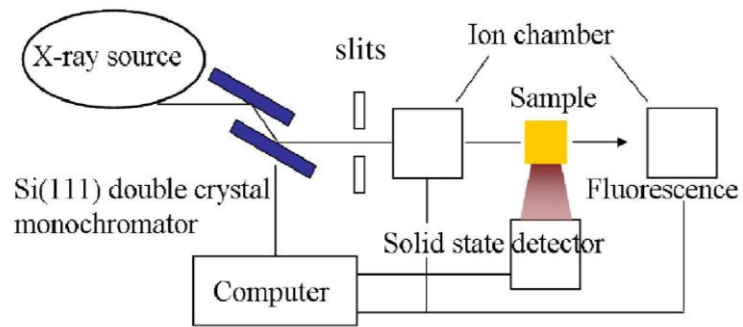
3.   J. X. Mcdermott, J. F. White and G. M. Whitesides, *J. Am. Chem. Soc.*, 1976, **98**, 6521-6528.

4.   G. Annibale, M. Brandolisio and B. Pitteri, *Polyhedron*, 1995, **14**, 451-453.

5.   H. Tannai, Ph.D thesis, Hokkaido University, 2005.

6.   H. Uehara, Ph.D thesis, Hokkaido University, 2009.

7.   O. Lavastre, L. Ollivier, P. H. Dixneuf and S. Sibandhit, *Tetrahedron*, 1996, **52**, 5495-5504.

8.   M. Schmittel and H. Ammon, *Synlett*, 1999, 750-752.

9.   P. Ehlers, A. Neubauer, S. Lochbrunner, A. Villinger and P. Langer, *Org. Lett.*, 2011, **13**, 1618-1621.

10.   F. Morgenroth and K. Mullen, *Tetrahedron*, 1997, **53**, 15349-15366.

11.   F. Bell and D. H. Waring, *J. Chem. Soc.*, 1949, 267-269.

12.   J. M. Cai, P. Ruffieux, R. Jaafar, M. Bieri, T. Braun, S. Blankenburg, M. Muoth, A. P. Seitsonen, M. Saleh, X. L. Feng, K. Mullen and R. Fasel, *Nature*, 2010, **466**, 470-473.

13.   S. Shanmugathasan, C. K. Johnson, C. Edwards, E. K. Matthews, D. Dolphin and R. W. Boyle, *J. Porphyrins Phthalocyanines*, 2000, **4**, 228-232.

14.   J. Clavilier, R. Faure, G. Guinet and R. Durand, *J. Electroanal. Chem.*, 1980, **107**, 205-209.

15.   S. Strbac, R. R. Adzic and A. Hamelin, *J. Electroanal. Chem.*, 1988, **249**, 291-310.

16.   K. Uosaki, S. Ye, H. Naohara, Y. Oda, T. Haba and T. Kondo, *J. Phys. Chem. B*, 1997, **101**, 7566-7572.

17.   J. F. Moulder, W. F. Stickle, P. E. Sobol and K. D. Bomben, *Handbook of X-ray Photoelectron Spectroscopy*, Perkin-Elmer, Minnesota, 1992.

18.   K. Ikeda, N. Fujimoto, H. Uehara and K. Uosaki, *Chem. Phys. Lett.*, 2008, **460**, 205-208.

19.   K. Ikeda, J. Sato, N. Fujimoto, N. Hayazawa, S. Kawata and K. Uosaki, *J. Phys. Chem. C*, 2009,

113, 11816-11821.

20.   K. Ikeda, S. Suzuki and K. Uosaki, *Nano Lett.*, 2011, **11**, 1716-1722.

21.   H. M. Villullas and M. L. Teijelo, *J. Electroanal. Chem.*, 1995, **384**, 25-30.

22.   H. M. Villullas and M. L. Teijelo, *J. Electroanal. Chem.*, 1995, **385**, 39-44.

23.   H. A. Gasteiger, N. M. Markovic and P. N. Ross, *J. Phys. Chem.*, 1995, **99**, 8290-8301.
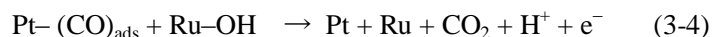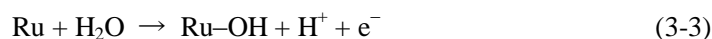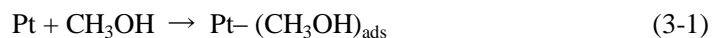
Chapter 3

ELECTROCATALYTIC ACTIVITY OF PT-RU ALLOY PREPARED FROM

HETERO BI-NUCLEAR PT-RU COMPLEX ON AU(111)

3.1 Introduction

Pt-Ru alloys are promising electrocatalysts for hydrogen oxidation reaction (HOR)[1-4] and methanol oxidation reaction (MOR).[5-7] Hydrogen gas produced from organic molecules often contains low amounts of CO. CO strongly interacts with Pt and prohibits HOR and MOR on Pt. The adsorption of CO on a Pt surface is prevented by the modification of the electronic structure of Pt. The Pt–CO interaction is weakened when Pt is alloyed with Ru.[8-10] Therefore, Pt-Ru alloys can have high HOR activity even in the presence of small amounts of CO.

Although the standard electrode potential for MOR is 0.04 V (vs. SHE),[11] MOR only proceeds at a potential significantly more positive than the standard electrode potential, because CO covers the Pt surface. CO covers the Pt surface as a result of the dissociative adsorption of methanol and then CO prevents the oxidation of methanol until the adsorbed CO is removed by reacting with surface OH, which is formed at positive potentials. The removal of CO by OH from a Pt surface can be enhanced by Ru modification. This modification allows OH adsorption to start at a more negative potential.[12, 13] The enhancement of MOR activity can be explained by a bi-functional mechanism proposed by Watanabe and Motoo.[14, 15] According to this bi-functional mechanism, Pt acts as an MOR active site, and Ru supplies oxidants such as Ru–OH to assist in the oxidative removal of CO adsorbed on Pt as follows.[14-17]

$$Pt + CH_3OH \ \rightarrow \ Pt-(CH_3OH)_{ads} \qquad\qquad (3\text{-}1)$$

$$Pt-(CH_3OH)_{ads} \ \rightarrow \ Pt-(CO)_{ads} + 4H^+ + 4e^- \qquad (3\text{-}2)$$

$$Ru + H_2O \ \rightarrow \ Ru-OH + H^+ + e^- \qquad\qquad (3\text{-}3)$$

$$Pt-(CO)_{ads} + Ru-OH \ \rightarrow \ Pt + Ru + CO_2 + H^+ + e^- \qquad (3\text{-}4)$$
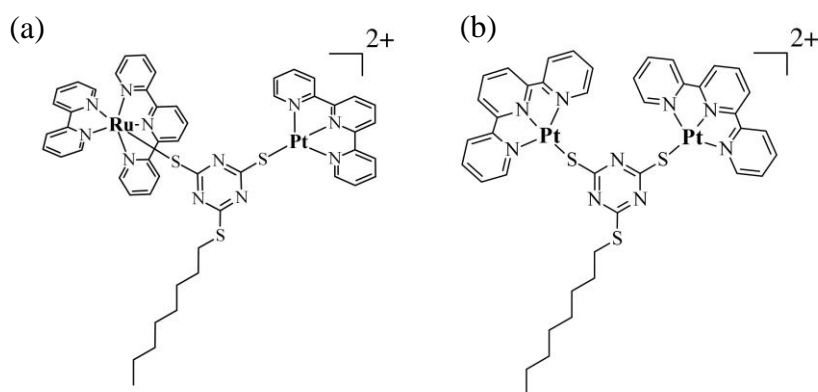
Figure 3-1. Structures of (a) Pt-Ru complex and (b) Pt-Pt complex.

Metallic Ru and RuO$_x$ and RuO$_x$H$_y$ species can provide active oxidants such as surface Ru–OH, leading to the enhancement of MOR activity.[18, 19] A randomly mixed Pt-Ru alloy with an equal ratio of metals is considered to be the most active electrocatalyst for MOR.[3] One of the most conventional methods for alloy preparation is the electrochemical and chemical reduction of mixed metal salts. Atomically mixed Au-Pd[20] and Ag-Rh alloys[21] are reported to be prepared using these methods. However, it is difficult to prepare a Pt-Ru alloy by these methods because of phase separation.[22-24] It is also difficult to control surface composition.[25-27]

There are several reports for preparing alloy catalysts via the decomposition of hetero multi-nuclear complexes with easily controllable metal distances and ratio.[28-34] Uehara prepared a Pt-Ru alloy from a new Pt-Ru complex, [Pt^{II}(tpy)Ru^{II}(bpy)(tpy)(μ-otd)](PF$_6$)$_2$ (tpy = 2,2':6',2''-terpyridine, bpy = 2,2'-bipyridine, μ-otd = 2-octylthio-4,6-disulfanyl-1,3,5-triazine), as shown in Figure 3-1 (a). Au(111) was modified with the Pt-Ru complex and heated at 300ºC under O$_2$ flow to form the Pt-Ru alloy. The formation of the Pt-Ru alloy with a height of 0.3 nm and a diameter of 3.1 nm was confirmed by STM (Figure 3-2 (c)). The MOR activity of Pt-Ru alloy prepared from Pt-Ru complex was much higher than that of poly Pt in an alkaline solution (Figure 3-3).[35, 36] The two-dimensional Pt-Ru alloy likely acts as a good MOR catalyst, and it is expected that even better catalysts can be obtained by increasing the surface coverage of Pt-Ru alloys.
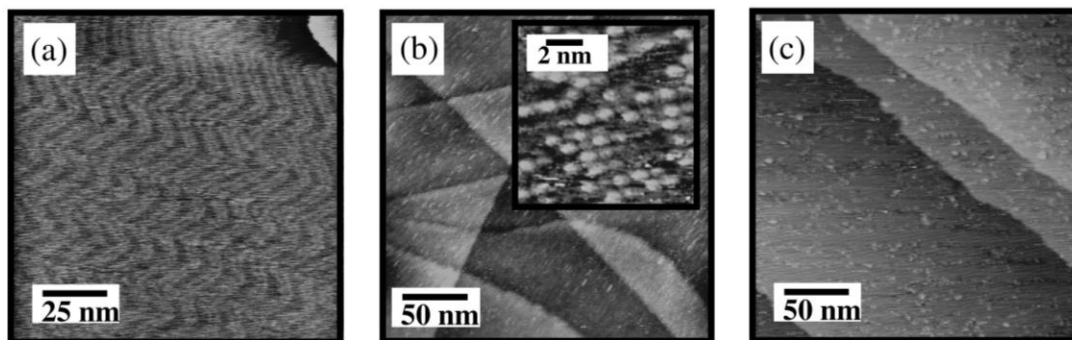
Figure 3-2. A STM image of bare Au(111). (b) STM images of Au(111) modified with Pt-Ru complex; (inset) High resolution STM image (E_{bias} = 0.6 V, I_{tc} = 0.1 nA). (C) A STM image of the heat treated Pt-Ru complex at 300°C. (E_{bias} = 0.1 V, I_{tc} = 0.5 nA).[34]
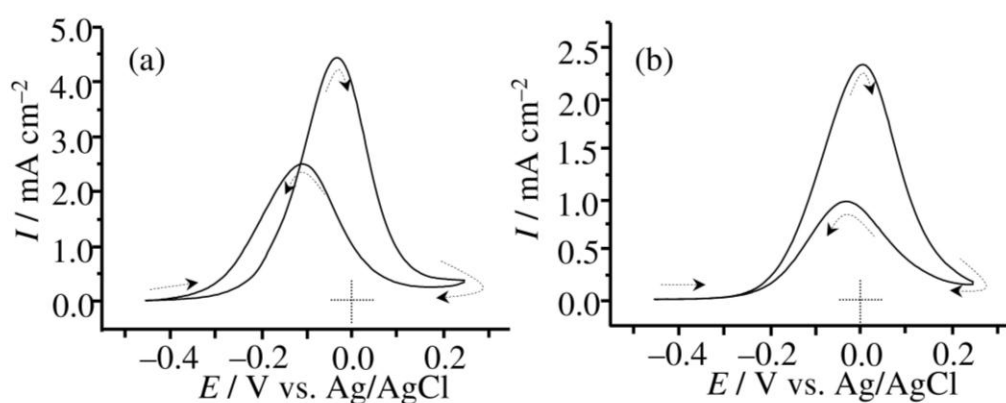
Figure 3-3. CVs of (a) poly Pt and (b) Pt-Ru alloy on Au(111) prepared from Pt-Ru complex in 0.1 M KOH solution containing 1 M methanol. Scan rate = 50 mV s^{-1}.[34]

In this chapter, Pt-Ru alloys were prepared by repeating the cycle of Pt-Ru complex adsorption and heat treatment, and the effect of surface coverage of Pt-Ru alloy prepared from Pt-Ru complex on MOR activity was investigated in acidic and alkaline solutions. The Pt-Ru alloys prepared by repeating a cycle of Pt-Ru complex adsorption and heat treatment are called n-Pt-Ru/Au (n is the number of Pt-Ru complex adsorption and heat treatment cycles.). The MOR activity of the Pt-Ru alloy with high coverage was compared with those of poly Pt and Au(111) modified with Pt prepared by repeating the cycle of adsorption and pyrolysis for Pt-Pt complex, [Pt^{II}(tpy)2(μ–otd)](PF$_6$)$_2$ shown in Figure 3-1 (b), in acidic and alkaline solutions. Au(111) modified with Pt prepared by repeating a cycle of Pt-Pt complex adsorption and heat treatment is called n-Pt/Au (n is the number of the Pt-Pt complex adsorption and heat treatment cycles.). Finally, the

electrocatalytic activities of several reactions related to the fuel cell of Pt-Ru alloy on Au(111) prepared from the Pt-Ru complex, were compared with those of Pt-Ru alloy on Au(111) prepared from a mixture of K_2PtCl_4 and $RuCl_3$ (denoted as Pt-Ru$_{mix}$/Au).

3.2   Results and Discussions

3.2.1   Effect of the number of adsorption/heat treatment cycles of Pt-Ru complex on the surface coverage and MOR activity of Pt-Ru alloy

3.2.1.1 STM

Figure 3-4 shows STM images of (a) 3-Pt-Ru/Au, (b) 9-Pt-Ru/Au, (c) 15-Pt-Ru/Au and (d) 24-Pt-Ru/Au. The surface of bare Au(111) was atomically flat, as shown in Figure 3-2 (a). However, in the STM images in Figure 3-4, island structures were observed and these structures increased with repeating cycles of Pt-Ru complex adsorption and decomposition, suggesting the island structures corresponding to the Pt-Ru alloys. In the case of 1-Pt-Ru/Au, the monoatomic height of Pt-Ru alloys with diameters of 3.13 nm were observed (Figure 3-2 (b)).

For 3-Pt-Ru/Au and 9-Pt-Ru/Au, a surface coverage increase of the Pt-Ru alloys with a monoatomic height was observed (Figures 3-4 (a) and (b)). The cross section shown in Figure 3-4 (b) clearly shows the the obtained Pt-Ru alloys have monoatomic height, suggesting that they grow two-dimensionally. However, the surface coverage of Pt-Ru alloy was still low, and large terraces and monoatomic steps of gold from Au(111) were clearly observed.

In 15-Pt-Ru/Au, islands of a few atomic heights were observed in addition to the monoatomic height islands (Figure 3-4 (c)).

In 24-Pt-Ru/Au, the number of islands with a few atomic height increased compared to 15-Pt-Ru/Au (Figure 3-4 (d)). It was more difficult to observe the terraces and monoatomic steps of gold from Au(111), suggesting that the surface coverage of the Pt-Ru alloy significantly increases. The STM measurements revealed that Au(111) is modified with well-dispersed Pt-Ru alloys within a few atomic height after the

cycle of Pt-Ru complex adsorption and heat treatment.
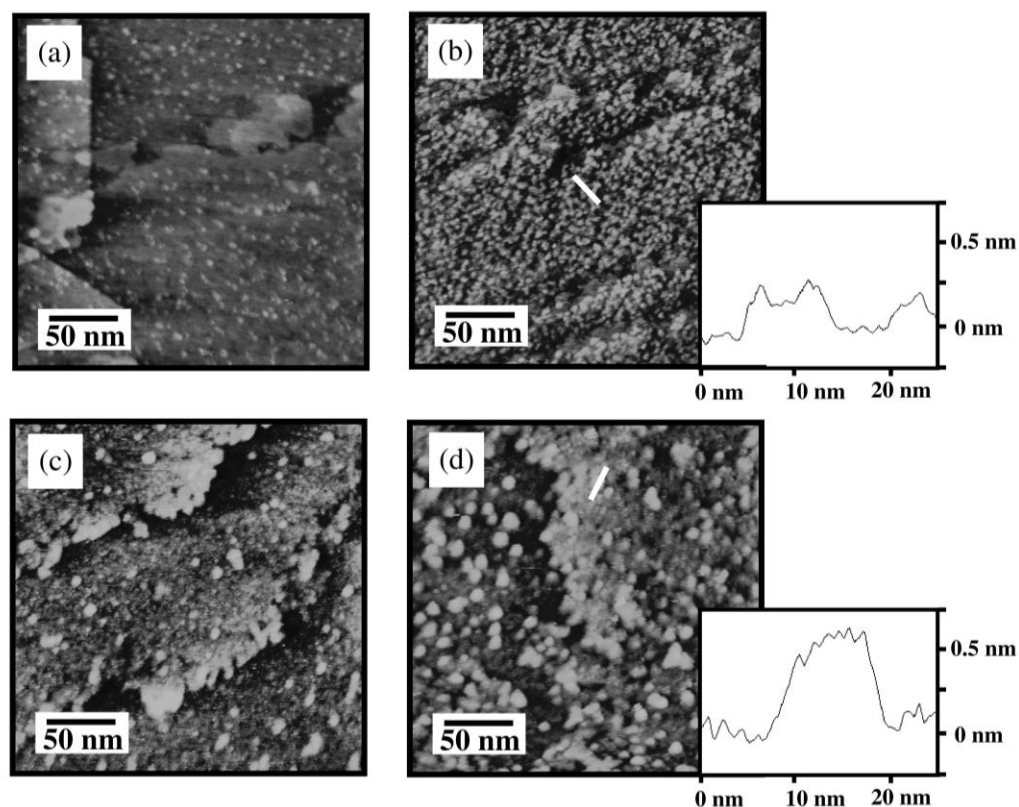
Figure 3-4. STM images of (a) 3-Pt-Ru/Au, (b) 9-Pt-Ru/Au, (c) 15-Pt-Ru/Au, and (d) 24-Pt-Ru/Au (E_{bias} = 0.1 V, I_{tc} = 0.5 nA).

3.2.1.1 XPS
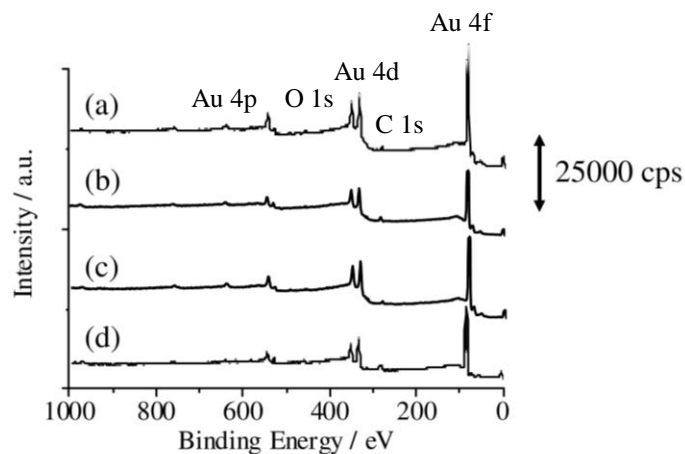
Figure 3-5. Wide-scan XP spectra of (a) bare Au, (b) Pt-Ru complex on Au, (c) 1-Pt-Ru/Au, and (d) 24-Pt-Ru/Au.

Figures 3-5 and Figure 3-6 show wide- and narrow-scan XP spectra of (a) bare Au, (b) Au modified

with Pt-Ru complex, (c) 1-Pt-Ru/Au, and (d) 24-Pt-Ru/Au.

The wide- and narrow-scan XP spectra of a bare Au surface (Figure 3-5 (a), Figure 3-6 (a)) showed only peaks corresponding to Au, C, and O. The peaks corresponding to C 1s and O 1s appeared at 284.6 and 532.5 eV, respectively, and these peaks were caused by organic contamination.

After Au was modified with Pt-Ru complex, which is composed of bivalent center metals and ligands such as bi-pyridine, peaks corresponding to Pt 4f, Ru 3d, and N 1s appeared (Figure 3-6 (b)). The Pt $4f_{7/2}$ and Pt $4f_{5/2}$ overlapped with the Au $5p_{1/2}$ were observed at 73.3 and 76.6 eV, respectively. This was 2.1 eV higher than bulk Pt(0),[37] suggesting that Pt is bivalent. In the Ru 3d region, two peaks were observed at 280.8 and 285.8 eV, corresponding to Ru $3d_{5/2}$ and Ru $3d_{3/2}$ with C 1s overlap, respectively. The peak

Figure 3-6. Narrow-scan XP spectra in the Pt 4f (A), Ru 3d (B), O 1s (C), and N 1s (D) regions of (a) bare Au, (b) Pt-Ru complex on Au, (c) 1-Pt-Ru/Au, and (d) 24-Pt-Ru/Au.

corresponding to Ru $3d_{5/2}$ was 0.7 eV higher than that of bulk Ru(0),[37] suggesting bivalent Ru. The position of the C 1s peak was 1.2 eV higher than that 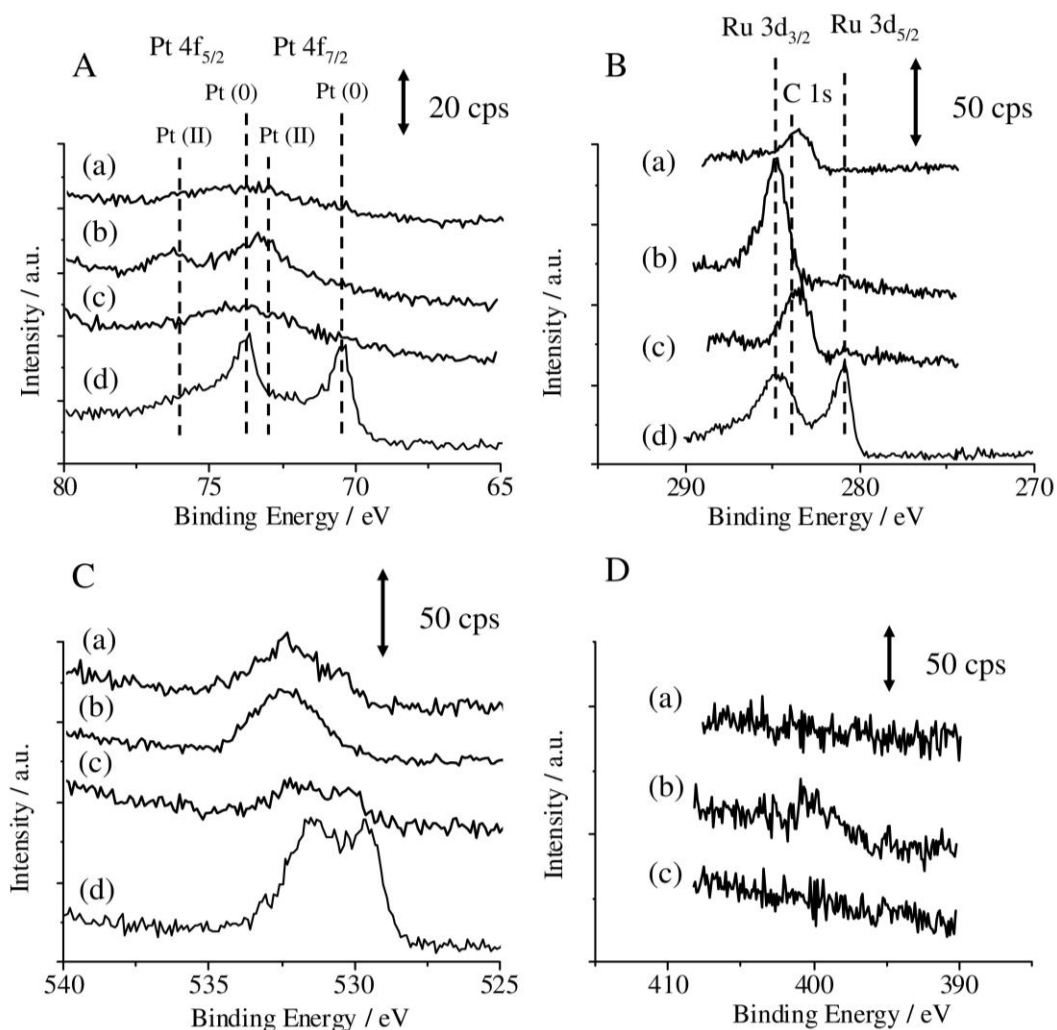of amorphous carbon (284.6 eV). The peak originates from aromatic carbon.[38] The peak in the N 1s region was observed at 399.7 eV and corresponds to pyridine-like nitrogen coordinated to metal.[39] The peak of O 1s was observed at 532.5 eV, and the peak position was the same as that of bare Au. From these results, the adsorption of Pt-Ru complex on the Au surface was confirmed.

Figure 3-6 (c) shows the XP spectra of Pt 4f (A), Ru 3d (B), O 1s (C) and N 1s (D) regions of 1-Pt-Ru/Au. The peaks of Pt 4f became broader than those of Pt 4f in Pt-Ru complex. Electrochemical results show that the Pt of 1-Pt-Ru/Au is on Au (c.f. section 3.2.1.3). The XP spectra of Au modified with Pt, prepared by the pyrolysis of Pt-Pt complex monolayer, clearly showed that the deposited Pt was composed of metallic Pt and Pt(II) oxides (c.f. section 3.2.2). In the Ru 3d region (Figure 3-6 (c)), two peaks were observed at 280.8 and 284.6 eV, corresponding to Ru $3d_{5/2}$ and Ru $3d_{3/2}$, respectively. The peak intensity of Ru $3d_{3/2}$ was smaller than that of Ru $3d_{5/2}$, but it overlapped with the C 1s peak. The peak position of Ru $3d_{5/2}$ was same as that of Pt-Ru complex. In the O 1s region, two peaks were observed at 530.0 and 532.5 eV, corresponding to metal oxides and organic contamination, respectively.[40] These results indicate the formation of a Ru oxide. The peak position of C 1s was lower than that of Pt-Ru complex, but it was the same as that of bare Au, suggesting the presence of decomposed aromatic carbon. The N 1s peak was not observed, and this was likely because of ligand pyrolysis. Thus, XPS measurements confirmed the pyrolysis of organic ligands and the presence of central metals on Au after heat treatment at 300 ℃ under O_2 flow.

Figure 3-6 (d) shows the XP spectra of Pt 4f (A), Ru 3d (B) and O 1s (C) regions of 24-Pt-Ru/Au. The XP spectra peak intensities in the Pt 4f, Ru 3d, and O 1s regions increased with the cycles of Pt-Ru complex adsorption and heat treatment, suggesting that the surface coverage of Pt-Ru alloy increases. The peaks corresponding to Pt $4f_{7/2}$ and Pt $4f_{5/2}$ were observed at 70.5 eV and 73.5 eV, respectively. The peak position of Pt 4f was 0.7 eV lower than that of bulk Pt (0). This lower peak position can be explained by an

electronic structure change in Pt by the Au substrate.[8] The peaks corresponding to Ru $3d_{5/2}$ and O 1s were observed at 280.8 and 530.0 eV, respectively. According to results reported by Kotz et al., the O 1s peaks corresponding to H_2O, OH^-, and O^{2-} were observed in bulk RuO_2.[40] The XP spectrum of O 1s shown in Figure 3-6 (d) also contained peaks corresponding to H_2O (532.6 eV), OH^- (531.1 eV), and O^{2-} (529.4 eV). The peak position of Ru $3d_{5/2}$ in 24-Pt-Ru/Au was similar to that of bulk RuO_2. The appearance of the O 1s peak corresponding to O^{2-} also indicates RuO_2 formation. The relative amount of Pt and Ru on the surface can be determined by XPS by the following equation.[41]

$$C_{Pt}/C_{Ru} = ((I_{Pt}/R_{Pt})/(I_{Ru}/R_{Ru}) \qquad (3\text{-}5)$$

where C is the concentration, I is the peak area, and R is the relative sensitivity factor of the elements. Using the R_{Pt} and R_{Ru} values of 2.55 and 1.30,[41] the Pt/Ru ratio was estimated to be 0.5. This number indicates that some of the Pt atoms probably diffused into the Au substrate during heat treatment.

3.2.1.3   Electrochemical properties

Figure 3-7 shows the CVs of (a) bare Au, (b) 1-Pt-Ru/Au, (c) 3-Pt-Ru/Au, (d) 9-Pt-Ru/Au, (e) 24-Pt-Ru/Au, and (f) 32-Pt-Ru/Au in 0.1 M $HClO_4$ solutions. The potentials was cycled between –0.2 and 0.9 V (gray) and between –0.2 and 1.45 V (black). The current was normalized by the surface area of Au(111) before Pt-Ru alloy modification. In Figure 3-7 (a), current peaks corresponding to surface reconstruction (0.35 V), Au oxide formation (1.1, 1.4 V), and Au oxide reduction (0.9 V) were observed. Compared to the CV of Au(111) in 50 mM H_2SO_4 solution in Figure 2-1, Au oxide formation in Figure 3-7 (a) began at a more negative potential. The pre-oxidation peak observed at 1.1 V corresponds to OH adsorption on Au(111). OH adsorption on Au(111) in a 0.1 M $HClO_4$ solution started at a more negative potential compared to the potentials in a 50 mM H_2SO_4 solution. This is because ClO_4^- has less adsorption ability against Au(111) surface than HSO_4^- and SO_4^{2-}.[42]
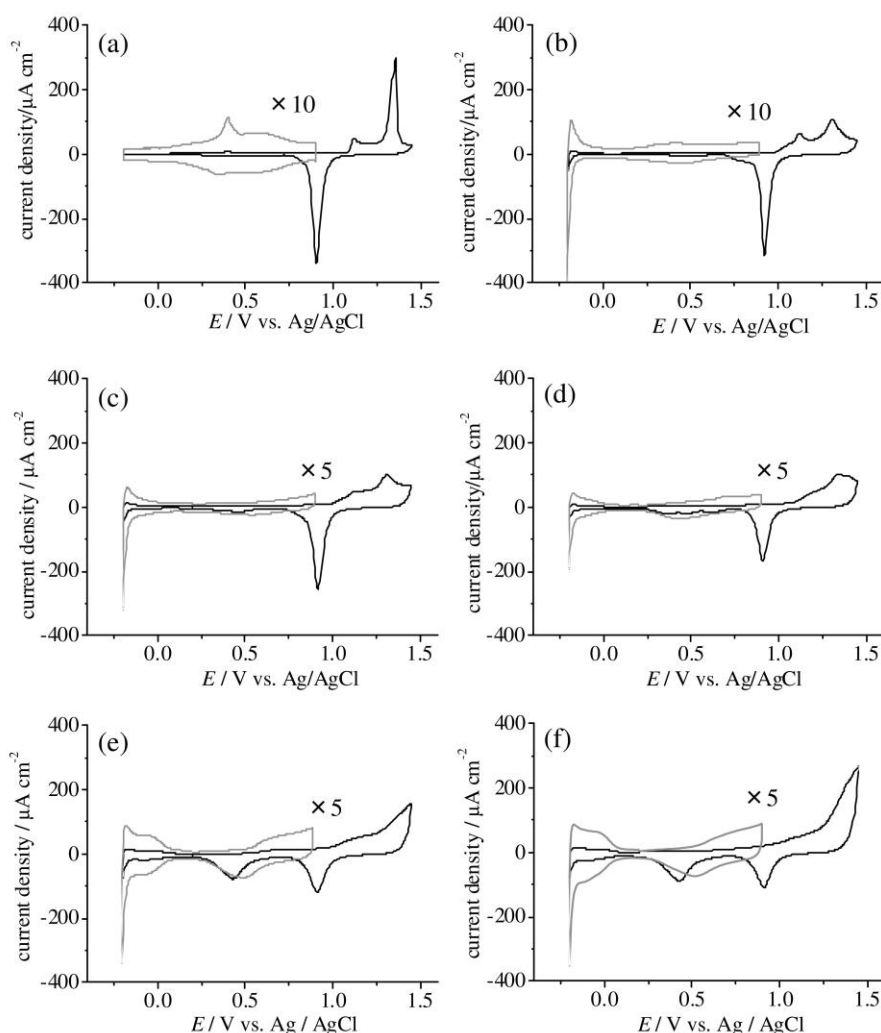
Figure 3-7. CVs of (a) bare Au(111), (b) 1-Pt-Ru/Au, (c) 3-Pt-Ru/Au, (d) 9-Pt-Ru/Au, (e) 24-Pt-Ru/Au, and (f) 32-Pt-Ru/Au in 0.1 M HClO$_4$ solutions. Scan rate = 50 mV s^{-1}.

After Pt-Ru complex adsorption and heat treatment on Au(111), the electrochemical properies of bare Au(111) changed (Figures 3-7 (b)-(f)). The peak current of the Au oxide reduction decreased as the cycle of Pt-Ru complex adsorption and heat treatment on Au(111) was repeated. The charge difference in the Au oxide reduction reaction of bare Au(111) and Au(111) modified with a Pt-Ru alloy (θ_{Pt-Ru}) was utilized to estimate the surface coverage of Pt-Ru alloy on Au(111). The ratio of Pt in Pt-Ru alloys was estimated by dividing the charge of Pt hydrogen adsorption (θ_{Pt}) by θ_{Pt-Ru}. The electrochemically determined values are summarized in Table 3-1.

For 1-Pt-Ru/Au and 3-Pt-Ru/Au, the peak current of Au oxide reduction decreased (Figures 3-7 (b)-(c),

48

Table 3-1. Summary of surface coverage of Pt and Pt-Ru alloy on Au(111). The charge of hydrogen adsorption and Au oxide reduction reactions were utilized for estimation of θ_{Pt} and θ_{Pt-Ru}. The ratio of Pt in the Pt-Ru alloys was estimated by dividing θ_{Pt} by θ_{Pt-Ru}

Sample	Hydrogen adsorption		Oxide reduction		Ratio of Pt (%)
	Q_H / µC cm^{-2}	θ_{Pt} (%)	Q_{Au} / µC cm^{-2}	θ_{Pt-Ru} (%)	
1-Pt-Ru/Au(111)	——	——	418	5.8	——
3-Pt-Ru/Au(111)	——	——	408	8.2	——
9-Pt-Ru/Au(111)	8.6	3.8	333	25.0	15.2
24-Pt-Ru/Au(111)	35.7	15.5	248	44.2	35.1 (32.4)*
32-Pt-Ru/Au(111)	41.0	17.8	225	49.3	36.1

*Estimated by the result of XPS

black curve). The surface coverage for Pt-Ru alloys of 1-Pt-Ru/Au and 3-Pt-Ru/Au were estimated to be 5.8% and 8.2%, respectively. The current peak corresponding to the Pt oxide reduction reaction appeared around 0.5 V. In the gray curve, the cathodic and anodic currents corresponded to the hydrogen evolution and oxidation reactions (HER, HOR), and typical electrochemical properties of Pt were observed at –0.18 V. Meanwhile, the hydrogen adsorption/desorption current, which is also a typical electrochemical property of Pt, was not clearly observed, and θ_{Pt} could not be estimated. The broadened oxidation and reduction current waves were observed at 0.5 V vs. Ag/AgCl, corresponding to OH adsorption/desorption on Pt.

In 9-Pt-Ru/Au, the peak current of Au oxide reduction reaction decreased (Figure 3-7 (d), black curve). The surface coverage of Pt-Ru alloy of 9-Pt-Ru/Au was estimated to be 25.0%. The current peak corresponding to the Pt oxide reduction reaction increased. On the gray curve, currents corresponding to HER, HOR, and OH adsorption/desorption were observed. Compared with 1-Pt-Ru/Au and 3-Pt-Ru/Au, the hydrogen adsorption/desorption current was clearly observed, and θ_{Pt} was estimated to be 3.8%.

For 24-Pt-Ru/Au and 32-Pt-Ru/Au, a decrease in the peak current of Au oxide reduction reaction and an increase in the peak current of Pt oxide reduction reaction was clearly observed (Figures 3-7 (e)-(f), black curve). The surface coverage of Pt-Ru alloy of 24-Pt-Ru/Au and 32-Pt-Ru/Au was estimated to be 44.2% and 49.3%, respectively. The current corresponding to hydrogen adsorption/desorption increased (gray curve). The currents corresponding to HER, HOR and OH adsorption/desorption were observed.

From the electrochemical results, the ratio of Pt in Pt-Ru alloy ($\theta_{Pt}/\theta_{Pt-Ru}$) was estimated to be 15.2% for

9-Pt-Ru/Au, 35.1% for 24-Pt-Ru/Au and 36.1% for 32-Pt-Ru/Au (Table 3-1). From XPS analysis, the ratio of Pt in 24-Pt-Ru/Au was estimated to be 32.4%. The ratios of Pt in Pt-Ru alloys with low coverage estimated by electrochemical measurements (1-Pt-Ru/Au, 3-Pt-Ru/Au, 9-Pt-Ru/Au) were lower than those estimated by XPS measurements. The electrochemical properties of Pt-Ru alloys with a surface coverage of less than 25% were different from those of the bulk Pt-Ru alloy, suggesting that the electronic structure of a low-coverage Pt-Ru alloy is different than that of bulk Pt-Ru alloy.

3.2.1.4   Relation between surface coverage and MOR activity

Figure 3-8 shows the CVs of (i) 1-Pt-Ru/Au, (ii) 3-Pt-Ru/Au, (iii) 9-Pt-Ru/Au, (iv) 24-Pt-Ru/Au and (v) 32-Pt-Ru/Au obtained in (a) 0.1 M HClO$_4$ solution containing 1 M methanol and (b) 0.1 M KOH solution containing 1 M methanol. The current was normalized on the basis of the surface area of Au(111) before
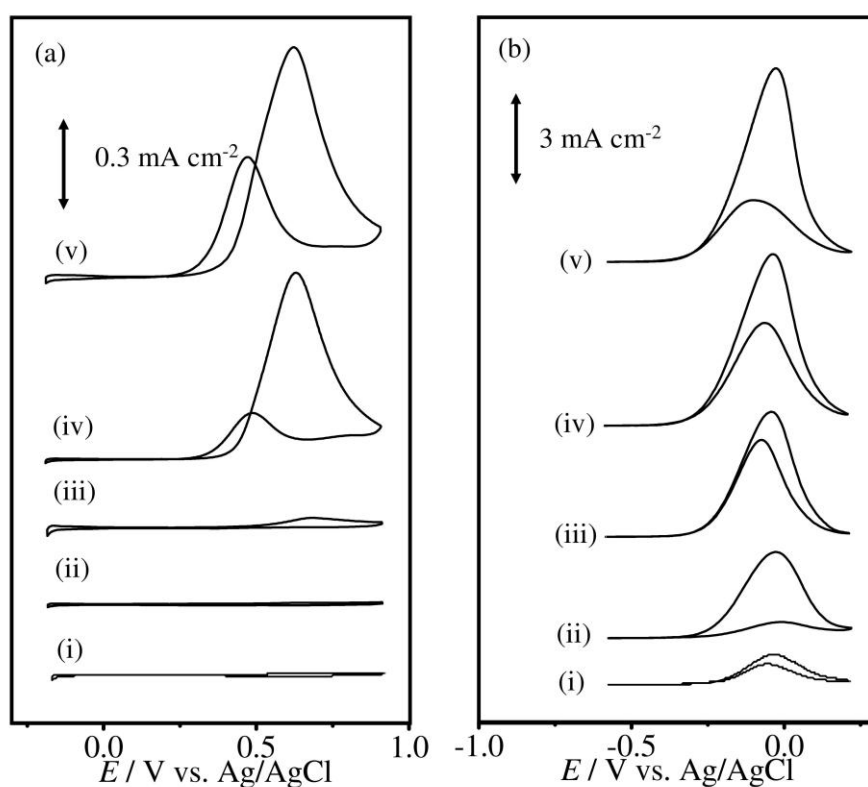

Figure 3-8. CVs of (i) 1-Pt-Ru/Au, (ii) 3-Pt-Ru/Au, (iii) 9-Pt-Ru/Au, (iv) 24-Pt-Ru/Au, and (v) 32-Pt-Ru/Au in (a) 0.1 M HClO$_4$ and (b) 0.1 M KOH solutions containing 1 M methanol. Scan rate = 50 mV s^{-1}.

50

Pt-Ru alloy modification. In Figure 3-8 (a), the oxidation current corresponding to MOR was observed for 9-Pt-Ru/Au, 24-Pt-Ru/Au, and 32-Pt-Ru/Au at around 0.65 V. In Figure 3-8 (b), the oxidation current corresponding to MOR was observed for all electrodes around –0.05 V. While the Pt-Ru alloys with low coverage (lower than 25%) showed MOR activity only in alkaline solution, Pt-Ru alloys with higher coverage showed MOR activity in alkaline and acidic solutions. The peak current densities and peak potentials of MOR in 0.1 M HClO$_4$ and 0.1 M KOH solutions of Pt-Ru alloys were summarized in Tables 3-2 and 3-3, respectively. The MOR activities of low-coverage Pt-Ru alloys were different from those of high-coverage Pt-Ru alloys. The peak current densities of MOR for a forward scan (I_{peak}) were plotted against the surface coverage of Pt-Ru alloy.

In the case of MOR in acidic solutions (Figure 3-9 (a)), Pt-Ru alloys with surface coverages lower than 25 % did not show any MOR activity. As the surface coverage of Pt-Ru alloy increased, the peak current densities increased, suggesting that I_{peak} has no correlation with the surface coverage of Pt-Ru alloy. STM measurements showed that the Pt-Ru alloy with monoatomic heifht was observed for 1-Pt-Ru/Au, 3-Pt-Ru/Au, and 9-Pt-Ru/Au, and the Pt-Ru alloy with a few atomic heights was observed for 15-Pt-Ru/Au and 24-Pt-Ru/Au. The electronic structure of Pt-Ru alloy with monoatomic height was probably different from that of a Pt-Ru alloy with a few atomic heights. The Pt-Ru alloy with a few atomic heights can act as a MOR active site in acidic solution.

In the case of MOR in alkaline solutions (Figure 3-9 (b)), all electrodes showed MOR activity, and their peak current densities got increased as the cycles of Pt-Ru complex adsorption and heat treatment repeated. This suggested that the I_{peak} has a correlation with the surface coverage of Pt-Ru alloy. The electronic structure of Pt-Ru alloy with low coverage was probably different from that of Pt-Ru alloy with high coverage and therefore Pt-Ru alloy with low coverage showed MOR activity only in alkaline solution. It was reported that Au has MOR activity in alkaline solutions.[43, 44] A Pt-Ru alloy with monoatomic height probably has electrochemical properties similar to Au. Not only the Pt-Ru alloy with a few atomic heights but also the Pt-Ru alloy with monoatomic height can act as MOR active sites in alkaline solutions.

51

Thin foreign metals on noble metals and noble metal nanoparticles often have different physical properties and electrocatalytic activities from bulk metals.[45-57] Our group revealed the differences in geometric and electronic structures between submonlayer Pd on Au and bulk Pd using surface X-ray scattering (SXS)[45] and second-harmonic generation (SHG)[46] measurements. The electronic structure of the submonolayer Pd film on Au single crystals was strongly affected by Au and showed unique electrocatalytic activities against formaldehyde oxidation[47] and oxygen reduction reactions.[48]

Table 3-2. Summary of peak potentials and peak current densities of MOR of Pt-Ru alloys in 0.1 M HClO$_4$ solutions.

Sample	Positive Scan		Negative scan	
	I_{peak} / mA cm^{-2}	E_{peak} / V	I_{peak} / mA cm^{-2}	E_{peak} / V
1-Pt-Ru/Au(111)	——	——	——	——
3-Pt-Ru/Au(111)	——	——	——	——
9-Pt-Ru/Au(111)	0.04	0.67	——	——
24-Pt-Ru/Au(111)	0.89	0.63	0.24	0.47
32-Pt-Ru/Au(111)	0.95	0.61	0.49	0.46

Table 3-3. Summary of peak potentials and peak current densities of MOR of Pt-Ru alloys in 0.1 M KOH solutions.

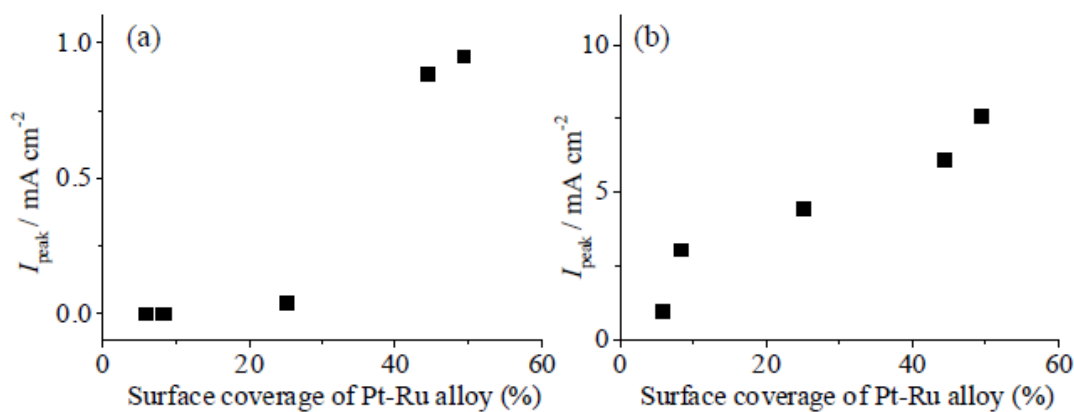| Sample	Positive Scan		Negative scan	
	I_{peak} / mA cm^{-2}	E_{peak} / V	I_{peak} / mA cm^{-2}	E_{peak} / V
1-Pt-Ru/Au(111)	1.02	-0.07	0.70	-0.07
3-Pt-Ru/Au(111)	3.08	-0.05	0.56	-0.03
9-Pt-Ru/Au(111)	4.49	-0.06	3.48	-0.09
24-Pt-Ru/Au(111)	6.17	-0.05	3.70	-0.07
32-Pt-Ru/Au(111)	7.65	-0.05	2.79	-0.11

Figure 3-9. Plots of the peak current densities of MOR at positive scan (I_{peak}) against surface coverages of Pt-Ru alloy. (a) MOR in 0.1 M HClO$_4$ solutions. (b) MOR in 0.1 M KOH solutions.
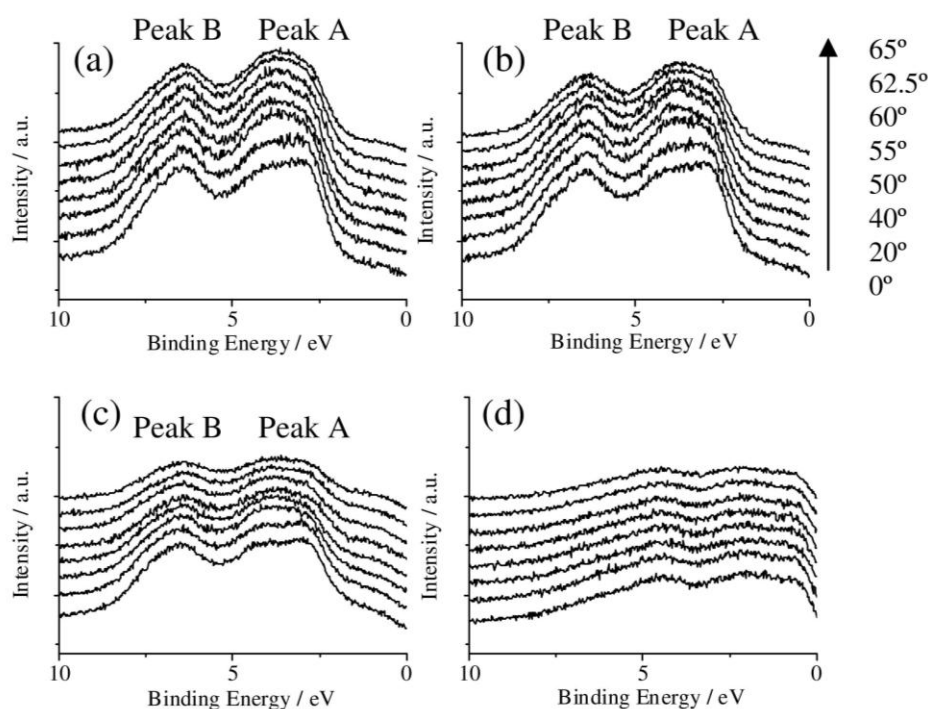
Figure 3-10. ARXP spectra of (a) bare Au, (b) 9-Pt-Ru/Au, (c) 32-Pt-Ru/Au, and (d) poly Pt in the valence-band region obtained by MgKa radiation. Photoelectron emission angle: 0, 20, 40, 50, 55, 60, 62.5 and 65°.

The difference in the electronic structure between 9-Pt-Ru/Au and 32-Pt-Ru/Au was investigated by

angle-resolved X-ray photoelectron spectroscopy (ARXPS) in the valence-band region. Figure 3-10 shows

the ARXP spectra in the valence-band region of (a) Au, (b) 9-Pt-Ru/Au, (c) 32-Pt-Ru/Au and (d) Pt with

photoelectron emission angles at 0, 20, 40, 50, 55, 60, 62.5, and 65°. The obtained XP spectra of Au and Pt

with photoelectron emission angles at 0° were similar to those previously reported.[58] In Figure 3-10 (a),

three peaks were observed at 2.8, 3.8, and 6.5 eV. In Figure 3-10 (d), three peaks were observed at 0.6, 1.8

and 4.2 eV. It has been reported that the valence-band spectra of RuO_2 are composed of three peaks

corresponding to Ru-Oπ* (0.6 eV), Ru-Oπ (4.7 eV) and Ru-Oσ (6.9 eV).[59] The shape of valence-band

spectrum of 9-Pt-Ru/Au is very similar to that of Au. Meanwhile, in the valence-band spectrum of

32-Pt-Ru/Au, peaks corresponding to Au, and a shoulder peak corresponding to Pt and RuO_2 were observed

around 0.8 eV. In Figures 3-10 (a)-(c), two peaks were observed around 3.8 eV (peak A) and 6.4 eV (peak

B). The photoelectron emission angles were plotted against the peak positions for peaks A and B (Figure

53

3-11). The positions of peak B for Au, 9-Pt-Ru/Au, and 32-Pt-Ru/Au were similar. On the other hand, the

positions of peak A for Au and 9-Pt-Ru/Au were similar but different from those of 32-Pt-Ru/Au. These

results show that the electronic structure of 9-Pt-Ru/Au is similar to Au, and the electronic structure of

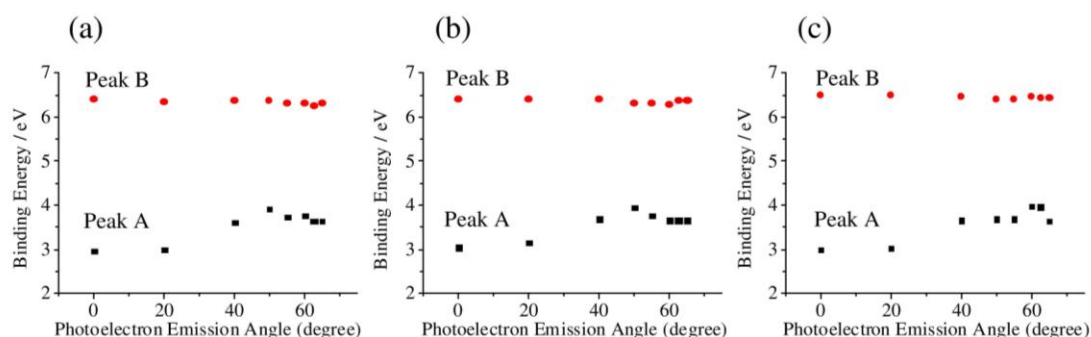32-Pt-Ru/Au is different from Au and 9-Pt-Ru/Au.

Figure 3-11.   The plots of photoelectron emission angles against peak positions of photoelectron of peak A (black square) and peak B (red circle) of (a) bare Au, (b) 9-Pt-Ru/Au, and (c) 32-Pt-Ru/Au.

3.2.2   MOR activity of Au(111) modified with Pt prepared from Pt-Pt complex

Au(111) modified with Pt was prepared from Pt-Pt complex shown in Figure 3-1 (b) to investigate the contribution of Ru to MOR activity in the Pt-Ru alloys prepared from the Pt-Ru complex. Figure 3-12 shows narrow-scan XP spectra in the Pt 4f region of (a) Au modified with Pt-Pt complex, (b) 1-Pt/Au, and (c) 24-Pt/Au. In Figure 3-12 (a),
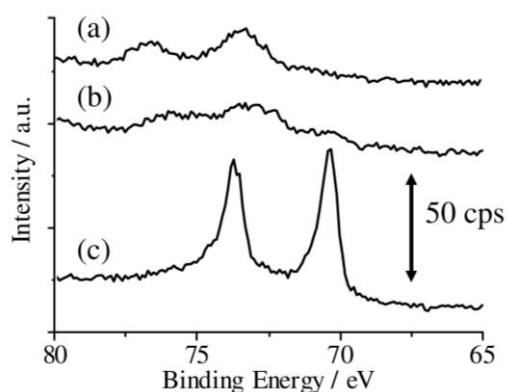
Figure 3-12.   XP spectra in the Pt 4f region of (a) Pt-Pt complex on Au, (b) 1-Pt/Au, and (c) 24-Pt/Au.

two peaks corresponding to Pt $4f_{7/2}$ and Pt $4f_{5/2}$ overlapped with Au $5p_{1/2}$ were observed at 73.3 and 76.6 eV,

respectively. The peak positions of Pt 4f were 2.1 eV higher than those of bulk Pt(0).

After heat treatment (Figure 3-12 (b)), the peak position of Pt $4f_{7/2}$ shifted negatively and split into two

peaks (70.5 eV and 72.2 eV), corresponding to metallic Pt(0) and Pt(II) oxide, respectively.[60]

54

By repeating Pt-Pt complex adsorption and heat treatment 24 times, the intensities of the peaks corresponding to Pt $4f_{7/2}$ and Pt $4f_{5/2}$ increased significantly (Figure 3-12 (c)). The Pt(II) oxides observed in the case of 1-Pt/Au were completely reduced to metallic Pt during the cycles of Pt-Pt complex adsorption and heat treatment.
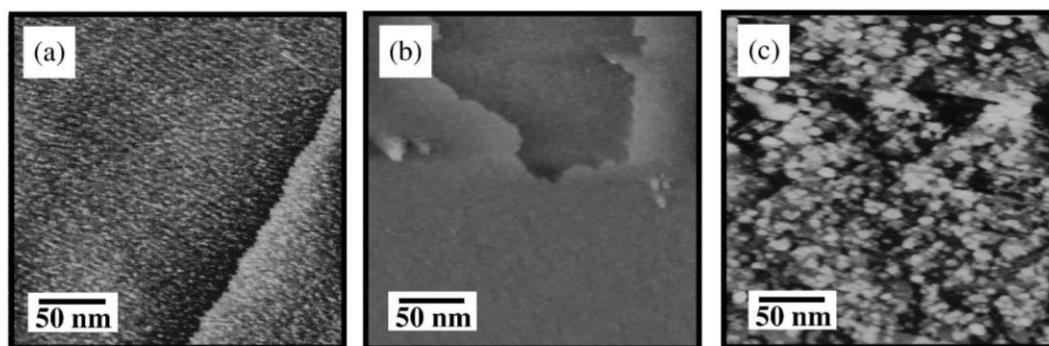
Figure 3-13. STM images of (a) Pt-Pt complex on Au(111), (b) 1-Pt/Au, and (c) 24-Pt/Au. (E_{bias} = 0.1 V, I_{tc} = 0.5 nA).
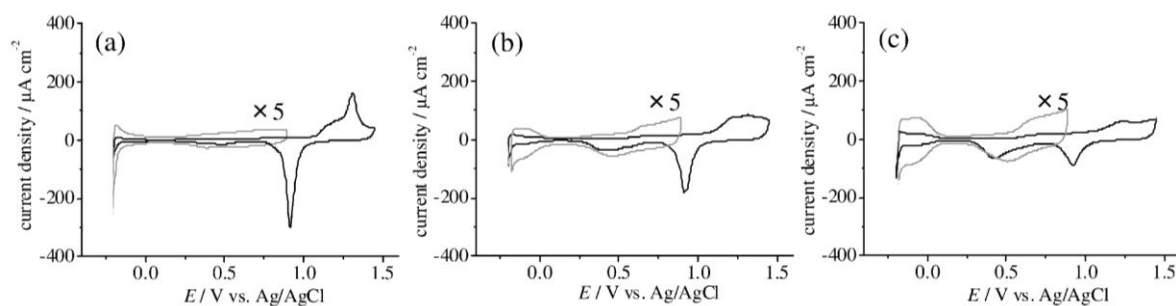
Figure 3-14. CVs of (a) 1-Pt/Au, (b) 9-Pt/Au, and (c) 24-Pt/Au in 0.1 M HClO$_4$ solutions. Scan rate = 50 mV s^{-1}.

Figure 3-13 shows STM images of Au(111) modified with (a) Pt-Pt complex, (b) 1-Pt/Au, and (c) 24-Pt/Au. An ordered Pt-Pt complex layer was not observed (Figure 3-13 (a)). After the decomposition of Pt-Pt complex, Pt islands with a height of 0.2 nm were observed (Figure 3-13 (b)). The surface coverage of Pt islands increased when the cycle of Pt-Pt complex adsorption and heat treatment was repeated 24 times (Figure 3-13 (c)). Figure 3-14 shows the CVs of (a) 1-Pt/Au, (b) 9-Pt/Au, and (c) 24-Pt/Au in 0.1 M HClO$_4$ solution. In Figure 3-14 (a), the potentials cycled between –0.2 and 0.9 V (gray) and between –0.2 and 1.45 V (black), and in Figures 3-14 (b) and (c), the potentials were cycled between –0.17 and 0.9 V (gray) and between –0.2 and 1.45 V (black). The electrochemical properies of 1-Pt/Au are similar to 1-Pt-Ru/Au. An

improvement in HER was observed, but hydrogen adsorption/desorption current was difficult to observe in the case of 1-Pt/Au. For 9-Pt/Au and 24-Pt/Au, the hydrogen adsorption/desorption wave was clearly observed. Figure 3-15 shows the CVs of (i) 1-Pt/Au, (ii) 9-Pt/Au, and (iii) 24-Pt/Au in (a) 0.1 M $HClO_4$ solution containing 1 M methanol and in (b) 0.1 M KOH solution containing 1 M methanol. In Figure 3-15 (a), the oxidation current corresponding to MOR was observed for 9-Pt/Au and 24-Pt/Au at around 0.65 V. In Figure 3-15 (b), the oxidation current corresponding to MOR was observed for all electrodes at –0.05 V Pt with low coverage showed MOR activity only in alkaline solution, and Pt with high coverage showed MOR activity in alkaline and acidic solutions.
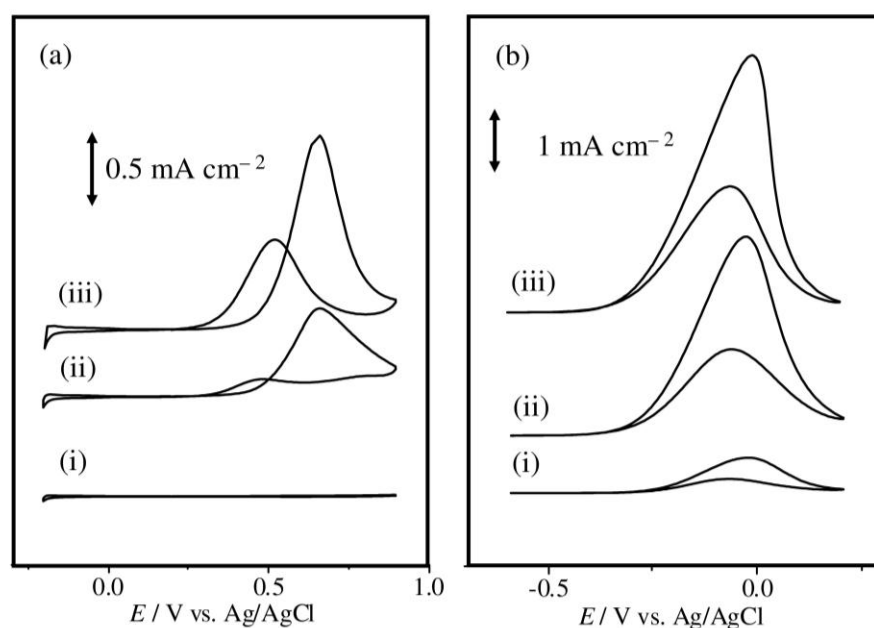
Figure 3-15. CVs of (i) 1-Pt/Au, (ii) 9-Pt/Au, and (iii) 24-Pt/Au in (a) 0.1 M $HClO_4$ and (b) 0.1 M KOH solutions containing 1 M methanol. Scan rate = 50 mV s^{-1}.

3.2.3   Electrochemical behavior of Au(111) modified with Pt-Ru alloy prepared from a mixture of K_2PtCl_4 and $RuCl_3$

A Pt-Ru alloy was prepared from a mixture of K_2PtCl_4 and $RuCl_3$ on Au(111) to investigate the merit of using Pt-Ru complex as a starting material for preparation of high-MOR-activity Pt-Ru alloys. Figures 3-16 (a) and (b) show the CVs of Pt-Ru$_{mix}$/Au and Pt-Ru$_{mix}$/Au (H$_2$) in 0.1 M $HClO_4$ solutions. The current was normalized on the basis of the surface area of Au(111) before any Pt-Ru alloy modification. At both

56

electrodes, a reversible redox wave, corresponding to the hydrogen adsorption/desorption on Pt began to flow at 0.05 V. In the more negative potential region, a sharp reductive current, due to Pt-catalyzed HER catalyzed was observed. When the potential swept to a positive potential, a quasi-reversible wave, corresponding to OH adsorption/desorption on Pt was observed at around 0.6 V. As the positive sweep continued, a clear increase in the oxidation current, caused by oxide formation reactions at Au and Pt and oxygen evolution reactions (OER), was observed. As the sweep went negative, two reduction current peaks, corresponding to Au and Pt oxide reduction reactions, were observed at 0.99 and 0.40 V, respectively and they overlapped with reduction reaction of oxygen generated from RuO_2. Figure 3-16 (c) shows the linear sweep voltammograms of 32-Pt-Ru/Au (blue, A), Pt-Ru$_{mix}$/Au (red, B) and Pt-Ru$_{mix}$/Au (H_2) (pink, C) in the OER region. This result clearly shows that Pt-Ru$_{mix}$/Au showed a higher OER activity than 32-Pt-Ru/Au and Pt-Ru$_{mix}$/Au (H_2), suggesting the formation of RuO_2 in Pt-Ru$_{mix}$/Au, which has bulk RuO_2 properties.[61-63]
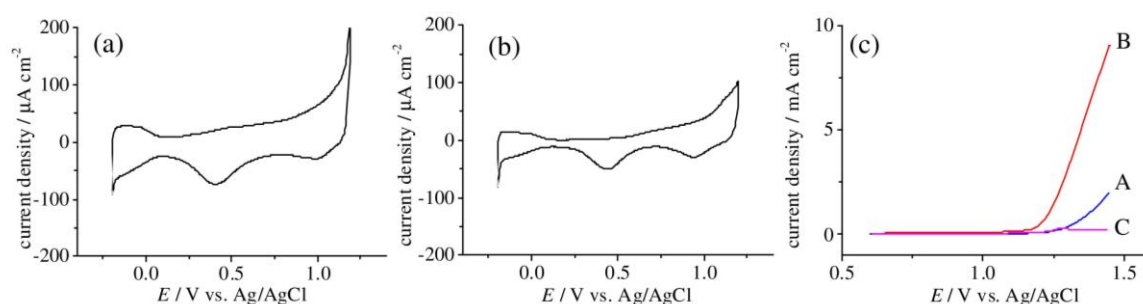
Figure 3-16.   CVs of (a) Pt-Ru$_{mix}$/Au and (b) Pt-Ru$_{mix}$/Au (H_2) in 0.1 M $HClO_4$ solutions. (b) LSVs of 32-Pt-Ru/Au (blue, A) Pt-Ru$_{mix}$/Au (red, B) and Pt-Ru$_{mix}$/Au (H_2) (pink, C) in 0.1 M $HClO_4$ solutions. Scan rate = 50 mV s^{-1}.

3.2.4   Comparison of electrocatalytic activity of Pt-Ru alloy prepared from Pt-Ru complex with that of

other electrocatalysts

3.2.4.1 MOR

Figures 3-17 (a) and (b) show the CVs and current decay curves at 0.4 V vs. Ag/AgCl for poly Pt (green, A), 32-Pt-Ru/Au (blue, B), Pt-Ru$_{mix}$/Au (red, C) 24-Pt/Au (black, D), and Pt-Ru$_{mix}$/Au (H_2) (pink, E) in 0.1 M $HClO_4$ solutions with 1 M methanol. The current was normalized using the Pt surface area estimated

57

Figure 3-17. (a) CVs of poly Pt (green, A), 32-Pt-Ru/Au (blue, B), Pt-Ru$_{mix}$/Au (red, C), 24-Pt/Au (black, D), and Pt-Ru$_{mix}$/Au (H$_2$) (pink, E) in 0.1 M HClO$_4$ solutions with 1 M methanol. Scan rate = 50 mV s^{-1}. (b) Current decay curved of poly Pt (green, A), 32-Pt-Ru/Au (blue, B), Pt-Ru$_{mix}$/Au (red, C), 24-Pt/Au (black, D), and Pt-Ru$_{mix}$/Au (H$_2$) (pink, E) in 0.1 M HClO$_4$ solutions with 1 M methanol at 0.4 V vs. Ag/AgCl. The current was normalized by the surface area of Pt determined from the charge of hydrogen adsorption.

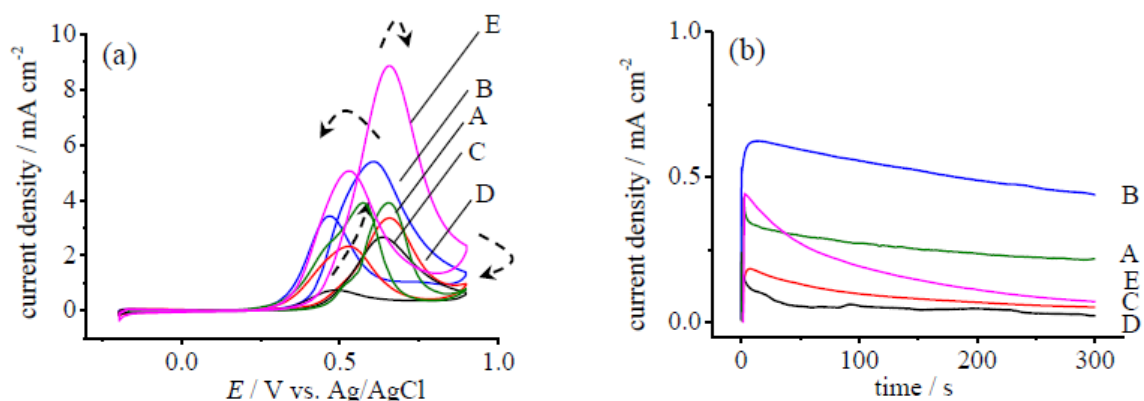**Figure 3-18.** (a) CVs of poly Pt (green, A), 32-Pt-Ru/Au (blue, B), Pt-Ru$_{mix}$/Au (red, C), and 24-Pt/Au (black, D) in 0.1 M KOH solution with 1 M methanol. Scan rate = 50 mV s^{-1}. (b) Current decay curved of the poly Pt (green, A), 32-Pt-Ru/Au (blue, B), Pt-Ru$_{mix}$/Au (red, C), and 24-Pt/Au (black, D) in 0.1 M KOH solutions with 1 M methanol at –0.2 V vs. Ag/AgCl. The current was normalized by the surface area of Pt determined from the charge of hydrogen adsorption.

from the hydrogen adsorption charge. The peak current densities and peak potentials of MOR for poly Pt, 32-Pt-Ru/Au, Pt-Ru$_{mix}$/Au, 24-Pt/Au and Pt-Ru$_{mix}$/Au (H$_2$) in (a) 0.1 M HClO$_4$ solutions are summarized in Table 3-4 (a). For 32-Pt-Ru/Au and Pt-Ru$_{mix}$/Au (H$_2$), the MOR current began flowing at a more negative potential than the other electrodes. On the other hand, no significant enhancement of MOR current was observed with Pt-Ru$_{mix}$/Au. Although the peak current for MOR with Pt-Ru$_{mix}$/Au (H$_2$) is the highest among the five measured electrodes, the MOR current deteriorated to the same level as Pt-Ru$_{mix}$/Au after 300 s (Figure 3-17 (b)). 32-Pt-Ru/Au exhibited a higher MOR activity and durability than Pt-Ru alloys,

prepared from the mixture of K_2PtCl_4 and $RuCl_3$ on Au(111). Figures 3-18 (a) and (b) show the CVs and current decay curves at -0.2 V vs. Ag/A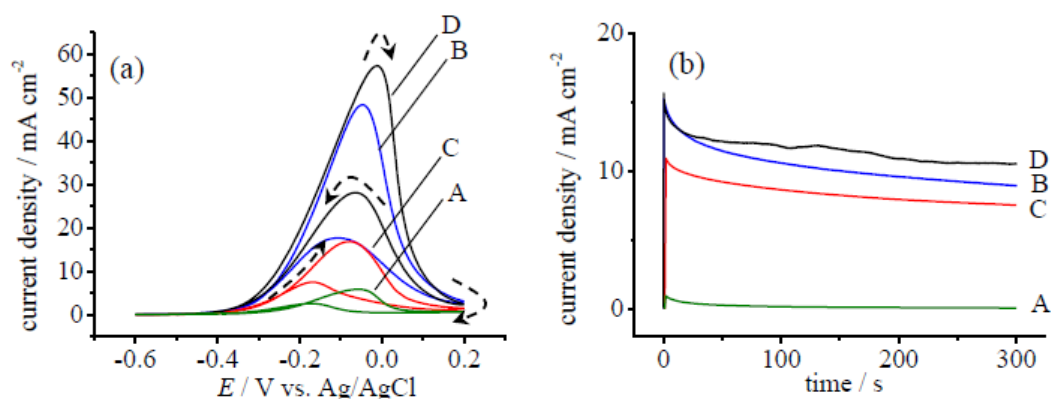gCl for poly Pt (green, A), 32-Pt-Ru/Au (blue, B), Pt-Ru$_{mix}$/Au (red, C), and 24-Pt/Au (black, D) in 0.1 M KOH solutions with 1 M methanol. The peak current densities and peak potentials of MOR for poly Pt, 32-Pt-Ru/Au, Pt-Ru$_{mix}$/Au, and 24-Pt/Au in (a) 0.1 M KOH solutions are summarized in Table 3-4 (b). In the case of MOR in alkaline solutions, 24-Pt/Au exhibited the highest activity and durability for MOR of the four measured electrodes in a 0.1 M KOH solution. From the peak current densities of the MOR forward scan in 0.1 M $HClO_4$ (I_H) and 0.1 M KOH (I_K) solutions, the ratio of peak current densities (I_K/I_H) was estimated to be 1.3 (poly Pt), 8.9 (32-Pt-Ru/Au), 5.3 (Pt-Ru$_{mix}$/Au) and 21.5 (24-Pt/Au). It has been reported that the MOR activity of poly Pt is higher in alkaline solutions than in acidic solutions.[64] Au(111) modified with foreign metals, especially 32-Pt-Ru/Au and 24-Pt/Au had high MOR activity in alkaline solution.

The enhancement may be caused by the difference in electronic structure of Pt and OH adsorbed on Au(111). The XPS results in the Pt 4f region (Figure 3-6 and 3-12) showed that the electronic structure of Pt in 32-Pt-Ru/Au and 24-Pt/Au might be affected by the Au substrate. The peak positions of Pt $4f_{7/2}$ are

Table 3-4. Summary of peak potentials and current densities of MOR of poly Pt, 32-Pt-Ru/Au, Pt-Ru$_{mix}$/Au, 24-Pt/Au, and Pt-Ru$_{mix}$/Au (H$_2$) in (a) 0.1 M $HClO_4$ and (b) 0.1 M KOH solutions.

	Sample	Positive scan		Negative scan	
		E_{peak} / V	I_{peak} / mA cm^{-2}	E_{peak} / V	I_{peak} / mA cm^{-2}
(a)	poly Pt	+0.65	+3.80	+0.46	+3.68
	32-Pt-Ru/Au	+0.60	+5.40	+0.46	+3.42
	Pt-Ru$_{mix}$/Au	+0.66	+3.36	+0.53	+2.33
	24-Pt/Au	+0.64	+2.67	+0.47	+0.75
	Pt-Ru$_{mix}$/Au (H$_2$)	+0.66	+8.84	+0.53	+5.13

	Sample	Positive scan		Negative scan	
		E_{peak} / V	I_{peak} / mA cm^{-2}	E_{peak} / V	I_{peak} / mA cm^{-2}
(b)	poly Pt	−0.12	+5.21	−0.23	+2.64
	32-Pt-Ru/Au	−0.05	+48.30	−0.11	+17.61
	Pt-Ru$_{mix}$/Au	−0.08	+17.80	−0.17	+7.47
	24-Pt/Au	−0.01	+57.50	−0.07	+28.02

71.2 eV (poly Pt), 70.5 eV (32-Pt-Ru/Au), 70.5 eV (24-Pt/Au) and 70.9 eV (Pt-Ru$_{mix}$/Au) (c.f. section

4.2.2). The catalysts with peak positions for Pt $4f_{7/2}$ that were more negative had high MOR activity in

alkaline solutions. Lipkowski et al. reported that OH adsorption on Au(111) starts at –0.36 V vs. Ag/AgCl

in 0.1 M KClO$_4$ with 1 mM KOH solution. The adsorbed OH on Au(111) may accelerate MOR on Pt. In

alkaline solution, the enhancement by Au was so strong that any enhancement by Ru was difficult to

observe.

3.2.4.2   *CO oxidation reaction*

The CO tolerance of poly Pt, 32-Pt-Ru/Au, Pt-Ru$_{mix}$/Au and 24-Pt/Au in 0.1 M HClO$_4$ solution was

investigated. Figure 3-19 shows the CO stripping voltammograms of poly Pt in a 0.1 M HClO$_4$ solution

(first cycle: black, second cycle: gray). The potential was swept from 0.2 V to negative potential and then

swept back to positive potential. In Figure 3-19 (a), the Pt surface was poisoned with CO for 10 s. In the

first cycle, the current of hydrogen adsorption/desorption on Pt was decreased as a result of CO poisoning.

The poly Pt surface was easily covered with CO by CO bubbling for only 10 s. The surface coverage of CO

can be estimated as follows

$$\theta_{CO} = Q_{H2}/Q_{H1} \qquad (3\text{-}6)$$

where Q_{H1} and Q_{H2} are the charges of hydrogen adsorption/desorption before and after CO poisoning,

respectively. The surface coverage of CO in Figure 3-19 (a) was estimated to be 90%. The adsorbed CO

can be removed in the more positive potential region where OH adsorption proceeds on the Pt surface. An

irreversible oxidation current corresponding to a CO oxidation reaction started to flow at 0.45 V. In the

second cycle, a reversible current, corresponding to hydrogen adsorption/desorption on Pt and a

quasi-reversible current corresponding to OH adsorption/desorption on Pt were observed around 0 V and

0.6 V, respectively. After the oxidative removal of CO from the Pt surface, a typical CV of poly Pt was

obtained. The poly Pt surface was completely poisoned by CO with CO bubbling for more than 60 s.

Figure 3-20 shows the CO stripping voltammograms of 32-Pt-Ru/Au in a 0.1 M HClO$_4$ solution (first cycle: black, second cycle: gray). The potential was swept from 0.2 V to negative potential and then swept back to positive potential. 32-Pt-Ru/Au had s better tolerance against CO than poly Pt. The CO oxidation current began to flow at ca. 0.64 V. The CO coverage on the Pt in 32-Pt-Ru/Au after CO bubbling for 30 s
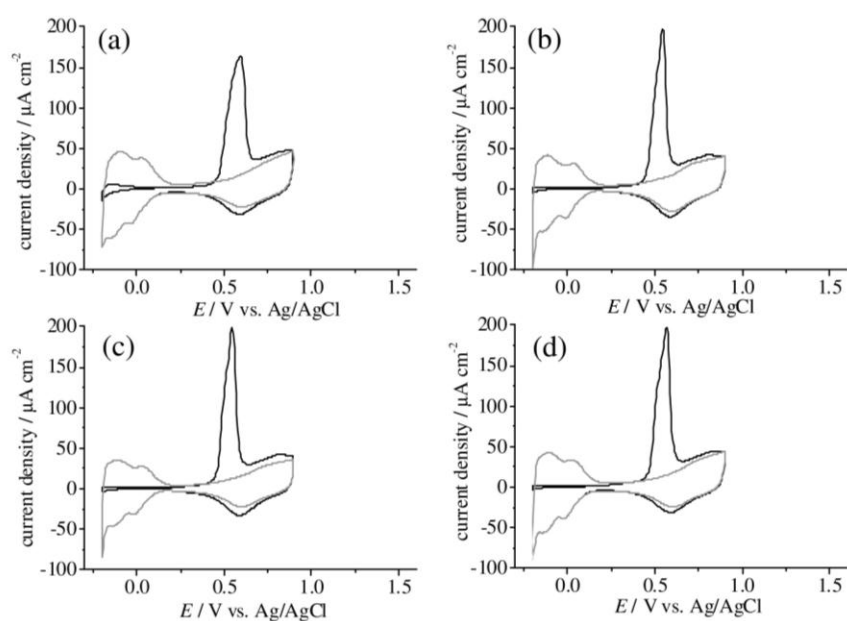

Figure 3-19. CO stripping voltammograms of poly Pt in 0.1 M HClO$_4$ solutions. Poison time: (a) 10 s, (b) 30 s, (c) 120 s and (d) 300 s. Scan rate = 50 mV s^{-1}.

Figure 3-20. CO stripping voltammograms of 32-Pt-Ru/Au in 0.1 M HClO$_4$ solutions. Poison time: (a) 10 s, (b) 30 s, (c) 120 s, (d) 300 s and (e) 600 s. Scan rate = 50 mV s^{-1}.

61

was estimated to be 60%. The Pt surface of 32-Pt-Ru/Au was completely covered with CO bubbling for more than 300 s.

Figure 3-21 shows the CO stripping voltammograms of Pt-Ru$_{mix}$/Au in a 0.1 M HClO$_4$ solution (first cycle: black, second cycle: gray). The potential was swept from 0.2 V to negative potential and then swept

Figure 3-21. CO stripping voltammograms of Pt-Ru$_{mix}$/Au in 0.1 M HClO$_4$ solutions. Poison time: (a) 10 s, (b) 30 s, (c) 120 s, (d) 300 s and (e) 600 s. Scan rate = 50 mV s^{-1}.
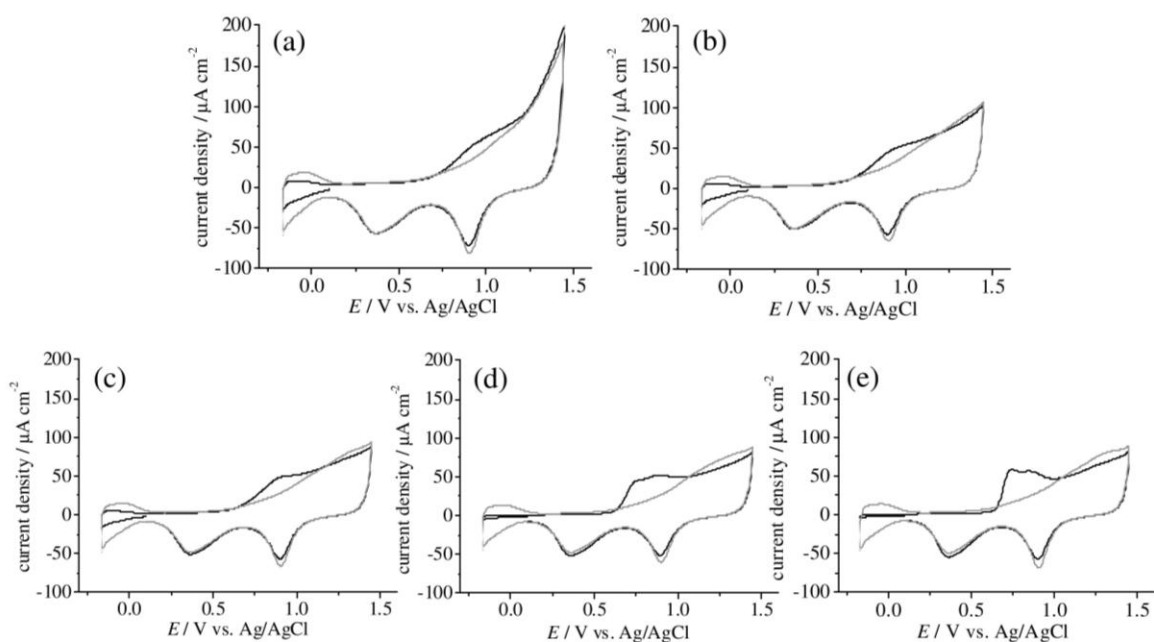

Figure 3-22. CO stripping voltammograms of 24-Pt/Au in 0.1 M HClO$_4$ solutions. Poison time: (a) 10 s, (b) 30 s, (c) 120 s, (d) 300 s and (e) 600 s. Scan rate = 50 mV s^{-1}.

62

back to positive potential. The CO oxidation current started to flow at ca. 0.38 V. Pt-Ru$_{mix}$/Au also had a better CO tolerance than poly Pt. The CO coverage on the Pt in Pt-Ru$_{mix}$/Au after CO bubbling for 30 s was estimated at 65%. The Pt surface of Pt-Ru$_{mix}$/Au was completely covered with CO by CO bubbling for more than 600 s.

Figure 3-22 shows the CO stripping voltammograms of 24-Pt/Au in a 0.1 M HClO$_4$ solution (first cycle: black, second cycle: gray). The potenti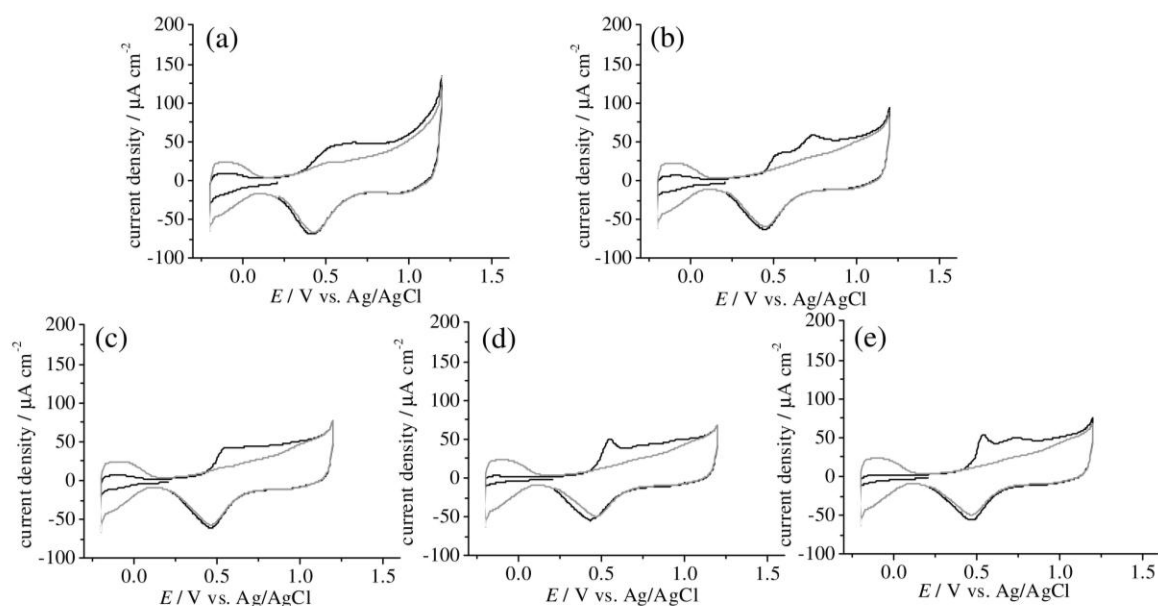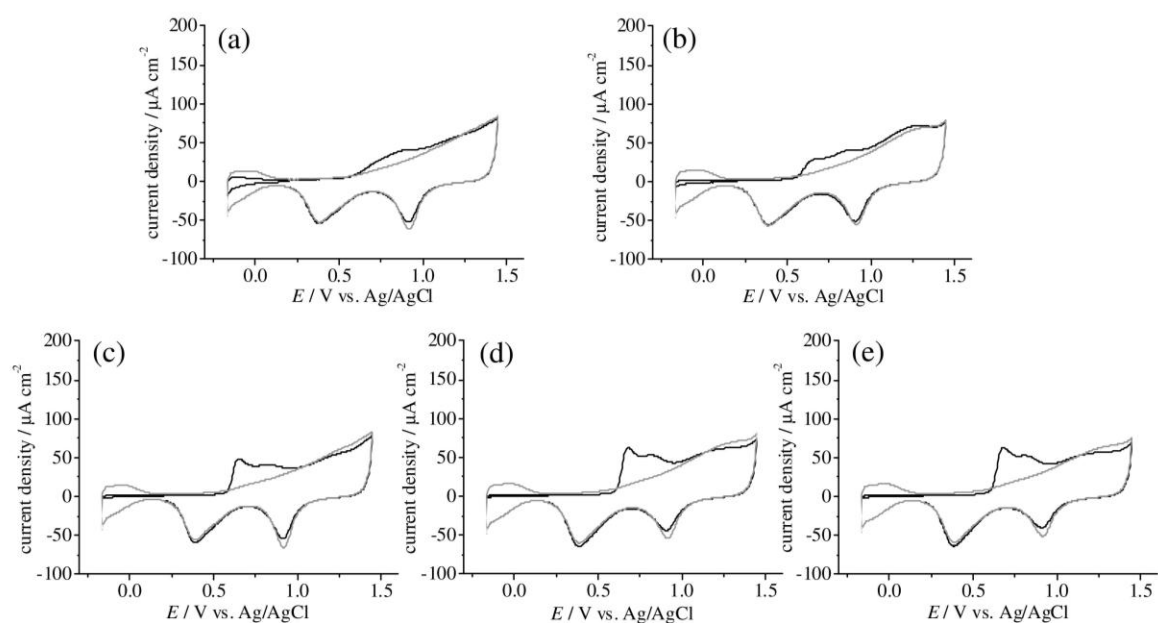al was swept from 0.2 V to negative potential and then swept to positive potential. The CO oxidation current started to flow at ca. 0.6 V. 24-Pt/Au had a better CO tolerance than poly Pt, and the CO coverage on Pt after CO poisoning for 30 s was estimated to be 80%. The Pt surface of the 24-Pt/Au was completely poisoned by CO with CO bubbling for more than 120 s.

Figure 3-23 shows the plots of CO coverage for poly Pt, 32-Pt-Ru/Au, Pt-Ru$_{mix}$/Au and 24-Pt/Au against CO poison time. 32-Pt-Ru/Au and Pt-Ru$_{mix}$/Au had higher tolerances against CO than poly Pt and 24-Pt/Au. However, 32-Pt-Ru/Au and Pt-Ru$_{mix}$/Au had poor tolerances against CO compared to the reported results of CO oxidation reaction on Pt-Ru alloys.[8, 65]

The peak potentials, peak current densities, charges of CO stripping (Q_{CO}), and ratios of hydrogen adsorption and CO oxidation reaction (Q_{CO}/Q_H) charge for poly Pt, 32-Pt-Ru/Au, Pt-Ru$_{mix}$/Au and 24-Pt/Au are summarized in Table 3-5. The peak potential of CO oxidation reaction for 32-Pt-Ru/Au was the most positive among the four measured electrodes, in spite of its high tolerance against CO and MOR activity. According to results reported by Strbac et al., the peak potentials of CO oxidation reaction at Pt on Au(111) depends on the size of Pt. The peak potential of a CO oxidation reaction on small Pt is small is more positive than on poly Pt. The peak potential shifted negatively as the size of Pt on Au(111) increased.[50] The adsorption of CO on RuO$_2$ in the Pt-Ru alloys can also affect the activity of CO oxidation reaction on Pt-Ru alloys. As shown in Table 3-5, the Q_{CO}/Q_H of 32-Pt-Ru/Au, Pt-Ru$_{mix}$/Au, and 24-Pt/Au is greater than that of poly Pt, suggesting that CO is adsorbed not only on Pt but also on Au and RuO$_2$.[66, 67] CO can adsorb on RuO$_2$, and the adsorbed CO on RuO$_2$ is oxidized at a more positive potential than the CO adsorbed on Ru metal.[67] RuO$_2$ in Pt-Ru alloys may be poisoned by CO and cannot act as a good promoter to remove CO
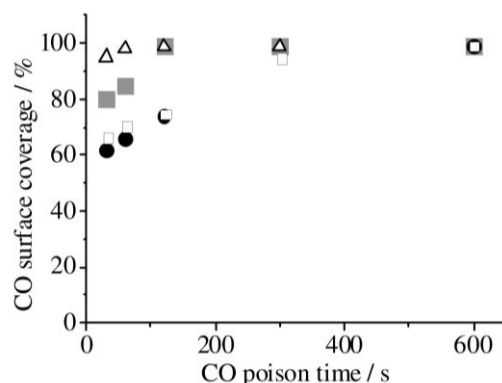
adsorbed on Pt.

Figure 3-23. The plots of CO coverage of poly Pt (white triangle), 32-Pt-Ru/Au (black circle), Pt-Ru$_{mix}$/Au (white square), and 24-Pt/Au (gray square) against poison time.

Table 3-5. Summary of peak potentials, peak current densities and charges of CO stripping of poly Pt, 32-Pt-Ru/Au, Pt-Ru$_{mix}$/Au, and 24-Pt/Au.

Sample	E_{peak} / V	I_{peak} / μA cm^{-2}	Q_{CO} / μC	Q_{CO} / Q_H
Poly Pt	+0.56	+197	+237.36	1.37
32-Pt-Ru/Au	+0.74	+59	+8.31	4.37
Pt-Ru$_{mix}$/Au	+0.53	+56	+9.20	2.73
24-Pt/Au	+0.68	+64	+14.19	3.37

3.2.4.3   HOR

Figures 3-24 (a), 3-25 (a), and 3-26 (a) show the CVs of poly Pt, 32-Pt-Ru/Au, and Pt-Ru$_{mix}$/Au, respectively, in Ar saturated 0.1 M HClO$_4$ solutions at a scan rate of 50 mV s^{-1} with and without rotation at 500 rpm. The reversible redox peaks corresponding to hydrogen adsorption/desorption, and quasi-reversible redox peaks, corresponding to OH adsorption/desorption were observed at 0 V and 0.6 V, respectively. It was confirmed that the solution was completely purged with Ar. After O$_2$ removal from the electrolyte solution was confirmed, the solution was saturated with H$_2$.

Figure 3-24 (b) shows LSVs of poly Pt in a 0.1 M HClO$_4$ solution saturated with H$_2$. The potential was swept from –0.26 V to 0.8 V at a scan rate of 10 mV s^{-1} and a rotation rate between 500 and 3000 rpm. The HOR current started to flow at ca. –0.26 V. It increased as the electrode potential became more positive, and the limiting current was observed. The current began to decrease at 0.5 V as a result of OH adsorption

64
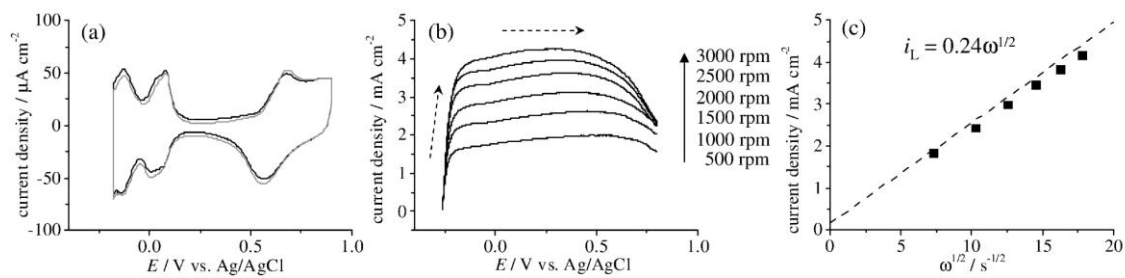
Figure 3-24. (a) CVs of poly Pt in H_2-free 0.1 M $HClO_4$ solutions with (gray) and without rotation (black) at 500 rpm. Scan rate = 50 mV s^{-1}. (b) LSVs of poly Pt in 0.1 M $HClO_4$ solutions saturated with H_2. Scan rate = 10 mV s^{-1}. (c) Levich plot at 0.1 V vs. Ag/AgCl.
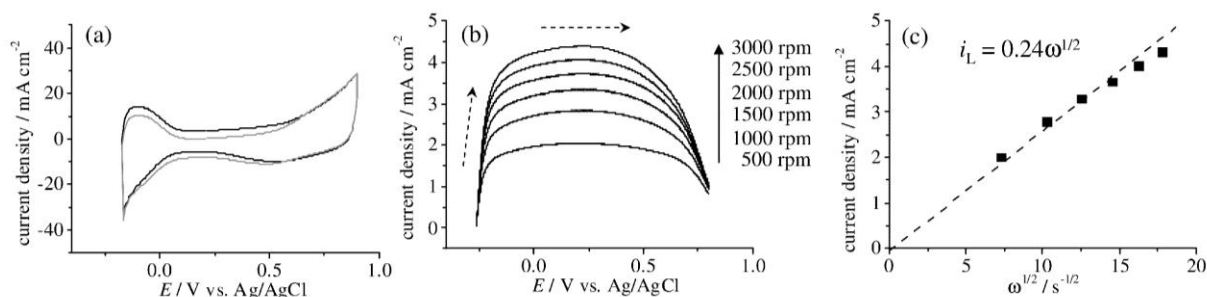
Figure 3-25. (a) CVs of 32-Pt-Ru/Au in H_2-free 0.1 M $HClO_4$ solutions with (gray) and without rotation (black) at 500 rpm. Scan rate = 50 mV s^{-1}. (b) LSVs of 32-Pt-Ru/Au in 0.1 M $HClO_4$ solutions saturated with H_2. Scan rate = 10 mV s^{-1}. (c) Levich plot at 0.1 V vs. Ag/AgCl.
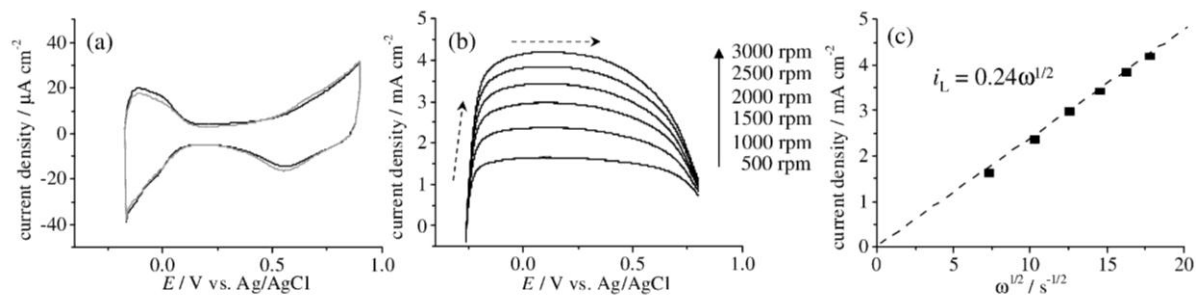
Figure 3-26. (a) CVs of Pt-Ru$_{mix}$/Au in H_2-free 0.1 M $HClO_4$ solutions with (gray) and without rotation (black) at 500 rpm. Scan rate = 50 mV s^{-1}. (b) LSVs of the Pt-Ru$_{mix}$/Au in 0.1 M $HClO_4$ solutions saturated with H_2. Scan rate = 10 mV s^{-1}. (c) Levich plot at 0.1 V vs. Ag/AgCl.

on the Pt surface. The relationship between the diffusion-limiting current density and rotation rate is given

by the Levich equation:

$$i_L = B\omega^{1/2} = 0.62nFC_R^*D_{2/3}v^{-1/6}\omega^{1/2} \quad (3\text{-}7)$$

where i_L is the diffusion-limiting current density, n is the number of electrons in the HOR ($n = 2$), F is the Faraday constant ($F = 96490$ C mol^{-1}), C_{H2}^* is the bulk hydrogen concentration, D is the diffusion coefficient of hydrogen molecules in a 0.1 M HClO$_4$ solution ($D = 3.6 \times 10^{-5}$ cm^2 s^{-1}),[68] and v is the kinematic viscosity of the electrolyte ($v = 0.01$ cm$_2$ s^{-1}).[69] From the Levich plot (i_L versus $\omega^{1/2}$)

Figure 3-27. LSVs of poly Pt (green, A), 32-Pt-Ru/Au (blue, B), and Pt-Ru$_{mix}$/Au (red, C) in 0.1 M HClO$_4$ solutions saturated with H$_2$. Scan rate = 10 mV s^{-1}. Rotation rate = 2500 rpm.

for the limiting current at 0.1 V shown in Figure 3-24 (c), the bulk hydrogen concentration was estimated to be 8.4×10^{-4} M, and this value was quite close to the value that other authors determined in another electrolyte.[70] Figures 3-25 (b) and 3-26 (b) show the LSVs of 32-Pt-Ru/Au and Pt-Ru$_{mix}$/Au in 0.1 M HClO$_4$ solutions saturated with H$_2$, respectively. The potential was swept from –0.26 V to 0.8 V at a scan rate of 10 mV s^{-1} and a rotation rate between 500 and 3000 rpm. The limiting current started to decrease at a potential more negative than that of poly Pt, suggesting that OH adsorption on Pt-Ru alloys begins at a more negative potential than Pt.

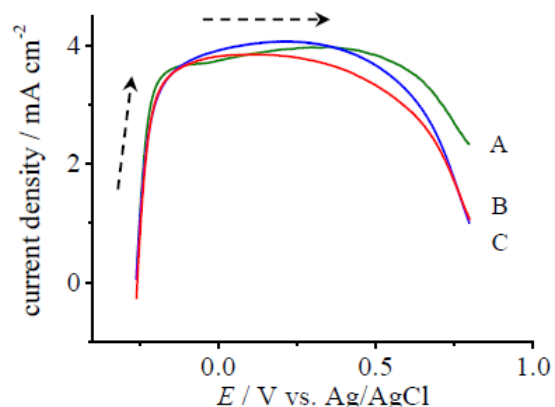Figure 3-27 shows the LSVs of poly Pt (green, A), 32-Pt-Ru/Au (blue, B), and Pt-Ru$_{mix}$/Au (red, C) in 0.1 M HClO$_4$ solutions saturated with H$_2$ at scan rates of 10 mV s^{-1} and rotation rates of 2500 rpm. The current densities for HOR of poly Pt, 32-Pt-Ru/Au and Pt-Ru$_{mix}$/Au at 0.4, 0.5, 0.6 and 0.7 V were obtained

Table 3-6. Summary of HOR current densities of poly Pt, 32-Pt-Ru/Au, and Pt-Ru$_{mix}$/Au at various potentials.

Sample	poly Pt	32-Pt-Ru/Au	Pt-Ru$_{mix}$/Au
E / V	i / mA cm^{-2}	i / mA cm^{-2}	i / mA cm^{-2}
0.4	3.97	3.89	3.56
0.5	3.83	3.65	3.32
0.6	3.58	3.22	2.94
0.7	2.27	2.47	3.13

from the results in Figure 3-27 and summarized in Table 3-6. The limiting current of Pt-Ru$_{mix}$/Au decreased at a potential more negative than poly Pt or 32-Pt-Ru/Au. Pt in Pt-Ru$_{mix}$/Au probably has a higher adsorption ability for OH than Pt in 32-Pt-Ru/Au.

The effect of CO on HOR activity on various electrodes was also investigated. Figure 3-28 shows the LSVs of (a) poly Pt, (b) 32-Pt-Ru/Au, and (c) Pt-Ru$_{mix}$/Au in 0.1 M HClO$_4$ solutions saturated with H$_2$ containing 0.2% CO. The potential was swept from –0.2 V to 0.8 V. Compared to the LSVs in 0.1 M HClO$_4$ solutions without CO, oxidation current started to flow at a more positive potential because of CO poisoning on the Pt surface. After the removal of CO from the Pt surface, a large oxidation current corresponding to the HOR and CO oxidation reaction started to flow at 0.5 V. 32-Pt-Ru/Au and Pt-Ru$_{mix}$/Au did not have high HOR activities under a H$_2$ atmosphere with CO compared to Pt-based alloys reported by other authors.[8]
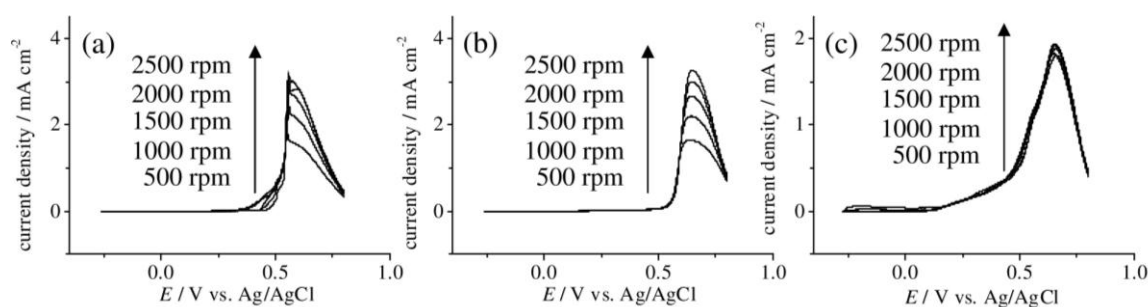
Figure 3-28. LSVs of (a) poly Pt, (b) 32-Pt-Ru/Au, and (c) Pt-Ru$_{mix}$/Au in 0.1 M HClO$_4$ solutions saturated with H$_2$ containing 0.2% CO. Scan rate = 10 mV s^{-1}.

Figure 3-29 shows the LSVs of poly Pt (green, A), 32-Pt-Ru/Au (blue, B), and Pt-Ru$_{mix}$/Au (red, C) in 0.1 M HClO$_4$ solutions saturated with H$_2$ containing 0.2% CO at a scan rate of 10 mV s^{-1} and a rotation rate of 2500 rpm. On Pt-Ru$_{mix}$/Au, the oxidation current corresponding to HOR started to flow at the most negative potential. The onset potential for HOR (current density = 0.3 mA cm^{-2}) in poly Pt, 32-Pt-Ru/Au, and Pt-Ru$_{mix}$/Au was 0.49, 0.56, and 0.40 V, respectively. The order of HOR activity under H$_2$ atmosphere containing CO was the same as the peak potential of CO stripping. Because of the low amount of CO contained in the gas, 32-Pt-Ru/Au showed poor HOR activity.
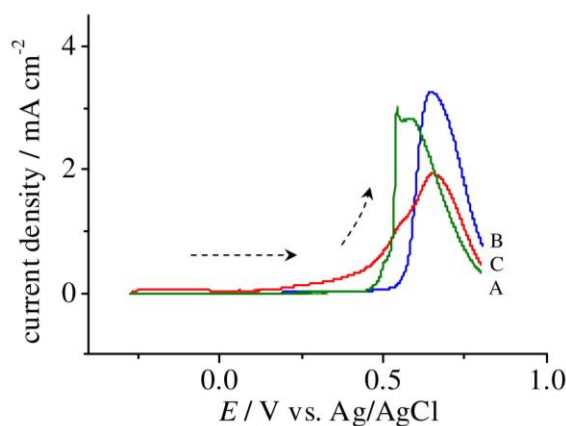
Figure 3-29. LSVs of poly Pt (green, A), 32-Pt-Ru/Au (blue, B), and Pt-Ru$_{mix}$/Au (red, C) in 0.1 M HClO$_4$ solutions saturated with H$_2$ containing 0.2% CO. Scan rate = 10 mV s^{-1}. Rotation rate = 2500 rpm.

3.2.4.4 ORR

Figure 3-30 (a) shows the LSVs of poly Pt in 0.1 M HClO$_4$ solutions saturated with O$_2$ at a scan rate of 10 mV s^{-1} and a rotation rate between 500 and 3000 rpm. The potential was swept from 0.8 V to –0.2 V. The reduction current corresponding to ORR started to flow at 0.7 V. In the more positive potential region, ORR was inhibited by adsorbed OH on Pt.[71, 72] The ORR increased as the electrode potential became more negative, and the limiting current was observed. It started to decrease around 0 V because the two electron ORR process becomes dominant in the hydrogen adsorption region.[72, 73] The bulk concentration and diffusion coefficients of oxygen molecules in the 0.1 M HClO$_4$ solution are 1.9×10^{-5} M and 1.2×10^{-6} cm^2 s^{-1}, respectively.[51] The number of electrons transferred in the overall reaction process was estimated to be 3.90 at 0.3 V by Levich plot (Figure 3-30 (b)).

Figure 3-31 shows the LSVs of 32-Pt-Ru/Au in 0.1 M HClO$_4$ solutions saturated with O$_2$ at a scan rate of 10 mV s^{-1} and a rotation rate between 500 and 2500 rpm. The potential was swept from 0.8 V to –0.2 V. The reduction current corresponding to ORR started to flow around 0.65 V. The number of electrons transferred in the overall reaction process was estimated to be 3.90 at 0.1 V according to the Levich plot (Figure 3-31 (b)).

Figure 3-32 (a) shows the LSVs of Pt-Ru$_{mix}$/Au in a 0.1 M HClO$_4$ solution saturated with O$_2$ at a scan rate of 10 mV s^{-1} and a rotation rate between 500 and 3000 rpm. The potential was swept from 0.8 V to

68
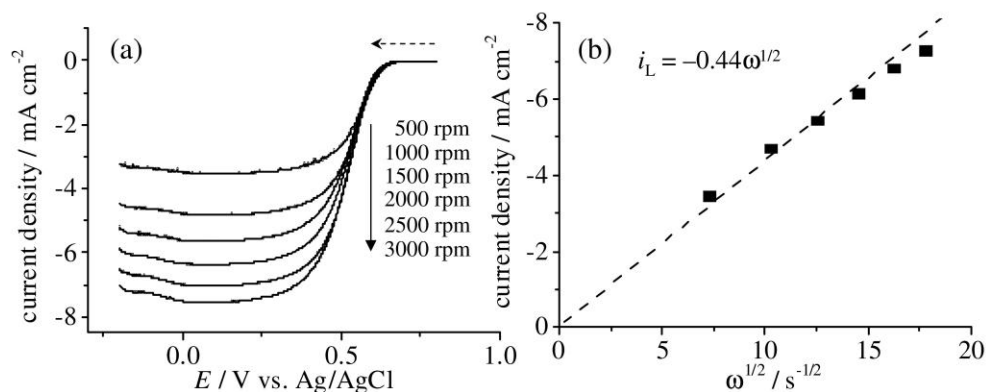
Figure 3-30. (a) LSVs of poly Pt in 0.1 M HClO$_4$ solutions saturated with O$_2$. Scan rate = 10 mV s^{-1}. (b) Levich plot at 0.3 V vs. Ag/AgCl.
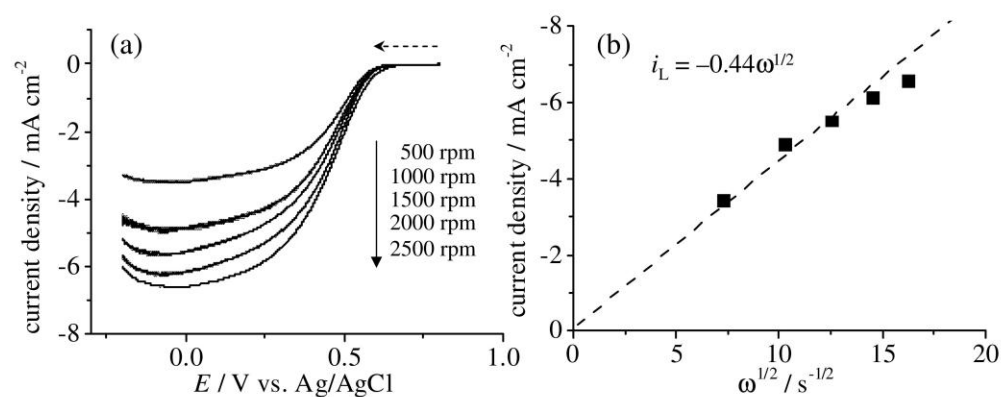
Figure 3-31. (a) LSVs of 32-Pt-Ru/Au in 0.1 M HClO$_4$ solutions saturated with O$_2$. Scan rate = 10 mV s^{-1}. (b) Levich plot at 0.1 V vs. Ag/AgCl.

Figure 3-32. (a) LSVs of Pt-Ru$_{mix}$/Au in 0.1 M HClO$_4$ solutions saturated with O$_2$. Scan rate = 10 mV s^{-1}. (b) Levich plot at 0.1 V vs. Ag/AgCl.

−0.2 V. The reduction current corresponding to ORR started to flow around 0.62 V. The number of electrons transferred in the overall reaction process was estimated to be 3.11 by Levich plot at 0.1 V (Figure 3-32 (b)).

69

Figure 3-33 shows the LSVs of bare Au(111) in 0.1 M HClO$_4$ solutions saturated with O$_2$ at a scan rate of 10 mV s^{-1} and a rotation rate bet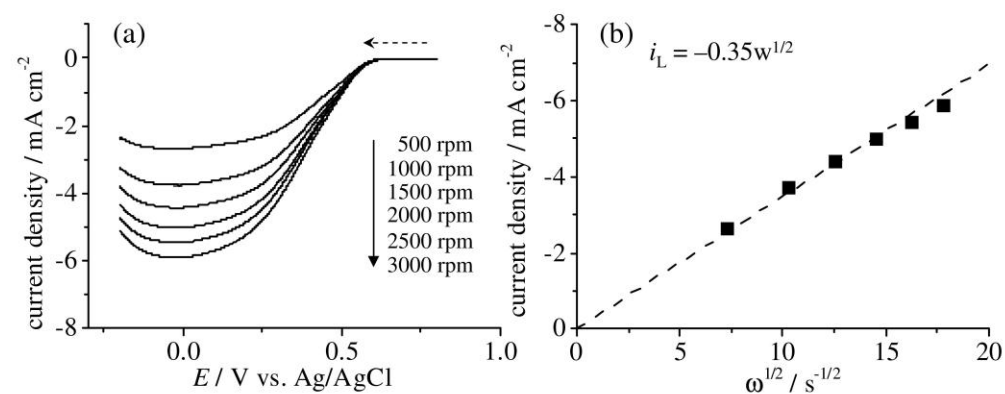ween 500 and 2500 rpm. The potential was swept from 0.8 V to –0.2 V. A cathodic current was first observed around 0.25 V and increased as the electrode potential became negative, but limiting currents were not observed in the solution because of hydrogen evolution reaction. This result agrees with the previous reports that Au shows poor ORR activity in acid solutions.[48]

Figure 3-34 shows the LSVs of poly Pt (green, A), 32-Pt-Ru/Au (blue, B), Pt-Ru$_{mix}$/Au (red, C), and bare Au(111) (black, D) in 0.1 M HClO$_4$ solutions saturated with O$_2$ at a scan rate of 10 mV s^{-1} and a rotation rate of 2500 rpm. Although the ORR activity of Au(111) was significantly improved with Pt-Ru alloy modification, the ORR activity of 32-Pt-Ru/Au and Pt-Ru$_{mix}$/Au was less than that of poly Pt. Another author reported that Pt-Ru alloys[74] and Pt on Au(111)[55] have less ORR activity than Pt.
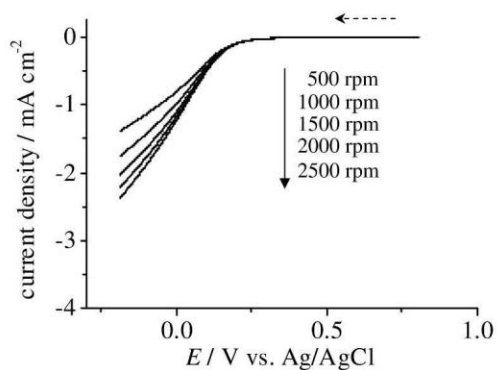
Figure 3-33 LSVs of bare Au(111) in 0.1 M HClO$_4$ solutions saturated with O$_2$. Scan rate = 10 mV s^{-1}.
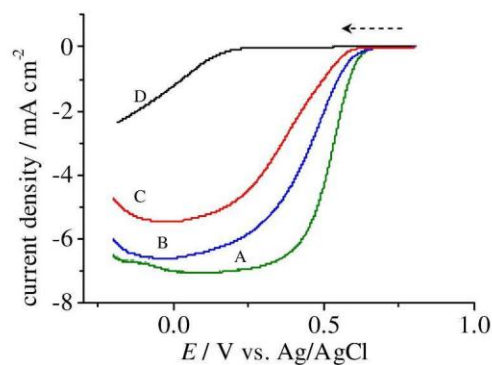
Figure 3-34 LSVs of poly Pt (green, A), 32-Pt-Ru/Au (blue, B), Pt-Ru$_{mix}$/Au (red, C), and the bare Au(111) (black, D) in 0.1 M HClO$_4$ solutions saturated with O$_2$. Scan rate = 10 mV s^{-1}. Rotation rate = 2500 rpm.

The kinetic current and rate constants for ORR were analyzed using the following Koutecky-Levich (K-L) equation:

$$1/i = 1/i_k + 1/B\omega^{1/2} \quad (3\text{-}8)$$

where i_k is the current in the absence of any mass transfer, and is given by as follows:

$$i_k = nFAkC_{O2}. \qquad (3\text{-}9)$$

A plot of $1/i$ versus $1/\omega^{1/2}$ should be liner and can be extrapolated to $1/\omega^{1/2} = 0$ to yield $1/i_k$. Then, the rate constant can be obtained from eq. 3-9. Figure 3-35 shows K-L plots of (a) poly Pt, (b) 32-Pt-Ru/Au, and (c) Pt-Ru$_{mix}$/Au using data from Figures 3-30, 3-31, and 3-32, respectively. The kinetic current and rate constants determined at various potentials are summarized in Table 3-7. At 0.4 V, poly Pt had rate constants 5.1 and 8.3 times larger than 32-Pt-Ru/Au and Pt-Ru$_{mix}$/Au, respectively. 32-Pt-Ru/Au had a larger rate constant for ORR than Pt-Ru$_{mix}$/Au.

The difference in HOR and ORR activity between 32-Pt-Ru/Au and Pt-Ru$_{mix}$/Au shows the difference of OH adsorption ability in Pt. Pt in 32-Pt-Ru/Au has less adsorption ability for OH than Pt in Pt-Ru$_{mix}$/Au. The difference in the adsorption ability of OH on Pt probably affects MOR activity and CO tolerance.
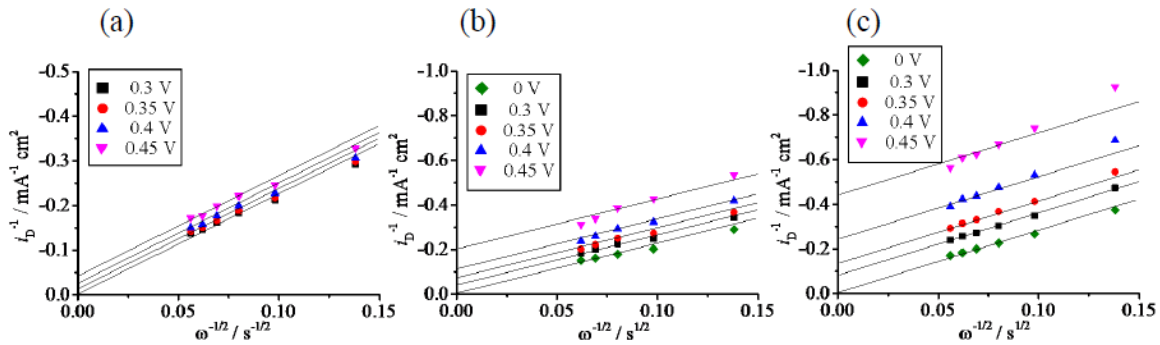
Figure 3-35 Koutecky-Levich plots of (a) poly Pt, (b) 32-Pt-Ru/Au, and (c) Pt-Ru$_{mix}$/Au at various potentials.

Table 3-7. The kinetic currents (i_k) and rate constants (k) of poly Pt, 32-Pt-Ru/Au, and Pt-Ru$_{mix}$/Au at various potentials.

Sample	poly Pt		32-Pt-Ru/Au		Pt-Ru$_{mix}$/Au	
E / V	i_k / mA cm^{-2}	k / cm s^{-1}	i_k / mA cm^{-2}	k / cm s^{-1}	i_k / mA cm^{-2}	k / cm s^{-1}
0.3			−18.52	0.040	−12.98	0.035
0.35	−142.86	0.311	−12.05	0.025	−7.09	0.019
0.4	−41.67	0.091	−8.33	0.018	−4.00	0.011
0.45	−23.81	0.052	−4.50	0.011	−2.26	0.006

3.3   Conclusion

Pt-Ru alloys with various coverage were prepared by repeating the cycle of Pt-Ru complex adsorption and heat treatment on Au(111). The Pt-Ru alloys with monoatomic height had unique electrochemical properties that were different from the Pt-Ru alloy with a few atomic heights. The MOR activity of Pt-Ru alloy in acidic solution showed no correlation with the surface coverage of Pt-Ru alloy. On the other hand, the MOR activity of Pt-Ru alloy in alkaline solution showed correlation with the surface coverage of Pt-Ru alloy. The peak current density of MOR of Pt-Ru alloy was much higher in alkaline solution than in acidic solution. The enhancement of MOR activity in alkaline solution may be caused by the Au substrate. The Pt-Ru alloy with high coverage on Au(111) had higher MOR activity and durability in acidic solution than poly Pt, Au(111) modified with Pt and Pt-Ru alloy prepared from a mixture of K_2PtCl_4 and $RuCl_3$. The Pt-Ru alloy prepared from Pt-Ru complex showed poor activity against the CO oxidation reaction, HOR under H_2 atmosphere containing CO, and ORR.

Reference

1.   H. A. Gasteiger, N. M. Markovic and P. N. Ross, *J. Phys. Chem.*, 1995, **99**, 8290-8301.

2.   H. A. Gasteiger, N. M. Markovic and P. N. Ross, *J. Phys. Chem.*, 1995, **99**, 16757-16767.

3.   T. Takeguchi, T. Yamanaka, K. Asakura, E. N. Muhamad, K. Uosaki and W. Ueda, *J. Am. Chem. Soc.*, 2012, **134**, 14508-14512.

4.   K. Sasaki, Y. Mo, J. X. Wang, M. Balasubramanian, F. Uribe, J. McBreen and R. R. Adzic, *Electrochim. Acta*, 2003, **48**, 3841-3849.

5.   Y. J. Ando, K. Sasaki and R. Adzic, *Electrochem. Commun.*, 2009, **11**, 1135-1138.

6.   K. Sasaki and R. R. Adzic, *J. Electrochem. Soc.*, 2008, **155**, B180-B186.

7.   A. E. Russell and A. Rose, *Chem. Rev.*, 2004, **104**, 4613-4635.

8.   H. Igarashi, T. Fujino, Y. M. Zhu, H. Uchida and M. Watanabe, *Phys. Chem. Chem. Phys.*, 2001, **3**, 306-314.

9.   M. Watanabe, Y. M. Zhu and H. Uchida, *J. Phys. Chem. B*, 2000, **104**, 1762-1768.

10.   M. Wakisaka, S. Mitsui, Y. Hirose, K. Kawashima, H. Uchida and M. Watanabe, *J. Phys. Chem. B*, 2006, **110**, 23489-23496.

11.   X. H. Xia, T. Iwasita, F. Ge and W. Vielstich, *Electrochim. Acta*, 1996, **41**, 711-718.

12.   S. Hadzijordanov, H. Angersteinkozlowska, M. Vukovic and B. E. Conway, *J. Electrochem. Soc.*, 1978, **125**, 1471-1480.

13.   J. X. Wang, N. S. Marinkovic, H. Zajonz, B. M. Ocko and R. R. Adzic, *J. Phys. Chem. B*, 2001, **105**, 2809-2814.

14.   M. Watanabe and S. Motoo, *J. Electroanal. Chem.*, 1975, **60**, 267-273.

15.   M. Watanabe and S. Motoo, *J. Electroanal. Chem.*, 1975, **60**, 275-283.

16.   E. Ticanelli, J. G. Beery, M. T. Paffett and S. Gottesfeld, *J. Electroanal. Chem.*, 1989, **258**, 61-77.

17.   T. Yajima, H. Uchida and M. Watanabe, *J. Phys. Chem. B*, 2004, **108**, 2654-2659.

18.   D. R. Rolison, P. L. Hagans, K. E. Swider and J. W. Long, *Langmuir*, 1999, **15**, 774-779.

19. L. Cao, F. Scheiba, C. Roth, F. Schweiger, C. Cremers, U. Stimming, H. Fuess, L. Q. Chen, W. T. Zhu and X. P. Qiu, *Angew. Chem. Int. Ed.*, 2006, **45**, 5315-5319.

20. F. Maroun, F. Ozanam, O. M. Magnussen and R. J. Behm, *Science*, 2001, **293**, 1811-1814.

21. K. Kusada, M. Yamauchi, H. Kobayashi, H. Kitagawa and Y. Kubota, *J. Am. Chem. Soc.*, 2010, **132**, 15896-15898.

22. A. Crown, C. Johnston and A. Wieckowski, *Surf. Sci.*, 2002, **506**, L268-L274.

23. C. Roth, N. Martz, A. Morlang, R. Theissmann and H. Fuess, *Phys. Chem. Chem. Phys.*, 2004, **6**, 3557-3562.

24. R. Chetty, W. Xia, S. Kundu, M. Bron, T. Reinecke, W. Schuhmann and M. Muhler, *Langmuir*, 2009, **25**, 3853-3860.

25. L. S. Sarma, C. H. Chen, S. M. S. Kumar, G. R. Wang, S. C. Yen, D. G. Liu, H. S. Sheu, K. L. Yu, M. T. Tang, J. F. Lee, C. Bock, K. H. Chen and B. J. Hwang, *Langmuir*, 2007, **23**, 5802-5809.

26. H. Nitani, T. Nakagawa, H. Daimon, Y. Kurobe, T. Ono, Y. Honda, A. Koizumi, S. Seino and T. A. Yamamoto, *Appl. Catal. A: Gen.*, 2007, **326**, 194-201.

27. B. A. L. Demishima, H. T. Mishima and G. Castro, *Electrochim. Acta*, 1995, **40**, 2491-2500.

28. M. S. Nashner, D. M. Somerville, P. D. Lane, D. L. Adler, J. R. Shapley and R. G. Nuzzo, *J. Am. Chem. Soc.*, 1996, **118**, 12964-12974.

29. M. S. Nashner, A. I. Frenkel, D. L. Adler, J. R. Shapley and R. G. Nuzzo, *J. Am. Chem. Soc.*, 1997, **119**, 7760-7771.

30. M. S. Nashner, A. I. Frenkel, D. Somerville, C. W. Hills, J. R. Shapley and R. G. Nuzzo, *J. Am. Chem. Soc.*, 1998, **120**, 8093-8101.

31. C. W. Hills, M. S. Nashner, A. I. Frenkel, J. R. Shapley and R. G. Nuzzo, *Langmuir*, 1999, **15**, 690-700.

32. E. S. Steigerwalt, G. A. Deluga and C. M. Lukehart, *J. Phys. Chem. B*, 2002, **106**, 760-766.

33. E. S. Steigerwalt, G. A. Deluga, D. E. Cliffel and C. M. Lukehart, *J. Phys. Chem. B*, 2001, **105**,

8097-8101.

34.   T. C. Deivaraja and J. Y. Lee, *J. Electrochem. Soc.*, 2004, **151**, A1832-A1835.

35.   H. Uehara, Y. Okawa, Y. Sasaki and K. Uosaki, *Chem. Lett.*, 2009, **38**, 148-149.

36.   H. Uehara, Ph.D thesis, Hokkaido University, 2009.

37.   J. F. Moulder, W. F. Stickle, P. E. Sobol and K. D. Bomben, *Handbook of X-ray Photoelectron Spectroscopy*, Perkin-Elmer, Minnesota, 1992.

38.   F. M. Pan, P. C. Stair and T. H. Fleisch, *Surf. Sci.*, 1986, **177**, 1-13.

39.   C. Agnes, J. C. Arnault, F. Omnes, B. Jousselme, M. Billon, G. Bidan and P. Mailley, *Phys. Chem. Chem. Phys.*, 2009, **11**, 11647-11654.

40.   A. Foelske, O. Barbieri, M. Hahn and R. Kotz, *Electrochem. Solid-State Lett.*, 2006, **9**, A268-a272.

41.   C. D. Wagner, L. E. Davis, M. V. Zeller, J. A. Taylor, R. H. Raymond and L. H. Gale, *Surf. Interface Anal.*, 1981, **3**, 211-225.

42.   B. E. Conway, *Prog. Surf. Sci.*, 1995, **49**, 331-452.

43.   M. AvramovIvic, V. Jovanovic, G. Vlajnic and J. Popic, *J. Electroanal. Chem.*, 1997, **423**, 119-124.

44.   P. Rodriguez, Y. Kwon and M. T. M. Koper, *Nature Chem.*, 2012, **4**, 177-182.

45.   M. Takahasi, Y. Hayashi, J. Mizuki, K. Tamura, T. Kondo, H. Naohara and K. Uosaki, *Surf. Sci.*, 2000, **461**, 213-218.

46.   T. Awatani, I. Yagi, H. Noguchi and K. Uosaki, *J. Electroanal. Chem.*, 2002, **524**, 184-193.

47.   H. Naohara, S. Ye and K. Uosaki, *J. Electroanal. Chem.*, 2001, **500**, 435-445.

48.   H. Naohara, S. Ye and K. Uosaki, *Electrochim. Acta*, 2000, **45**, 3305-3309.

49.   S. Strbac, F. Maroun, O. M. Magnussen and R. J. Behm, *J. Electroanal. Chem.*, 2001, **500**, 479-490.

50.   S. Strbac, S. Petrovic, R. Vasilic, J. Kovac, A. Zalar and Z. Rakocevic, *Electrochim. Acta*, 2007, **53**, 998-1005.

51.   R. R. Adzic, J. Wang and B. M. Ocko, *Electrochim. Acta*, 1995, **40**, 83-89.

52.   M. Baldauf and D. M. Kolb, *J. Phys. Chem.*, 1996, **100**, 11375-11381.

53.   A. A. El-Shafei, *J. Electroanal. Chem.*, 1998, **447**, 81-89.

54.   T. J. Schmidt, V. Stamenkovic, M. Arenz, N. M. Markovic and P. N. Ross, *Electrochim. Acta*, 2002, **47**, 3765-3776.

55.   J. L. Zhang, M. B. Vukmirovic, Y. Xu, M. Mavrikakis and R. R. Adzic, *Angew. Chem. Int. Ed.*, 2005, **44**, 2132-2135.

56.   T. Ghosh, M. B. Vukmirovic, F. J. DiSalvo and R. R. Adzic, *J. Am. Chem. Soc.*, 2010, **132**, 906-+.

57.   S. Park, Y. Xie and M. J. Weaver, *Langmuir*, 2002, **18**, 5792-5798.

58.   N. V. Smith, G. K. Wertheim, S. Hufner and M. M. Traum, *Phys. Rev. B*, 1974, **10**, 3197-3206.

59.   J. Riga, C. Tenretnoel, J. J. Pireaux, R. Caudano, J. J. Verbist and Y. Gobillon, *Phys. Scr.*, 1977, **16**, 351-354.

60.   T. L. Barr, *J. Phys. Chem.*, 1978, **82**, 1801-1810.

61.   R. Kotz, H. J. Lewerenz and S. Stucki, *J. Electrochem. Soc.*, 1983, **130**, 825-829.

62.   T. Arikawa, Y. Murakami and Y. Takasu, *J. Appl. Electrochem.*, 1998, **28**, 511-516.

63.   E. Tsuji, A. Imanishi, K. Fukui and Y. Nakato, *Electrochim. Acta*, 2011, **56**, 2009-2016.

64.   J. L. Cohen, D. J. Volpe and H. D. Abruna, *Phys. Chem. Chem. Phys.*, 2007, **9**, 49-77.

65.   E. Yoo, T. Okata, T. Akita, M. Kohyama, J. Nakamura and I. Honma, *Nano Lett.*, 2009, **9**, 2255-2259.

66.   B. B. Blizanac, M. Arenz, P. N. Ross and N. M. Markovic, *J. Am. Chem. Soc.*, 2004, **126**, 10130-10141.

67.   W. B. Wang, M. S. Zei and G. Ertl, *Chem. Phys. Lett.*, 2002, **355**, 301-305.

68.   H. Igarashi, T. Fujino and M. Watanabe, *J. Electroanal. Chem.*, 1995, **391**, 119-123.

69.   M. Harada, H. Noguchi, N. Zanetakis, S. Takakusagi, W. B. Song and K. Uosaki, *Sci. Technol. Adv. Mater.*, 2011, **12**.

70.   R. M. Q. Mello and E. A. Ticianelli, *Electrochim. Acta*, 1997, **42**, 1031-1039.

71.   N. M. Markovic, H. A. Gasteiger and N. Philip, *J. Phys. Chem.*, 1996, **100**, 6715-6721.

72.   N. M. Markovic, H. A. Gasteiger and P. N. Ross, *J. Phys. Chem.*, 1995, **99**, 3411-3415.

73.   N. M. Markovic, R. R. Adzic, B. D. Cahan and E. B. Yeager, *J. Electroanal. Chem.*, 1994, **377**, 249-259.

74.   M. Montiel, P. Hernandez-Fernandez, J. L. G. Fierro, S. Rojas and P. Ocon, *J. Power Sources*, 2009, **191**, 280-288.

Chapter 4

ORIGIN OF ENHANCEMENT OF ELECTROCATALYTIC ACTIVITY AND DURABILITY OF PT-RU ALLOY PREPARED FROM HETERO BI-NUCLEAR PT-RU COMPLEX FOR METHANOL OXIDATION REACTION

4.1   Introduction

The size, shape, thickness and local structure of electrocatalysts strongly affect their catalytic activity.[1-7] Therefore, it is very important to prepare structural controlled electrocatalysts. The increase of specific surface area of metal electrocatalysts leads to the increase of current and electromotive force of fuel cell systems. The shape of metal electrocatalysts is important because electrocatalytic activities of metals depend on their surface crystal structures. Thin metal films on foreign metals which are easily prepared by electrodeposition and galvanic displacement often show high electrocatalytic activities.[5, 6, 8-14] Uosaki et al. reported that Au single crystal electrodes modified with submonolayer Pd show high activity for formaldehyde oxidation[5] and oxygen reduction reactions.[6] Adzic et al. prepared Pd and Pt monolayer on foreign metals and revealed that their electronic structures are affected by foreign metals and the difference affects their ORR activities.[8-10] The size, shape and thickness of electrocatalysts can be controlled by parameters such as concentration, reaction time and temperature. However, it is very difficult to control the local structure of electrocatalysts by the electrochemical technique. Although Behm et al. reported that randomly mixed and ratio controlled Au-Pd alloys can be prepared by co-deposition of Au and Pd salts,[15] this method is not usable to prepare various alloys.

The structure of electrocatalysts can be changed by preparing from various starting materials.[16, 17] In chapter 3, Pt-Ru alloy prepared from Pt-Ru complex showed higher MOR activity and durability than not only Pt but also Pt-Ru alloy prepared from the mixture of K_2PtCl_4 and $RuCl_3$. The difference of activity against oxygen evolution reaction suggests the structure of RuO_2 in the Pt-Ru alloys prepared from Pt-Ru complex are different from those prepared from the mixture of K_2PtCl_4 and $RuCl_3$. It is considered that the difference in structure of RuO_2 affects MOR activity of Pt-Ru alloys.

In this chapter, the difference in structure of RuO_2 in Pt-Ru alloys prepared from Pt-Ru complex and the mixture of K_2PtCl_4 and $RuCl_3$ was investigated by XPS and Ru K edge XAFS measurements. Based on the results of the measurements, the origin of enhancement of activity and durability of the Pt-Ru alloy prepared from Pt-Ru complex for MOR was revealed.

4.2   Results and Discussions

4.2.1   STM

Figure 4-1 shows STM images of (a) 32-Pt-Ru/Au and (b) Pt-Ru$_{mix}$/Au in 0.1 M HClO$_4$ solutions at 0.2 V (vs. Ag/AgCl) after oxidation/reduction cycle (ORC) was carried out between –0.2 and 1.45 V five times at 50 mV s^{-1}. At both surfaces, many islands with a height of 0.3-1 nm, corresponding to a few atomic height were observed. From these results, it was confirmed the formation of thin film.
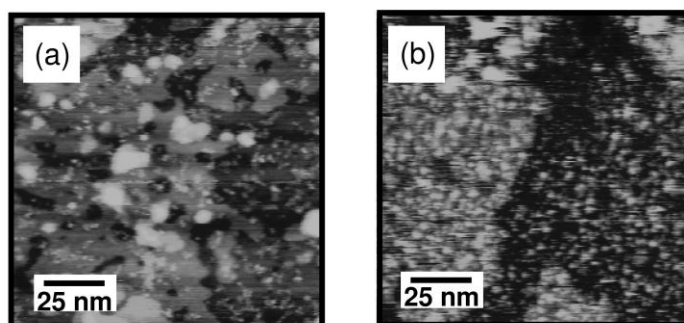

Figure 4-1. STM images of (a) 32-Pt-Ru/Au and (b) Pt-Ru$_{mix}$/Au in 0.1 M HClO$_4$ solutions at 0.2 V vs. Ag/AgCl ($E_{bias} = 0.16$ V, $I_{tc} = 0.6$ nA).

4.2.2   XPS

Figure 4-2 shows XP spectra in the Pt 4f, Ru 3p$_{3/2}$, O 1s, N 1s and S 2p regions of 32-Pt-Ru/Au (a) before and (b) after ORC between –0.2 and 1.45 V five times at 50 mV s^{-1}. The peak positions of Pt 4f$_{7/2}$, Ru 3p$_{3/2}$ and O 1s, full width at half maximums (FWHM) and ratios of peak area of 32-Pt-Ru/Au (a) before and (b) after ORC were summarized in Table 4-1. The peaks due to Pt 4f$_{7/2}$ and Pt 4f$_{5/2}$ are composed of two doublets, overlapped with the peak due to Au 5p$_{1/2}$ (74.2 eV). The most intensive ones are metallic Pt (Pt 4f$_{7/2}$: 70.5 eV, Pt 4f$_{5/2}$: 73.8 eV). The second-most intensive ones are Pt(II) oxides such as PtO and Pt(OH)$_2$ (Pt 4f$_{7/2}$: 72.1 eV, Pt 4f$_{5/2}$: 75.4 eV).[18] The peak due to Ru 3p$_{3/2}$ is composed of two doublets (462.4
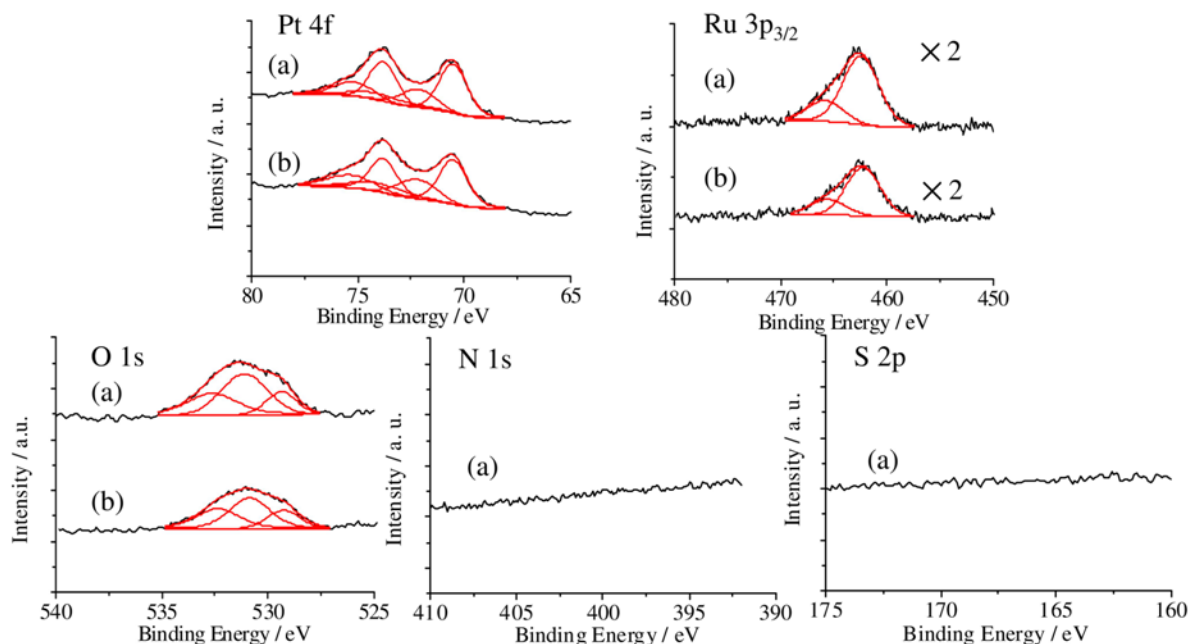
Figure 4-2. XP spectra in the Pt 4f, Ru 3p$_{3/2}$, O 1s, N 1s, and S 2p regions of 32-Pt-Ru/Au (a) before and (b) after ORC.

Table 4-1. The peak positions of Pt 4f$_{7/2}$, Ru 3p$_{3/2}$, and O 1s, full width at half maximums (FWHM) and ratios of peak area of XP spectra shown in Figure 4-2.

Sample	Pt 4f$_{7/2}$			
	Oxidation state	BE / eV	atomic ratio (%)	FWHM / eV
(a) before ORC	Pt(0)	70.5	69	1.53
	Pt(II)	72.1	31	1.94
(b) after ORC	Pt(0)	70.5	65	1.55
	Pt(II)	72.2	35	2.15

Sample	Ru 3p$_{3/2}$			
	Oxidation state	BE / eV	atomic ratio (%)	FWHM / eV
(a) before ORC	Ru(IV)	462.4	77	3.95
		465.8	23	3.94
(b) after ORC	Ru(IV)	462.5	81	4.10
		465.9	19	3.10

Sample	O 1s			
	Species	BE / eV	atomic ratio (%)	FWHM / eV
(a) before ORC	O^{2-}	529.4	17	1.66
	OH$^-$	531.1	49	2.56
	H$_2$O	532.6	34	2.77
(b) after ORC	O^{2-}	529.4	20	1.81
	OH$^-$	530.9	46	2.23
	H$_2$O	532.5	34	2.42

eV and 465.8 eV) and the peak position of the most intensive one is 0.9 eV higher than that of bulk Ru (0)

and similar to that of RuO$_2$. The shoulder peak observed at 465.8 eV originates from hydrous RuO$_2$.[19] Some

researchers have assigned this peak to surface-stabilized RuO_6, however, bulk RuO_6 is only stable in the vapor phase in the temperature between 1200 and 1500 ℃.[19] According to the reports, the peak of O 1s spectrum which was observed at 531.1 eV can distinguish three oxygen species which correspond to H_2O (532.6 eV), OH^- (531.1 eV) and O^{2-} (529.4 eV).[20] The peak corresponding to H_2O is overlapped with organic contamination as discussed in section 3.2.1.1. It should be noted that the peaks originate from nitrogen and sulfur which is contained in Pt-Ru complex were not observed, suggesting the pyrolysis of Pt-Ru complex.

The peak areas of Ru $3p_{3/2}$ and O 1s were slightly decreased after ORC as shown in Figure 4-2 (b). RuO_2, which promotes OER, may dissolve into electrolyte partially during OER.[21] On the other hand, the shape and peak position of XP spectra in the Pt 4f, Ru $3p_{3/2}$ and O 1s regions were not greatly changed, suggesting the oxidized Pt and Ru are not reduced after ORC.

Figure 4-3 shows XP spectra in the Pt 4f, Ru $3p_{3/2}$, O 1s, and Cl 2p regions of Pt-Ru_{mix}/Au (a) before and (b) after performing ORC from –0.2 to 1.45 V five times at 50 mV s^{-1}. The peak positions of Pt $4f_{7/2}$, Ru $3p_{3/2}$ and O 1s, FWHMs and ratios of peak area of the Pt-Ru_{mix}/Au (a) before and (a) after ORC were summarized in Table 4-2. Before the electrochemical treatment, almost none of Pt was reduced. Three doublets of the Pt $4f_{7/2}$ spectrum are due to metallic Pt (70.9 eV), Pt(II) oxides such as PtO and/or $Pt(OH)_2$ (72.2 eV) and Pt(IV) oxides such as PtO_2 and/or $Pt(OH)_4$ (73.9 eV).[18] Pt(IV) oxide species are the most intensive ones. The peak due to Ru $3p_{3/2}$ spectra is composed of two doublets (462.7 eV and 465.8 eV) and the peak position of the most intensive one is 1.2 eV higher than that of bulk Ru (0) and same as that of RuO_2. The shoulder peak observed at 465.8 eV originates from hydrous RuO_2.[19] The peak of the O 1s spectrum which was observed at 531.1 eV is composed of three oxygen species, H_2O (532.3 eV), OH^- (531.2 eV) and O^{2-} (530.0 eV) and the most intensive one is O^{2-}. The peak corresponding to Cl 2p was not observed.

After the ORC, oxidized Pt, especially Pt(IV) oxide species were mostly reduced to metallic Pt as shown in Figure 4-3 (b). The peaks due to Pt $4f_{7/2}$ and Pt $4f_{5/2}$ are composed of two doublets. The most intensive ones are metallic Pt (Pt $4f_{7/2}$: 70.9 eV, Pt $4f_{5/2}$: 74.2 eV). The second ones are Pt(II) oxide such as
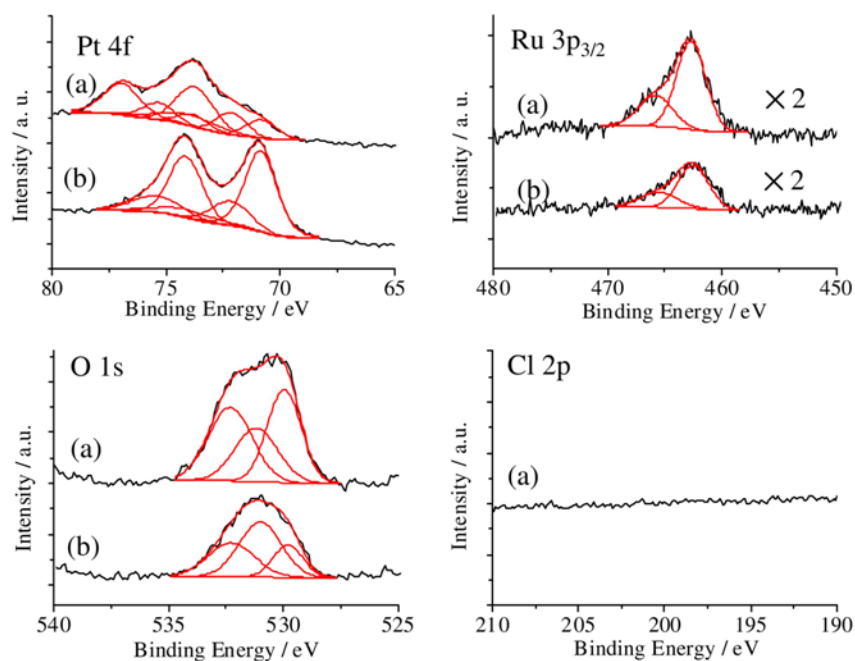
Figure 4-3. XP spectra in the Pt 4f, Ru 3p$_{3/2}$, O 1s, and Cl 2p regions of Pt-Ru$_{mix}$/Au (a) before and (b) after ORC.

Table 4-2. The peak positions of Pt 4f$_{7/2}$, Ru 3p$_{3/2}$, and O 1s, full width at half maximums (FWHM) and ratios of peak area of XP spectra shown in Figure 4-3.

| Sample | Pt 4f$_{7/2}$ | | | |
	Oxidation state	BE / eV	atomic ratio (%)	FWHM / eV
(a) before ORC	Pt(0)	70.9	20	1.53
	Pt(II)	72.2	24	1.53
	Pt(IV)	73.8	56	1.95
(b) after ORC	Pt(0)	70.9	75	1.63
	Pt(II)	72.2	25	2.02

| Sample | Ru 3p$_{3/2}$ | | | |
	Oxidation state	BE / eV	atomic ratio (%)	FWHM / eV
(a) before ORC	Ru(IV)	462.7	71	2.99
		465.8	29	3.42
(b) after ORC	Ru(IV)	463.0	65	2.78
		465.8	35	3.80

| Sample | O 1s | | | |
	Species	BE / eV	atomic ratio (%)	FWHM / eV
(a) before ORC	O^{2-}	530.0	36	1.73
	OH$^-$	531.2	27	2.20
	H$_2$O	532.3	37	2.26
(b) after ORC	O^{2-}	529.9	20	1.53
	OH$^-$	531.1	48	2.15
	H$_2$O	532.4	32	2.38

82

PtO and Pt(OH)$_2$ (Pt 4f$_{7/2}$: 72.2 eV, Pt 4f$_{5/2}$: 75.4 eV).

The peak areas of Ru 3p$_{3/2}$ and O 1s were decreased. The peak due to Ru 3p$_{3/2}$ is composed of two doublets and their peak positions and peak ratios were not changed by ORC. Meanwhile, the ratio of O^{2-} in oxygen species was decreased and the ratio of OH$^-$ was increased. These results suggest that RuO$_2$ became rough and more OH$^-$ was generated on the RuO$_2$ surface because of dissolution of RuO$_2$ during OER.

From XPS data, it was revealed that the relative amounts of Pt, Ru and oxygen species of 32-Pt-Ru/Au and Pt-Ru$_{mix}$/Au are given by the following equation.[22]

$$C_A/C_B = ((I_A/R_A)/(I_B/R_B)) \quad (4\text{-}1)$$

Where C is concentration, I is peak area which was obtained from XPS spectrum and R is relative sensitivity factor of elements. The relative sensitivity factors of Pt 4f$_{7/2}$, Ru 3p$_{3/2}$ and O 1s are 2.55, 1.30 and 0.66, respectively.[22] The atomic ratios of Pt, Ru and oxygen species were determined as shown in Table 4-3.

Table 4-3. The peak ratio of Pt, Ru and oxygen species of 32-Pt-Ru/Au and Pt-Ru$_{mix}$/Au.

Sample	C_{Pt}/C_{Ru}	$(C_{O^{2-}} + C_{OH^-})/C_{Ru}$	$C_{OH^-}/C_{O^{2-}}$
32-Pt-Ru/Au before ORC	0.32	1.58	2.86
32-Pt-Ru/Au after ORC	0.48	1.56	2.38
Pt-Ru$_{mix}$/Au before ORC	0.39	2.95	0.72
Pt-Ru$_{mix}$/Au after ORC	1.02	3.40	2.33

In the case of 32-Pt-Ru/Au, the atomic ratios of Pt, Ru and oxygen species were not significantly changed by ORC. The estimated Pt/Ru ratio was lower than 1, suggesting that Pt is partially diffused into Au(111) during the heat treatment. The atomic ratio of oxygen species/Ru was about 1.6.

In the case of Pt-Ru$_{mix}$/Au, the atomic ratios of Pt/Ru and oxygen species/Ru were increased by ORC as a result of dissolution of RuO$_2$. The atomic ratio of oxygen species/Ru was estimated as 3.4. The atomic ratio of oxygen species/Ru expected from pure bulk RuO$_2$ is 2. The RuO$_2$ in 32-Pt-Ru/Au had more oxygen

deficiency than that in Pt-Ru$_{mix}$/Au.

4.2.3　XAFS

　　Ru K edge XAFS measurements were carried out

for 32-Pt-Ru/Au and Pt-Ru$_{mix}$/Au without any

electrochemical treatment in air in order to determine

the precise structure in the vicinity Ru in the Pt-Ru

alloy. Figure 4-4 shows Ru K edge XANES spectra

of RuO$_2$ (black), 32-Pt-Ru/Au (blue), Pt-Ru$_{mix}$/Au

(red), Ru metal (green), RuCl$_3$ (pink) and Pt-Ru

complex (orange). The XANES spectrum of

Pt-Ru$_{mix}$/Au shows no significant difference from

that of RuO$_2$, indicating that the structure of the

RuO$_2$ in the Pt-Ru$_{mix}$/Au is similar to that of the

RuO$_2$. On the other hand, the white line intensity of

32-Pt-Ru/Au was higher than that of RuO$_2$ and

Pt-Ru$_{mix}$/Au, suggesting the RuO$_2$ in 32-Pt-Ru/Au

contains H$_2$O. According to the results reported by

Russell et al., the white line intensity of hydrous

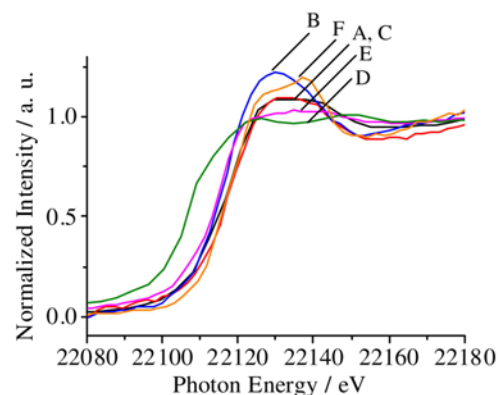RuO$_2$ is higher than that of anhydrous RuO$_2$.[23] Figure

Figure 4-4. Ru K edge XANES spectra of RuO$_2$ (black, A), 32-Pt-Ru/Au (blue, B), Pt-Ru$_{mix}$/Au (red, C), Ru metal (green, D), RuCl$_3$ (pink, E), and Pt-Ru complex (orange, F).
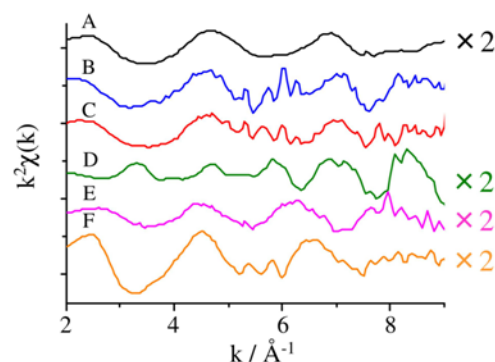

Figure 4-5.　EXAFS oscillations of RuO$_2$ (black, A), 32-Pt-Ru/Au (blue, B), Pt-Ru$_{mix}$/Au (red, C), Ru metal (green, D), RuCl$_3$ (pink, E), and Pt-Ru complex (orange, F).

4-5 and Figure 4-6 show EXAFS oscillations and

radial distribution functions (RDFs) of RuO$_2$ (black), 32-Pt-Ru/Au (blue), Pt-Ru$_{mix}$/Au (red), Ru metal

(green), RuCl$_3$ (pink) and Pt-Ru complex (orange). Table 4-4 shows the fitting results obtained from the

RDFs shown in Figure 4-6. The obtained bond lengths of the standard materials are close to the reported

ones.[23-26] The frequency of the EXAFS oscillations of 32-Pt-Ru/Au and Pt-Ru$_{mix}$/Au are different from

those of Ru metal, the RuCl$_3$ and Pt-Ru complex but similar to that of the RuO$_2$. This result shows the

84

formation of Ru oxide and agrees with the XPS results. The first nearest atom of Ru in Pt-Ru$_{mix}$/Au is oxygen and the obtained bond length of Ru–O of the Pt-Ru$_{mix}$/Au (1.98 Å) is quite close to that of the RuO$_2$. On the other hand, the bond length of Ru–O of 32-Pt-Ru/Au (2.07 Å) is longer than that of RuO$_2$ and Pt-Ru$_{mix}$/Au. This can be explained by the formation of Ru–OH$_2$ bond.[23, 27, 28] It is reported that the bond lengths of Ru–O of Ru(OH$_2$)$_6^{3+}$ and Ru(OH$_2$)$_6^{2+}$ are 2.03 Å and 2.12 Å, respectively.[23, 27] The XPS results of 32-Pt-Ru/Au in O 1s region did not show that H$_2$O is dominant oxygen species. The bond strength of Ru–OH$_2$ is so weak that H$_2$O bonded to Ru can be evaporated in UHV and not detected correctly by XPS, but the bond of Ru–OH$_2$ was observed by the XAFS measurement which was performed at room temperature in air. The RuO$_2$ in 32-Pt-Ru/Au had oxygen deficiency and H$_2$O was coordinated to Ru. The XPS results show that the O 1s peak corresponding to H$_2$O is observed not only in 32-Pt-Ru/Au but also Pt-Ru$_{mix}$/Au. The H$_2$O in Pt-Ru$_{mix}$/Au may be present between RuO$_2$ domains.[29, 30]
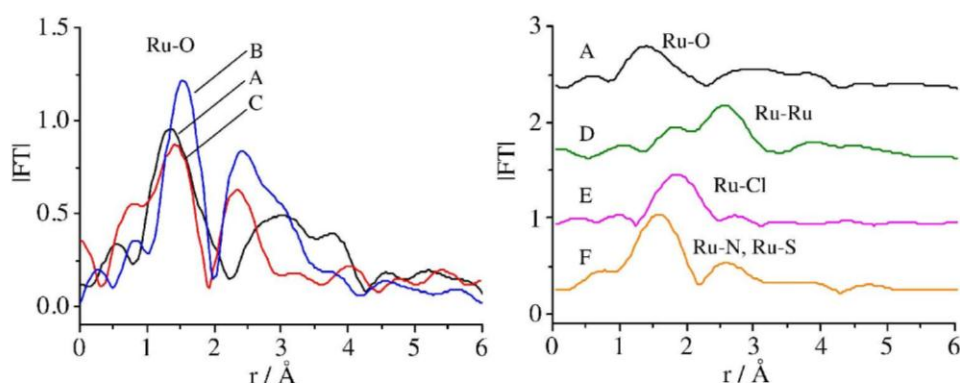

Figure 4-6. RDFs of RuO$_2$ (black, A), 32-Pt-Ru/Au (blue, B), Pt-Ru$_{mix}$/Au (red, C), Ru metal (green, D), RuCl$_3$ (pink, E), and Pt-Ru complex (orange, F).

Table 4-4. The bond lengths estimated by fitting results obtained from RDFs in Figure 4-6

Sample	Bond length / Å	
32-Pt-Ru/Au	Ru-O	2.07
Pt-Ru$_{mix}$/Au	Ru-O	1.98
RuO$_2$	Ru-O	1.97
Ru metal	Ru-Ru	2.68
RuCl$_3$	Ru-Cl	2.20
Pt-Ru complex	Ru-N	2.10

4.2.4   Origin of enhancement of activity and durability of Pt-Ru alloy prepared from Pt-Ru complex

for MOR

Previous works suggested that Pt-Ru alloys which contain hydrous Ru oxide show high MOR activity.[19, 31] Pt-Ru alloys, which are composed of Pt and Ru oxide, are reported to be totally reduced after electrochemical treatment[32-34] but the RuO_2 in 32-Pt-Ru/Au is not reduced even after the electrochemical treatment. According to the bi-functional mechanism of MOR, Ru–OH is a critical component to remove CO adsorbed on a Pt surface. The surface Ru–OH is formed as a result of oxidative adsorption of H_2O to Ru. The XPS results showed that the RuO_2 in 32-Pt-Ru/Au has oxygen deficiency and the XAFS results suggested that Ru–OH_2 bond is formed in 32-Pt-Ru/Au. The coordination site of H_2O to Ru is probably formed by the oxygen deficiency and MOR active Ru–OH is easily formed at the potential where MOR proceeds as follows.

$$ \begin{array}{c} -O \\ -O \end{array}\!\!\!\! Ru-OH_2 \longrightarrow \begin{array}{c} -O \\ -O \end{array}\!\!\!\! Ru-OH \;+\; H^+ + e^- $$
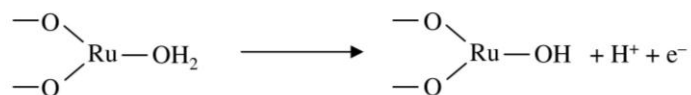
4.3   Conclusion

The origin of enhancement of activity and durability of the Pt-Ru alloy prepared from the Pt-Ru complex for MOR was revealed based on the results of XPS and XAFS measurements. These measurements showed that the structure of RuO_2 in the Pt-Ru alloy prepared from the mixture of K_2PtCl_4 and $RuCl_3$ was very similar to that of bulk RuO_2. Meanwhile, the RuO_2 in the Pt-Ru alloy prepared from the Pt-Ru complex had oxygen deficiency and H_2O was coordinated to Ru. The coordinated H_2O to Ru in the Pt-Ru alloy prepared from the Pt-Ru complex became Ru–OH easily under electrochemical condition. This coordinated H_2O is the origin of the enhancement of Pt-Ru alloy prepared from the Pt-Ru complex for MOR activity and durability.

References

1.   Y. Takasu, T. Kawaguchi, W. Sugimoto and Y. Murakami, *Electrochim. Acta*, 2003, **48**, 3861-3868.

2.   N. Tian, Z. Y. Zhou and S. G. Sun, *J. Phys. Chem. C*, 2008, **112**, 19801-19817.

3.   J. Hernandez, J. Solla-Gullon, E. Herrero, A. Aldaz and J. M. Feliu, *J. Phys. Chem. C*, 2007, **111**, 14078-14083.

4.   I. J. Hsu, D. V. Esposito, E. G. Mahoney, A. Black and J. G. G. Chen, *J. Power Sources*, 2011, **196**, 8307-8312.

5.   H. Naohara, S. Ye and K. Uosaki, *J. Electroanal. Chem.*, 2001, **500**, 435-445.

6.   H. Naohara, S. Ye and K. Uosaki, *Electrochim. Acta*, 2000, **45**, 3305-3309.

7.   S. Park, Y. Xie and M. J. Weaver, *Langmuir*, 2002, **18**, 5792-5798.

8.   M. H. Shao, T. Huang, P. Liu, J. Zhang, K. Sasaki, M. B. Vukmirovic and R. R. Adzic, *Langmuir*, 2006, **22**, 10409-10415.

9.   J. Zhang, Y. Mo, M. B. Vukmirovic, R. Klie, K. Sasaki and R. R. Adzic, *J. Phys. Chem. B*, 2004, **108**, 10955-10964.

10.   J. L. Zhang, M. B. Vukmirovic, Y. Xu, M. Mavrikakis and R. R. Adzic, *Angew. Chem. Int. Ed.*, 2005, **44**, 2132-2135.

11.   R. R. Adzic, J. Wang and B. M. Ocko, *Electrochim. Acta*, 1995, **40**, 83-89.

12.   M. Baldauf and D. M. Kolb, *J. Phys. Chem.*, 1996, **100**, 11375-11381.

13.   M. D. Obradovic, B. N. Grgur, S. L. Gojkovic and L. M. Vracar, *Journal of Solid State Electrochemistry*, 2006, **11**, 77-83.

14.   T. Ghosh, M. B. Vukmirovic, F. J. DiSalvo and R. R. Adzic, *J. Am. Chem. Soc.*, 2010, **132**, 906-+.

15.   F. Maroun, F. Ozanam, O. M. Magnussen and R. J. Behm, *Science*, 2001, **293**, 1811-1814.

16.   Y. Takasu, T. Fujiwara, Y. Murakami, K. Sasaki, M. Oguri, T. Asaki and W. Sugimoto, *J. Electrochem. Soc.*, 2000, **147**, 4421-4427.

17.   T. Okada, N. Arimura, C. Ono and M. Yuasa, *Electrochim. Acta*, 2005, **51**, 1130-1139.

18.   T. L. Barr, *J. Phys. Chem.*, 1978, **82**, 1801-1810.

19.   D. R. Rolison, P. L. Hagans, K. E. Swider and J. W. Long, *Langmuir*, 1999, **15**, 774-779.

20.   A. Foelske, O. Barbieri, M. Hahn and R. Kotz, *Electrochem. Solid-State Lett.*, 2006, **9**, A268-a272.

21.   R. Kotz, H. J. Lewerenz and S. Stucki, *J. Electrochem. Soc.*, 1983, **130**, 825-829.

22.   C. D. Wagner, L. E. Davis, M. V. Zeller, J. A. Taylor, R. H. Raymond and L. H. Gale, *Surf. Interface Anal.*, 1981, **3**, 211-225.

23.   D. A. McKeown, P. L. Hagans, L. P. L. Carette, A. E. Russell, K. E. Swider and D. R. Rolison, *J. Phys. Chem. B*, 1999, **103**, 4825-4832.

24.   A. Yamaguchi, N. Hiyoshi, O. Sato, M. Osada and M. Shirai, *Catal. Lett.*, 2008, **122**, 188-195.

25.   F. Laurent, E. Plantalech, B. Donnadieu, A. Jimenez, F. Hernandez, M. Martinez-Ripoll, M. Biner and A. Llobet, *Polyhedron*, 1999, **18**, 3321-3331.

26.   L. S. Sarma, C. H. Chen, S. M. S. Kumar, G. R. Wang, S. C. Yen, D. G. Liu, H. S. Sheu, K. L. Yu, M. T. Tang, J. F. Lee, C. Bock, K. H. Chen and B. J. Hwang, *Langmuir*, 2007, **23**, 5802-5809.

27.   G. Wilkinson, R. D. Gillard and J. A. McCleverty, *Comprehensive Coordination Chemistry*, 1987.

28.   J. R. Osman, J. A. Crayston and D. T. Richens, *Inorg. Chem.*, 1998, **37**, 1665-+.

29.   P. S. Patil, E. A. Ennaoui, C. D. Lokhande, M. Muller, M. Giersig, K. Diesner and H. Tributsch, *Thin Solid Films*, 1997, **310**, 57-62.

30.   W. Dmowski, T. Egami, K. E. Swider-Lyons, C. T. Love and D. R. Rolison, *J. Phys. Chem. B*, 2002, **106**, 12677-12683.

31.   L. Cao, F. Scheiba, C. Roth, F. Schweiger, C. Cremers, U. Stimming, H. Fuess, L. Q. Chen, W. T. Zhu and X. P. Qiu, *Angew. Chem. Int. Ed.*, 2006, **45**, 5315-5319.

32.   W. E. O'Grady, P. L. Hagans, K. I. Pandya and D. L. Maricle, *Langmuir*, 2001, **17**, 3047-3050.

33.   S. Stoupin, E. H. Chung, S. Chattopadhyay, C. U. Segre and E. S. Smotkin, *J. Phys. Chem. B*, 2006, **110**, 9932-9938.

34.   S. Stoupin, H. Rivera, Z. R. Li, C. U. Segre, C. Korzeniewski, D. J. Casadonte, H. Inoue and E. S. Smotkin, *Phys. Chem. Chem. Phys.*, 2008, **10**, 6430-6437.

Chapter 5

PREPARATION OF METAL FREE NITROGEN DOPED CARBON MATERIALS FOR OXYGEN REDUCTION REACTION CATALYST BY BOTTOM-UP METHODS

5.1   Introduction

As described in Chapter 1, the nitrogen doped carbon materials have been focused on as less expensive ORR catalysts. Generally, these materials are prepared by chemical vapor deposition (CVD),[1, 2] NH_3 treatment for carbon materials,[3, 4] or the pyrolysis of organic materials with transition-metals catalysts such as Fe and Co as catalysts.[5-8] Controlling nitrogen concentrations and C–N bonding configurations found in pyrrole, pyridine, and graphite-like nitrogen is very important because ORR activity depends on these parameters.[9] However, it is difficult to control the C–N bonding configurations and nitrogen concentrations of products, because the methods require high temperatures. In addition, these methods often need transition-metals as catalysts to prepare nitrogen doped carbon materials. These transition metals, which can act as ORR active sites and catalyze the decomposition of H_2O_2, may remain in the nitrogen doped carbon materials.[10, 11] Any remaining transition metals can make difficult to understand the ORR active sites in nitrogen doped carbon materials, and they can also allow the formation of a superoxide from H_2O_2, which damages electrodes and polymer electrolyte membranes. With nitrogen doped carbon materials, ORR can proceed with more than two electrons. For example, on nitrogen doped carbon materials prepared by catalytic CVD using acetonitrile, the electron number for the ORR is 2.3[7] and on those materials prepared by the pyrolysis of ionic liquids, the electron number for the ORR is 3.2,[12] suggesting the formation of not only H_2O but also H_2O_2 during ORR. To not only understand the ORR active site but also to improve ORR activity, the preparation of nitrogen doped carbon materials with controlled nitrogen concentration and C–N bonding configurations is required without using transition metals.

It is thought that such materials can be prepared by the heat treatment of new organic materials or synthesized from aromatic molecules. Recently, nitrogen doped carbon materials with high ORR activity

were prepared without transition metals by the pyrolysis of ionic liquids[12] and silk.[13, 14]

However, studies of the synthesis of nitrogen doped carbon materials with controlled nitrogen concentrations and C–N bonding configurations are still limited. Graphene, which is a two-dimensional carbon materials can be prepared by various methods, including synthesis from aromatic molecules.[15-19] On the metal surface, it is possible to prepare large amounts of graphene with controlled structures. Fasel et al. synthesized graphene structures on metal single crystal surfaces under ultra high
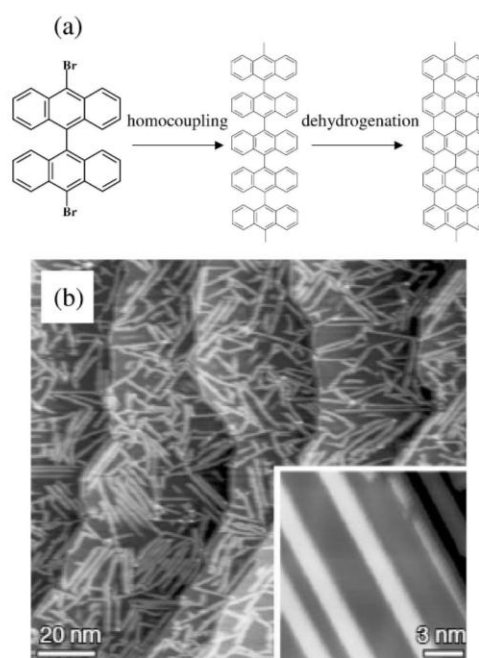
Figure 5-1. (a) A proposed mechanism of grapherization of polyaromatic molecules on Au(111) surface. (b) STM images of graphene ribbons prepared by the method shown in Figure 5-1 (a).   .

vacuum (UHV) conditions using polyaromatic molecules with halogen groups.[18] Graphene structures can be obtained by heat-induced coupling and dehydrogenation reactions of molecules adsorbed on metal surfaces (Figure 5-1). The metal surface acts as catalysts for the dissociation of C–halogen bonds and substrates of graphene. The reactions proceed at a relatively mild temperature that will not cause the decomposition of organic molecules (400 ℃), and the method can be used to prepare nitrogen doped graphene structures with well-controlled nitrogen concentrations and C–N bonding configurations.

In this chapter, two different approaches were tried to obtain metal-free ORR catalysts. First, a novel polyaromatic molecule, penta-2-(p-ethynylphenyl)-ethynylpyridine (pepy) (Figure 5-2) was modified on highly oriented pyrolytic graphite (HOPG) and then decomposed by heat treatment at various temperatures under Ar flow. The effect of temperature on their structure and ORR activity was investigated by XPS, Raman spectroscopy, and electrochemical measurements. The HOPG surface modified with pepy was heat treated at 500, 600, 700 and 800 ℃ for 30 min under Ar flow. Pepy heat treated at 500, 600, 700, and 800

℃ is denoted as 500py, 600py, 700py, and 800py, respectively in this chapter. Secondary, polyaromatic molecules with bromo groups shown in Figure 5-3 (9,10-dibromoanthracene (DBA), 10,10'-dibromo, 9,9'-bianthryl (DBBA), and 5,15-dibromo, 10,20-diphenylporphine (DBP)) were used to prepare the graphene structures. These molecules were modified on Au(111) by a wet process and heat treated under Ar flow.
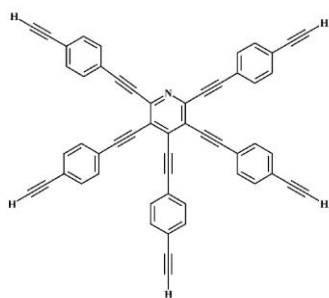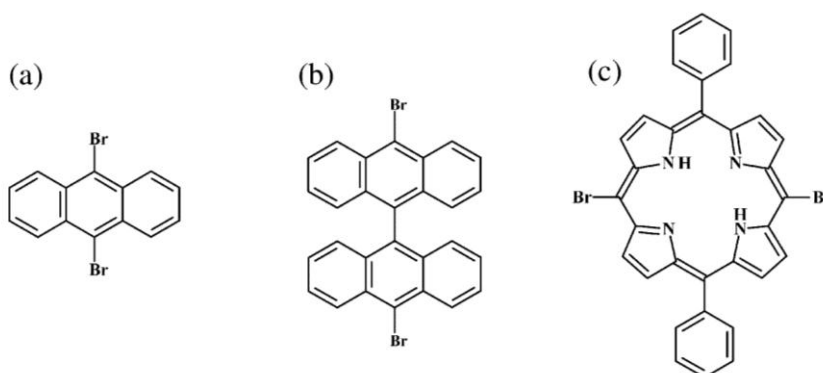

Figure 5-2. A structure of pepy.

Figure 5-3. Structures of (a) DBA, (b) DBBA and (c) DBP.

5.2 ORR Catalyst Prepared by Pyrolysis of Penta-2-(*p*-ethynylphenyl)-ethynylpyridine

5.2.1 Structural characterization

XPS measurements were carried out to investigate the effect of heat treatment temperature on C–N bonding configurations and nitrogen concentration in heat treated pepy. Figure 5-4 shows wide-scan XP spectra of (a) bare HOPG, (b) pepy on HOPG, (c) 500py, (d) 600py, (e) 700py, and (f) 800py. The peaks corresponding to O 1s and C 1s were clearly observed, and they originate from HOPG.

Figure 5-5 shows narrow-scan XP spectra in the N 1s region of (a) bare HOPG, (b) pepy on HOPG, (c) 500py, (d) 600py, (e) 700py and (f) 800py. The peak from the N 1s of pepy on HOPG appeared at 400.6 eV. The peak position in pepy was 2.1 eV higher than that of the pyridine-like nitrogen (398.5 eV). It was previously reported that the peak position of N 1s in acridine is 0.7 eV higher than that of pyridine like nitrogen.[20] The binding energy of N 1s in pyridine-like nitrogen in a highly π-conjugated molecules can be more positive than pyridine alone. The peak position of N 1s did not change with heat treatment, suggesting that the C–N bonding configuration of heat treated pepy is totally pyridine-like nitrogen. However, the peak area of N 1s decreases as heat treatment temperature increases.

Figure 5-6 shows the plot of heat treatment temperature against the ratio of nitrogen remaining after heat treatment. At 500ºC, the peak area of N 1s was only 60 % of the peak area of non-treated pepy, and the ratio of remaining nitrogen was gradually decreased as the heat treatment temperature increased.
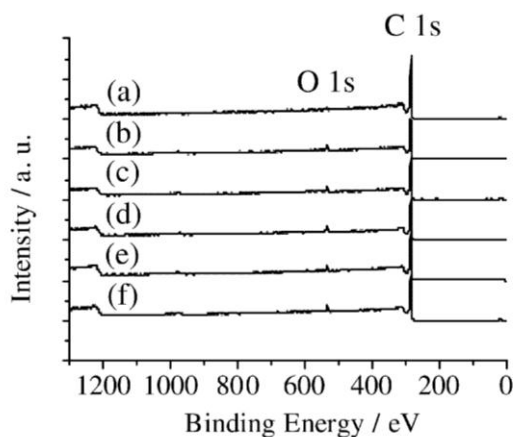

Figure 5-4. Wide-scan XP spectra of (a) bare HOPG, (b) pepy on HOPG, (c) 500py, (d) 600py, (e) 700py and (f) 800py..
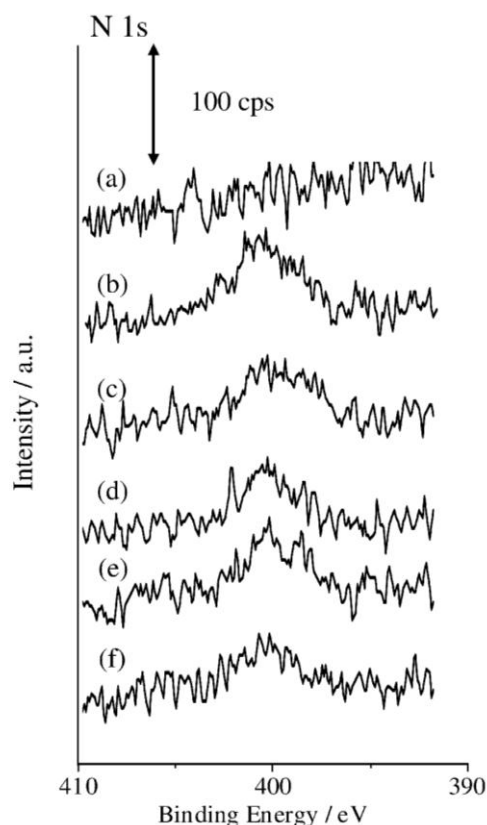

Figure 5-5. Narrow-scan XP spectra in N 1s region of (a) bare HOPG, (b) pepy on HOPG, (c) 500py, (d) 600py, (e) 700py and (f) 800py.
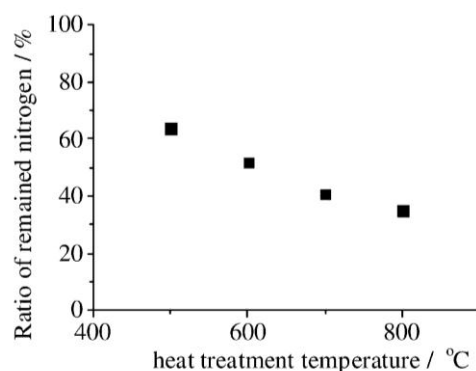
Figure 5-6. A plot of heat treatment temperature against the ratio of remaining nitrogen after heat treatment.

Raman measurements were carried out to investigate the crystallinity of heat treated pepy. Figure 5-7 shows Raman spectra of (a) pepy, (b) 500py, (c) 600py, and (d) 700py on SiO_2. No peaks from pepy were observed in Figure 5-7 (a). In Figures 5-7 (b)-(d), peaks corre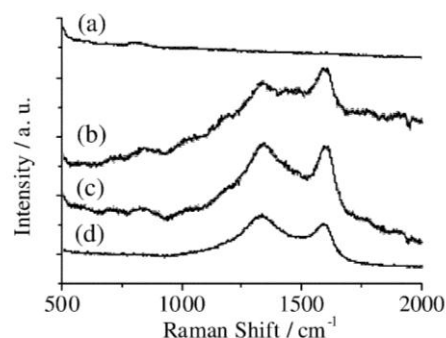sponding to the D band (1330 cm^{-1}) and G band (1590 cm^{-1}) were observed. Figure 5-8 (a) shows the peak ratios of D and G bands (I(D)/I(G)) for 500py, 600py, and 700py. The ratio

Figure 5-7. Raman spectra of (a) pepy, (b) 500py, (c) 600py and (d) 700py on SiO_2.

can be used to determine the crystallinity of carbon materials (Figure 5-8 (b)).[21] The I(D)/I(G) of heat treated pepy increased as the heat treatment temperature increased, which suggests that the crystal structure changes from amorphous carbon to nanocrystalline graphite.
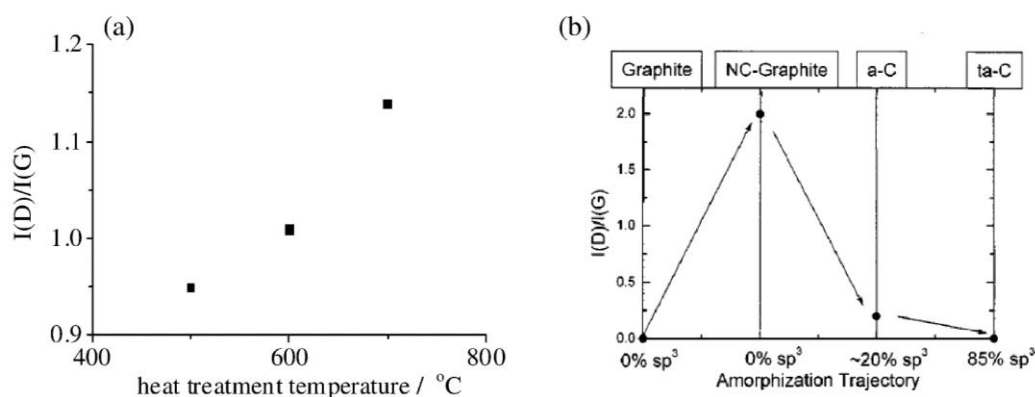

Figure 5-8. (a) A plot of heat treatment temperature against the ratio of intensities of D and G bands. (b) Relationship between carbon bonding configuration and Raman spectra of carbon materials from ref 21.

93

The surface structure of HOPG modified with heat treated pepy was investigated by STM. Figure 5-9 shows the STM images of (a) 600py and (b) 700py. Aggregations with an average diameter of 20 nm and height of 10 nm likely correspond to nanocrystalline graphite. The size of obtained nitrogen doped carbon material is small and the STM results agree with the Raman results.
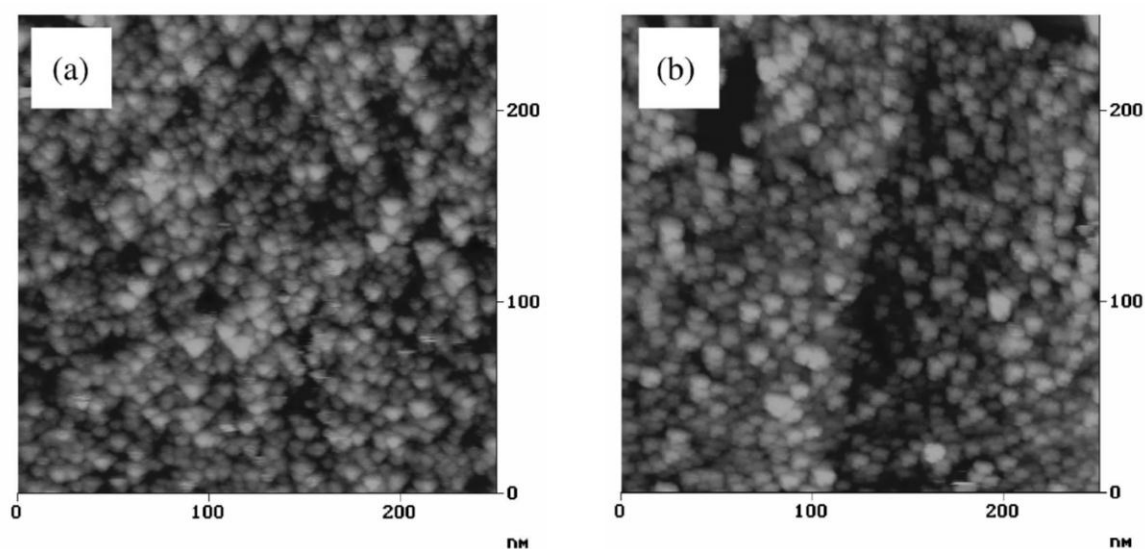

Figure 5-9. STM images of (a) 600py and (b) 700py. ($E_{bias} = 0.4$ V, $I_{tc} = 0.1$ nA)

5.2.2   ORR activity

The ORR activity of heat treated pepy was investigated. Figure 5-10 shows the CVs of (a) HOPG, (b) pepy on HOPG, (c) 500py, (d) 600py, (e) 700py and (f) 800py in 0.1 M HClO$_4$ solutions saturated with Ar (black curve) or O$_2$ (red curve). The reductive current corresponding to ORR was observed and started flowing at around 0 V. The ORR activity of pepy was less than that of HOPG. Although the ORR activity of pepy was improved with heat treatment, heat treated pepy still did not have a high ORR activity in acidic solutions.

Figure 5-11 shows the CVs of (a) HOPG, (b) pepy on HOPG, (c) 500py, (d) 600py, (e) 700py, and 800py in 0.1 M KOH solutions saturated with Ar (black curve) or O$_2$ (red curve). The reductive current corresponding to ORR was observed and began to flow at around −0.2 V. In alkaline solutions, heat treated pepy, especially, 600py and 700py, had large reductive currents corresponding to ORR. Their ORR
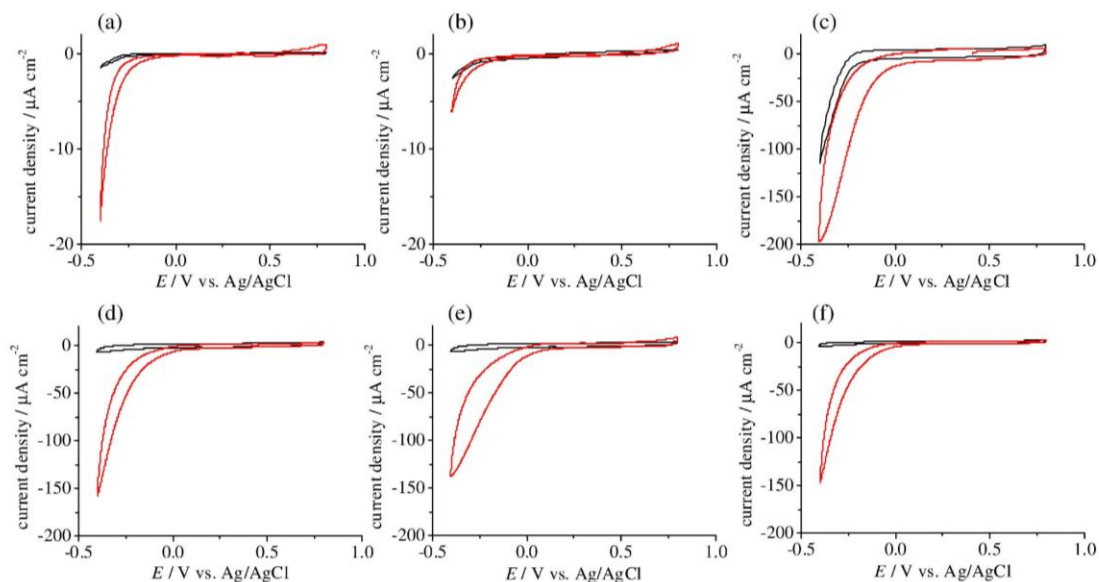
94

Figure 5-10. CVs of (a) bare HOPG, (b) pepy on HOPG, (c) 500py, (d) 600py, (e) 700py, and (f) 800py in 0.1 M HClO$_4$ solutions under Ar (black) and O$_2$ (red). Scan rate = 10 mV s^{-1}.
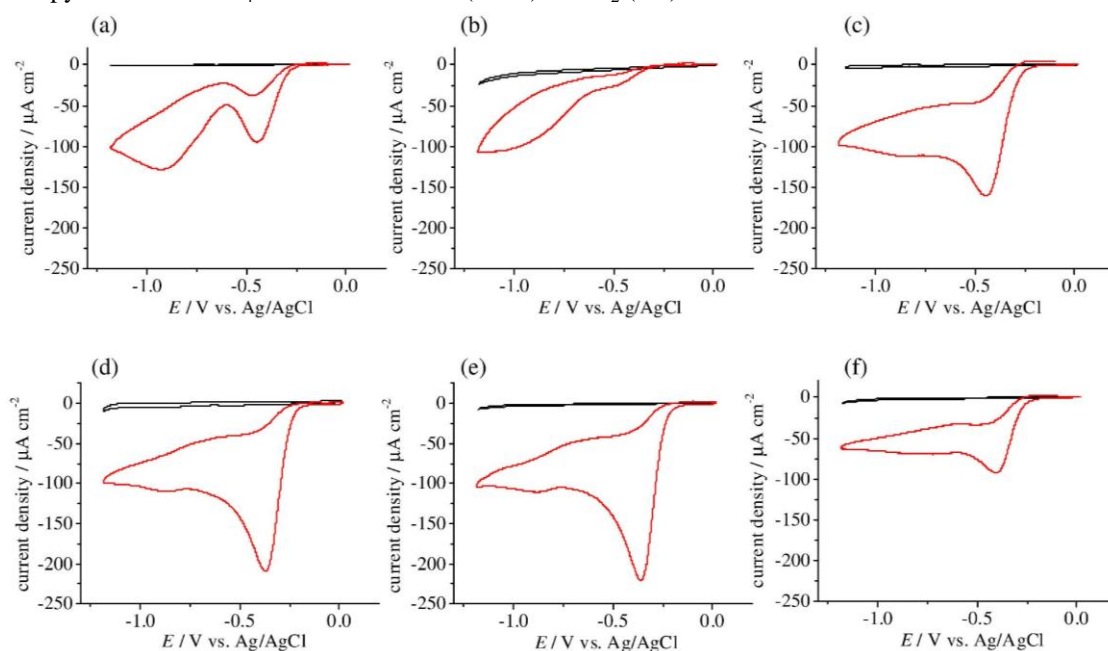

Figure 5-11. CVs of (a) bare HOPG, (b) pepy on HOPG, (c) 500py, (d) 600py, (e) 700py, and (f) 800py in 0.1 M KOH solutions under Ar (black) and O$_2$ (red). Scan rate = 10 mV s^{-1}.

activities in alkaline solution were investigated by rotating disk electrode measurements. Figure 5-12 shows LSVs of (a) HOPG, (b) pepy on HOPG, (c) 500py, (d) 600py, (e) 700py, and 800py in 0.1 M KOH solutions saturated with O$_2$. The potential was swept from 0.02 V to −1.20 V at a scan rate of 10 mV s^{-1} and rotation rate from 500 to 2500 rpm. The ORR current of HOPG modified with heat treated pepy started to flow at ca. −0.20 V. It increased as the electrode potential became more positive and then the limiting current was
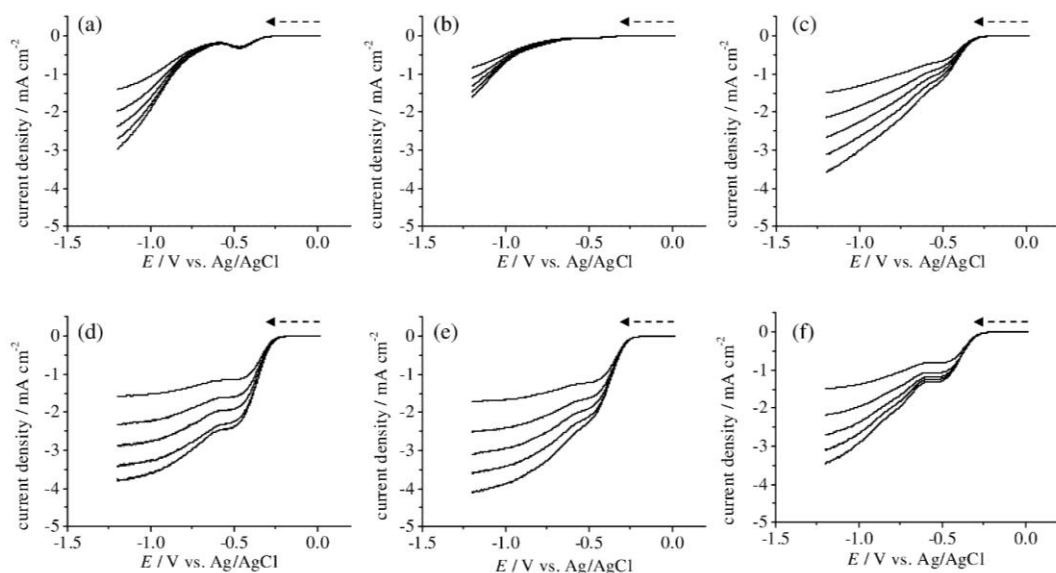
95

Figure 5-12. LSVs of (a) bare HOPG, (b) pepy on HOPG, (c) 500py, (d) 600py, (e) 700py, and (f) 800py in 0.1 M KOH solutions saturated with O_2. Scan rate = 10 mV s^{-1}.
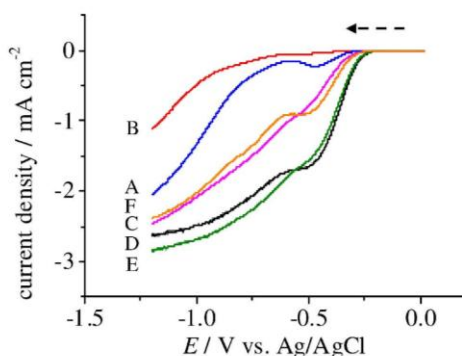

Figure 5-13. LSVs of bare HOPG (blue, A), pepy on HOPG. (red, B), 500py (pink, C), 600py (black, D), 700py (green E), and 800py (orange, F) in 0.1 M KOH solutions saturated with O_2. Scan rate = 10 mV s^{-1}. Rotation rate = 1500 rpm.

observed for 600py and 700py. Figure 5-13 shows LSVs of HOPG, pepy on HOPG, 500py, 600py, 700py, and 800py in 0.1 M KOH solutions saturated with O_2 at a scan rate of 10 mV s^{-1} and a rotation rate of 1500 rpm. In the more positive potential region, 600py had the highest ORR activity. The relationship between the diffusion-limiting current density and rotation rate is given by the Levich equation, shown in Chapter 3, using a bulk oxygen concentration ($C_{O2}{}^* = 1.2 \times 10^{-6}$ cm^2 s^{-1})[22] and the diffusion coefficient of oxygen molecules in 0.1 M KOH solution ($D = 1.9 \times 10^{-5}$ cm^2 s^{-1}).[22] From the Levich plot (i_L versus $\omega^{1/2}$) shown in Figure 5-14 for the limiting current at −1.10 V, the number of electrons in the ORR was estimated to be

96

2.22 for 600py and 2.29 for 700py, and these results show that O_2 undergoes a two electron reduction process (5-1).

$$O_2 + H_2O + 2e^- \rightarrow HO_2^- + OH^- \qquad (5\text{-}1)$$

The kinetic current and rate constant for ORR were analyzed with the Koutecky-Levich (K-L) equation shown in Chapter 3. Figure 5-15 shows the K-L plots of (a) 500py, (b) 600py, (c) 700py, and (d) 800py using the data at various potentials from Figure 5-13. The kinetic currents and rate constants determined at various potentials are summarized in Table 5-1. The 600py had the largest rate constant for ORR at –0.4 V and –0.5 V.
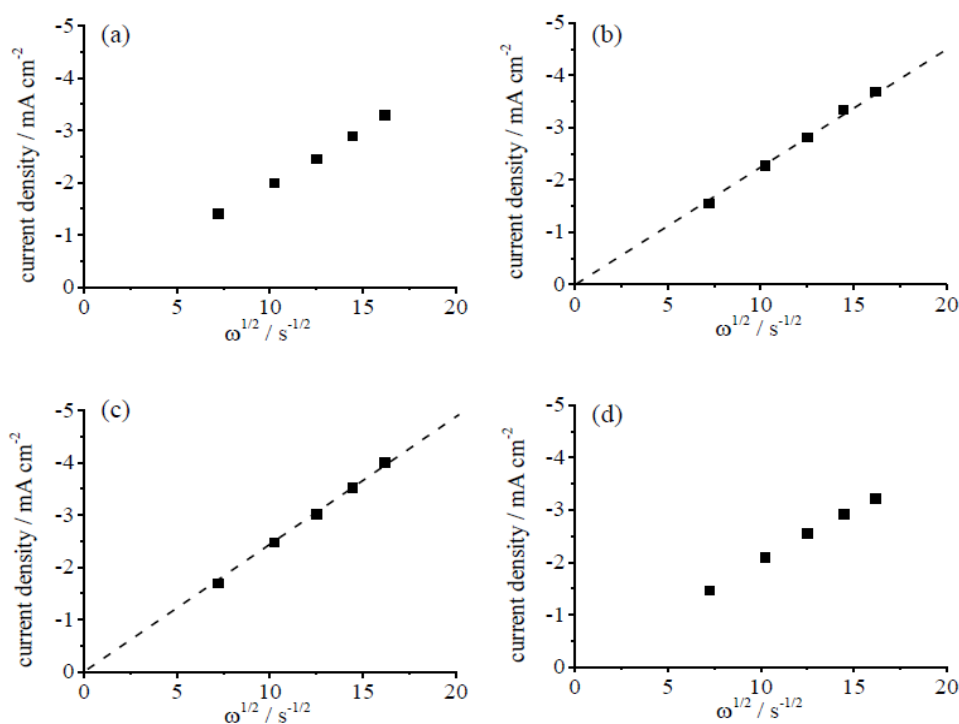

Figure 5-14. Levich plots of (a) 500py, (b) 600py, (c) 700py, and (d) 800py at –1.1 V vs. Ag/AgCl.

The effect of structure on the ORR activity of heat treated pepy was investigated. The kinetic current at –0.5 V was plotted against the concentration of remaining nitrogen and the I(D)/I(G) of heat treated pepy (Figure 5-16). XPS results showed that the concentration of nitrogen expected to be ORR active decreased

as the heat treatment temperature increased. The concentration of nitrogen in 800py was so low that 800py showed poor ORR activity. Meanwhile, 500py, which had the highest nitrogen concentration of the prepared catalysts, also showed poor ORR activity. Raman results showed that the crystalline structure of 500py was close to amorphous carbon, and the amorphous carbon was converted to nanocrystalline graphite at higher heat treatment temperatures. These results show that both nitrogen concentration and the crystallinity of nitrogen doped carbon materials affect ORR activity. Heat treated pepy with a high nitrogen concentration and high crystallinity, i.e., 600py and 700py, had high ORR activity.
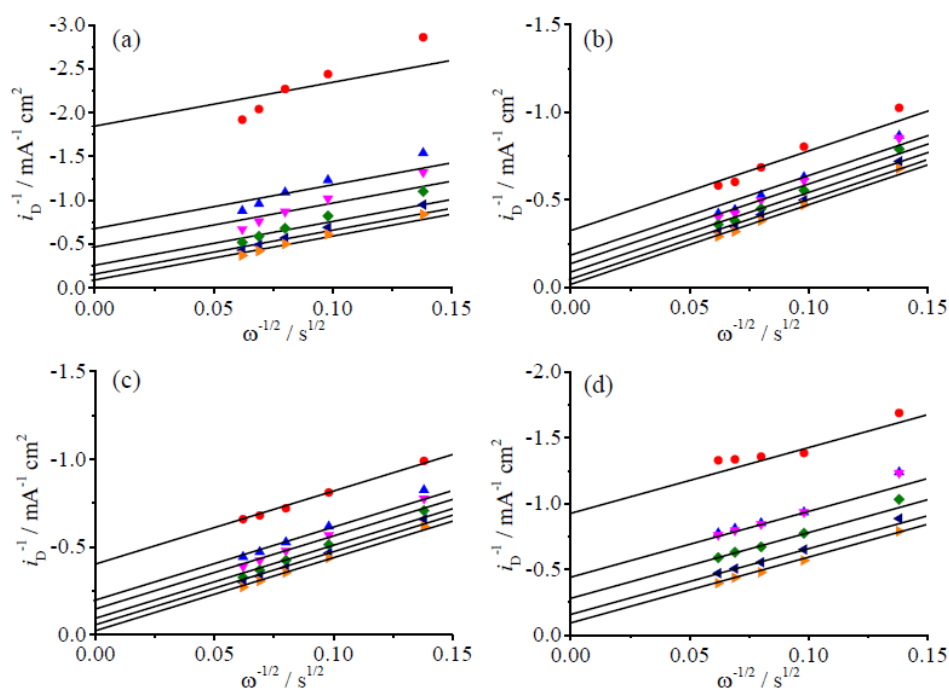

Figure 5-15. Koutecky-Levich plots of (a) 500py, (b) 600py, (c) 700py, and (d) 800py at −0.4 (red circle), −0.5 (blue triangle), −0.6 (pink triangle), −0.7 (green diamond), −0.8 (black triangle) and −0.9 V (orange triangle).

Table 5-1. The kinetic currents (i_k) and rate constants (k) of the 500py, 600py, 700py and 800py at various potentials.

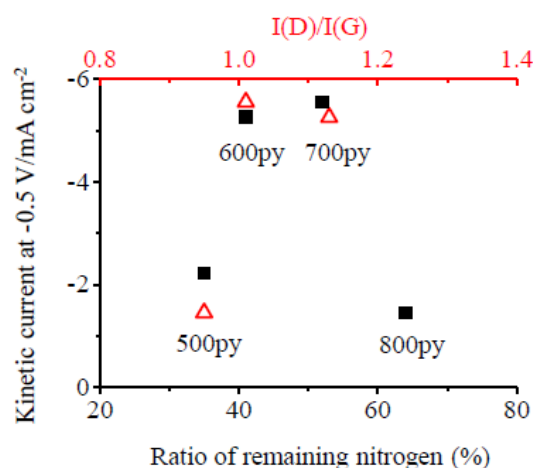| Sample	500py		600py		700py		800py	
E / V	i_k / mA cm^{-2}	k / cm s^{-1}	i_k / mA cm^{-2}	k / cm s^{-1}	i_k / mA cm^{-2}	k / cm s^{-1}	i_k / mA cm^{-2}	k / cm s^{-1}
−0.4	−0.53	0.004	−2.94	0.024	−2.33	0.019	−1.11	0.009
−0.5	−1.45	0.012	−5.56	0.044	−5.26	0.042	−2.22	0.018
−0.6	−2.13	0.017	−6.67	0.053	−6.99	0.056	−2.27	0.018
−0.7	−4.08	0.032	−10.00	0.080	−11.36	0.091	−3.51	0.028
−0.8	−5.88	0.047	−13.89	0.111	−21.74	0.174	−6.25	0.050
−0.9	−13.33	0.107	−31.25	0.250	−52.63	0.421	−11.11	0.089

Figure 5-16. The plots of kinetic current at –0.5 V against ratio of remaining nitrogen and I(D)/I(G).

5.3 ORR Catalyst Prepared by Heat Induced Chemical Reaction of Polyaromatic Molecules with Bromo Group

5.3.1 9,10-dibromoanthracene (DBA)

The preparation of a graphene structure was attempted by heating DBA on Au(111). Figure 5-17 (a) shows the STM images of Au(111) modified with DBA. A long range ordered adlayer was clearly observed. The elongated spots ca. 1 nm in length and ca. 0.3 nm in width correspond to the DBA molecules. The longest distance between each bright spot was estimated to be ca. 1.5 nm, which is close to five times the Au lattice distance (0.29 nm),[23] and the shortest nearest distance between each bright spot was estimated to be ca. 1.2 nm, which is close to four times the Au lattice distance. The lattice angle of DBA adlayer was the same as that of Au (60º). These results suggest that the adlayer structure of DBA on Au(111) has a (4 × 5) structure as shown in Figure 5-17 (b). The ordered DBA adlayer on Au(111) disappeared with heat treatment. Figures 5-17 (c) and (d) show the STM images of DBA modified Au(111) after heat treatment at 250ºC and 460ºC, respectively. Instead of the anticipated ribbon structures, aggregations were observed. Fasel et al. reported that the height of graphene ribbons estimated by STM was 0.16 nm, which is shorter than that of regular graphene.[18] It is possible that the obtained DBA layer was so densely-packed that DBA had marginal mobility, and the anticipated intermolecular coupling reaction did not proceed efficiency
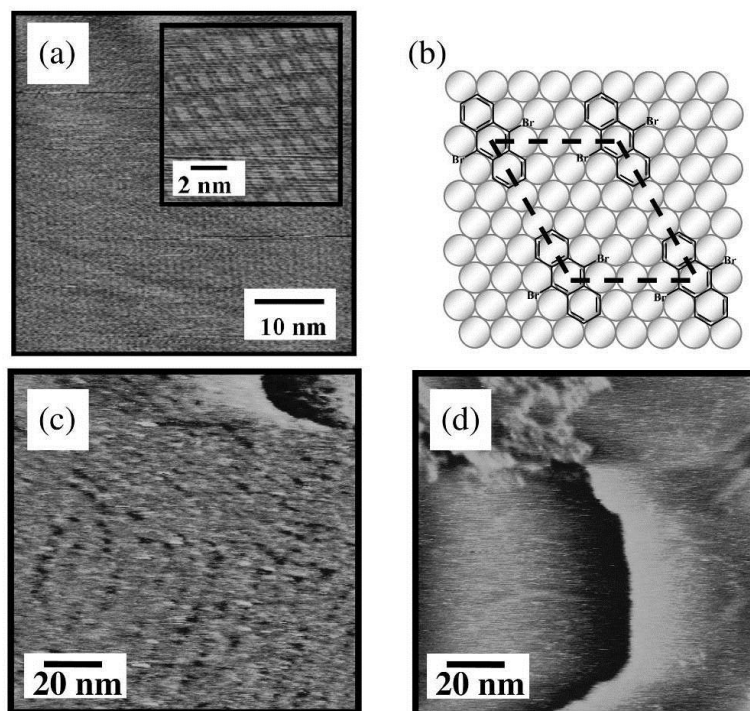
Figure 5-17. (a) STM images of Au(111) modified with DBA. (b) A proposed ad-structure of DBA on Au(111). STM images of Au(111) modified with DBA heat treated at 250ºC (c) and 460ºC (d). (E_{bias} = 0.3 V, I_{tc} = 0.8 nA)

during heat treatment.

Next, the DBA layer with low coverage was prepared on Au(111) by immersing Au(111) in low-concentrated DBA in dichloromethane for 10 s. Au(111) modified with DBA was heat treated at 460 ºC. Figure 5-18 (a) shows an STM image of Au(111) modified with low-coverage DBA. The image observed from Au(111) modified with DBA was similar to that of a phase separated structure than Au(111) modified with DBA shown in Figure 5-17 (a). The individual DBA molecules were not observed. After heat treatment at 460 ºC, aggregated structures and Au(111) surface reconstruction structures appeared (Figure 5-18 (b)). Considering the anticipated grapherization steps, a diradical, which is very unstable, could form from DBA during heat treatment on Au(111). A molecule that can form a more stable radical, such as DBBA, could be used for the preparation of graphene ribbon structures.
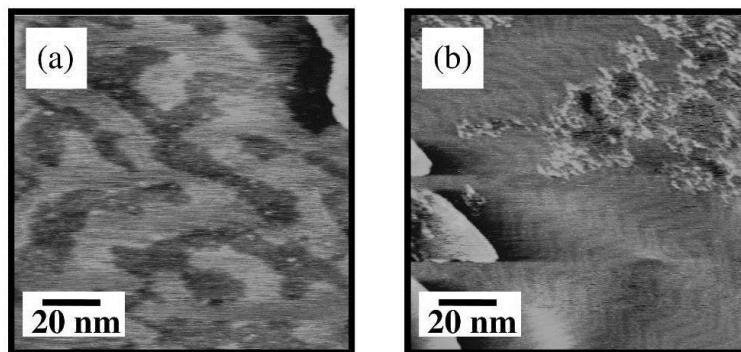
100

Figure 5-18. STM images of (a) Au(111) modified with low-coverage DBA and (b) heat treated DBA on Au(111) at 460ºC. ($E_{bias} = 0.3$ V, $I_{tc} = 0.8$ nA)

5.3.2 10,10'-dibromo, 9,9'-bianthryl (DBBA)

Figure 5-19 (a) shows an STM image of Au(111) modified with DBBA. An ordered structure of DBBA adlayer was not observed. Figure 5-19 (b) shows an STM image of Au(111) modified with heat treated DBBA at 460 ºC. Aggregated structures together with bright spots 1 nm in diameter, were observed in the enlarged STM image (inset of Figure 5-19 (b)). The size of bright spots was very similar to the size of DBBA, suggesting that the intermolecular reaction does not proceed well during heat treatment. Next, a low coverage DBBA layer was prepared on Au(111), and Au(111) modified with DBBA was heat treated at 460ºC. Figure 5-19 (c) shows an STM image of Au(111) after DBBA modification and its heat treatment at 460ºC. Instead of graphene ribbon structures, aggregations were observed and in the region without aggregations, Au(111) surface reconstruction structures appeared. The Au surface may have less interaction
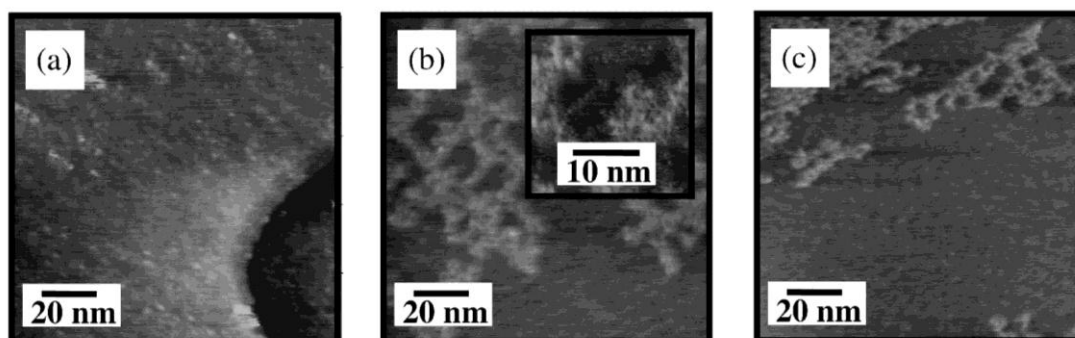

Figure 5-19. STM images of (a) Au(111) modified with DBBA, (b) heat treated DBBA on Au(111) at 460ºC and (c) heat treated DBBA with low coverage on Au(111) at 460ºC. ($E_{bias} = 0.3$ V, $I_{tc} = 0.8$ nA)

101

with generated radicals, and the intermolecular coupling reaction may not proceed well on the Au(111) surface.

5.3.3 5,15-dibromo, 10,20-diphenylporphine (DBP)

The preparation of graphene structures containing nitrogen was attempted by heating Au(111) modified with DBP. Figure 5-20 (a) shows the STM images of Au(111) modified with DBP. A long range ordered adlayer can be clearly observed. A high-resolution image (inset of Figure 5-20 (a)) showed that the size of the bright spots (diameter 0.2 nm) was much smaller than those of previously reported porphyrines. The assembly of 16 bright spots ordered in a diamond shape probably corresponds to one DBP molecule. The longest distance between each bright spot was estimated to be ca. 2.0 nm, which is close to 7 times the Au lattice distance and the shorter nearest distance between each bright spot was estimated as ca. 1.7 nm, which is close to six times the Au lattice distance. The lattice angle of DBA adlayer is the same as Au (60º). These results suggest that the adlayer structure of DBA on Au(111) is a (6 × 7) structure, shown in Figure 5-20 (b). Figure 5-20 (c) shows an STM image of Au(111) modified with heat treated DBP at 460 ℃. The ordered DBP adlayer on Au(111) disappeared with heat treatment, and aggregated structures (height 1 nm) were observed.
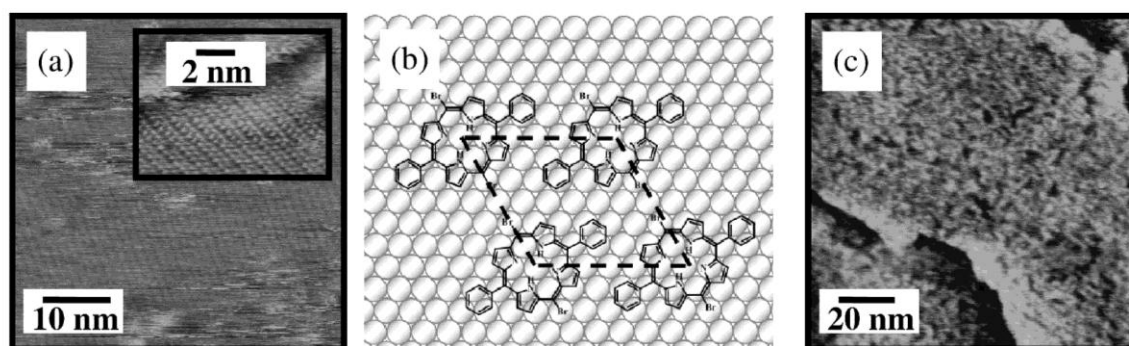

Figure 5-20. (a) STM images of Au(111) modified with DBP. (b) A proposed ad-structure of DBP on Au(111). (c) An STM image of Au(111) modified with DBA heat treated at 460℃. (E_{bias} = 0.3 V, I_{tc} = 0.8 nA)

Figures 5-21 (a) and (b) show the gap-mode Raman spectra of DBP and heat treated DBP at 460℃ on Au(111), respectively. In Figure 5-21 (a), peaks from porphyrin were observed and summarized in Table

5-2.[24] After the heat treatment at 460ºC, the peaks observed in Figure 5-21 (a) completely disappeared, suggesting the decomposition of DBP (Figure 5-21 (b)).
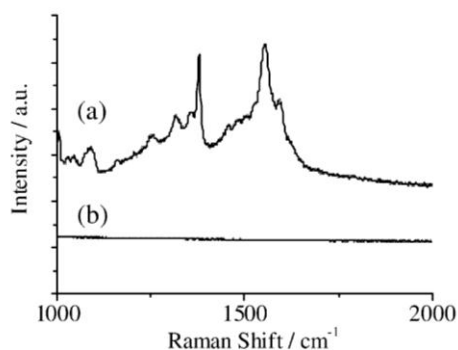

Figure 5-21. Gap-mode Raman spectra of (a) DBP and (b) heat treated DBP on Au(111) at 460ºC.

Table 5-2. Peak identification of DBP obtained in Figure 5-21.

1553 cm^{-1}	$\upsilon(C_\beta C_\beta)$
1378 cm^{-1}	$\upsilon(\text{Pyr half-ring})_{sym}$
1317 cm^{-1}	$\upsilon(\text{Pyr half-ring})_{sym}$
1256 cm^{-1}	$\upsilon(C=C)$
1089 cm^{-1}	$\delta(C_\beta H)$
1045 cm^{-1}	$\upsilon(C=C)$
1029 cm^{-1}	$\upsilon(\text{Pyr half-ring})_{asym}$
1004 cm^{-1}	$\upsilon(\text{Pyr breathing})$

Figure 5-22 shows wide-scan XP spectra of (a) DBP and (b) heat treated DBP on Au(111) at 460ºC. The peaks corresponding to Au and C were also observed.

Figure 5-23 shows narrow-scan XP spectra of N 1s, C 1s, and Br 3d$_{5/2}$ for (a) DBP and (b) heat treated DBP on Au(111) at 460ºC. In Figure 5-23 (a), peaks from N 1s and C 1s, corresponding to pyrrole-like nitrogen[25] and aromatic carbon,[26] were observed at 400.0 and 284.9 eV, respectively, suggesting the adsorption of DBP on Au(111). The
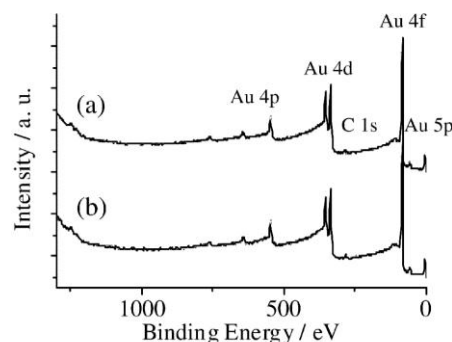

Figure 5-22. Wide-scan XP spectra of (a) DBP and (b) heat treated DBP on Au(111) at 460ºC.

peak corresponding to Br 3d$_{5/2}$ (70 eV) was not observed. Bent et al. reported that the C–I bond of iodobenzene adsorbed on Cu(111) can be cleaved at temperatures lower than 300 K under UHV.[27] The C–Br bond of DBP may cleave in the solvent and air. After heat treatment at 460ºC, the peak corresponding to N 1s disappeared, and the peak from C 1s shifted negatively, suggesting the complete decomposition of DBP. The heat induced coupling reaction of DBP did not proceed well on the Au(111) surface.

Finally, the ORR activity of heat treated DBP was investigated. Figure 5-24 shows the LSVs of bare Au (111) (black, A), Au(111) modified with DBP (blue, B) and heat treated DBP at 460ºC (red, C). Au(111)

modified with DBP had less ORR activity than Au(111), suggesting the inhibition of ORR by ad-molecules. The ORR activity of DBP improved with the heat treatment at 460ºC but was less than that of Au(111). The Raman and XPS results show that DBP decomposed, and the composites did not contain nitrogen. The ORR active catalyst was not obtained by heating DBP on Au(111).
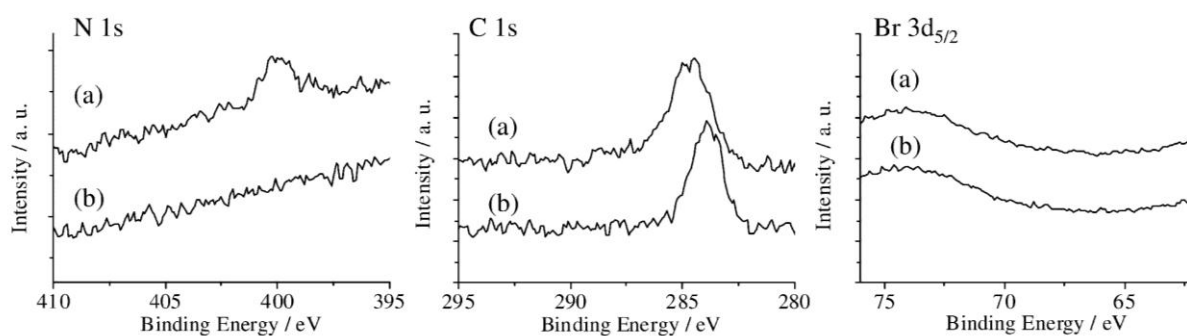

Figure 5-23. Narrow-scan XP spectra in N 1s, C 1s, and Br 3d$_{5/2}$ regions of (a) DBP and (b) heat treated DBP at 460ºC on Au(111).
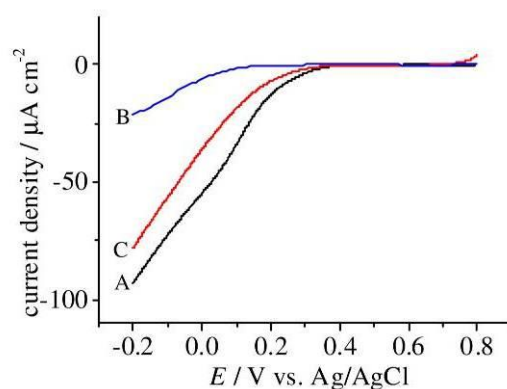
Figure 5-24. LSVs of bare Au(111) (black, A), Au(111) modified with DBP (blue, B) and (c) heat treated DBP on Au(111) at 460ºC in 0.1 M HClO$_4$ solutions saturated with O$_2$. Scan rate = 10 mV s^{-1}.

5.4   Conclusion

Nitrogen doped carbon materials, which consist of pyridine-like nitrogen, were prepared from pepy. XPS and Raman spectroscopy results showed that the nitrogen concentration decreased while the crystallinity of nitrogen doped carbon materials increased with heat treatment at higher temperatures. The ORR activity of pepy, especially in alkaline solution, improved with heat treatment. 600py and 700py,

104

which possessed higher nitrogen concentrations and higher crystallinity had higher ORR activity than 500py and 800py. RDE measurements showed that ORR on nitrogen doped carbon materials prepared from pepy proceeds by a two electron reaction. In addition, the layer of bromo group containing aromatic molecules was prepared on Au(111), and attempts were made to convert it to graphene structures, but the graphene ribbon structure was not observed. The STM, Raman, and XPS results showed that the molecules decomposed during heat treatment.

Reference

1.   L. T. Qu, Y. Liu, J. B. Baek and L. M. Dai, *ACS Nano*, 2010, **4**, 1321-1326.

2.   Y. F. Tang, B. L. Allen, D. R. Kauffman and A. Star, *J. Am. Chem. Soc.*, 2009, **131**, 13200-+.

3.   B. Stohr, H. P. Boehm and R. Schlogl, *Carbon*, 1991, **29**, 707-720.

4.   X. Q. Wang, J. S. Lee, Q. Zhu, J. Liu, Y. Wang and S. Dai, *Chem. Mater.*, 2010, **22**, 2178-2180.

5.   P. H. Matter, E. Wang, M. Arias, E. J. Biddinger and U. S. Ozkan, *J. Phys. Chem. B*, 2006, **110**, 18374-18384.

6.   P. H. Matter, L. Zhang and U. S. Ozkan, *J. Catal.*, 2006, **239**, 83-96.

7.   A. Pacula, K. Ikeda, T. Masuda and K. Uosaki, *J. Power Sources*, 2012, **220**, 20-30.

8.   K. P. Gong, F. Du, Z. H. Xia, M. Durstock and L. M. Dai, *Science*, 2009, **323**, 760-764.

9.   H. Niwa, K. Horiba, Y. Harada, M. Oshima, T. Ikeda, K. Terakura, J. Ozaki and S. Miyata, *J. Power Sources*, 2009, **187**, 93-97.

10.   R. Bashyam and P. Zelenay, *Nature*, 2006, **443**, 63-66.

11.   S. S. Lin and M. D. Gurol, *Environ. Sci. Technol.*, 1998, **32**, 1417-1423.

12.   W. Yang, T. P. Fellinger and M. Antonietti, *J. Am. Chem. Soc.*, 2011, **133**, 206-209.

13.   T. Iwazaki, R. Obinata, W. Sugimoto and Y. Takasu, *Electrochem. Commun.*, 2009, **11**, 376-378.

14.   T. Iwazaki, H. S. Yang, R. Obinata, W. Sugimoto and Y. Takasu, *J. Power Sources*, 2010, **195**, 5840-5847.

15.   C. D. Simpson, J. D. Brand, A. J. Berresheim, L. Przybilla, H. J. Rader and K. Mullen, *Chem. Eur. J*, 2002, **8**, 1424-1429.

16.   X. Y. Yang, X. Dou, A. Rouhanipour, L. J. Zhi, H. J. Rader and K. Mullen, *J. Am. Chem. Soc.*, 2008, **130**, 4216-+.

17.   L. J. Zhi and K. Mullen, *J. Mater. Chem.*, 2008, **18**, 1472-1484.

18.   J. M. Cai, P. Ruffieux, R. Jaafar, M. Bieri, T. Braun, S. Blankenburg, M. Muoth, A. P. Seitsonen, M. Saleh, X. L. Feng, K. Mullen and R. Fasel, *Nature*, 2010, **466**, 470-473.

19. M. Treier, C. A. Pignedoli, T. Laino, R. Rieger, K. Mullen, D. Passerone and R. Fasel, *Nature Chem.*, 2011, **3**, 61-67.

20. W. J. Gammon, O. Kraft, A. C. Reilly and B. C. Holloway, *Carbon*, 2003, **41**, 1917-1923.

21. A. C. Ferrari and J. Robertson, *Phys. Rev. B*, 2000, **61**, 14095-14107.

22. R. E. Davis, G. L. Horvath and C. W. Tobias, *Electrochim. Acta*, 1967, **12**, 287-&.

23. H. Naohara, S. Ye and K. Uosaki, *J. Phys. Chem. B*, 1998, **102**, 4366-4373.

24. X. Y. Li, R. S. Czernuszewicz, J. R. Kincaid, Y. O. Su and T. G. Spiro, *J. Phys. Chem.*, 1990, **94**, 31-47.

25. N. Nishimura, M. Ooi, K. Shimazu, H. Fujii and K. Uosaki, *J. Electroanal. Chem.*, 1999, **473**, 75-84.

26. F. M. Pan, P. C. Stair and T. H. Fleisch, *Surf. Sci.*, 1986, **177**, 1-13.

27. M. Xi and B. E. Bent, *J. Am. Chem. Soc.*, 1993, **115**, 7426-7433.

Chapter 6

GENERAL CONCLUSION AND FUTURE PROSPECT

In this thesis, noble metal based and metal-free based electrocatalysts were prepared from molecules by bottom-up methods and their structure and activity were characterized by scanning tunneling microscope (STM), X-ray photoelectron spectroscopy (XPS), X-ray adsorption fine structure (XAFS), Raman spectroscopy and electrochemical measurements.

In chapter 3, Pt-Ru alloys with various coverage were prepared by repeating Pt-Ru complex adsorption and heat treatment cycle on Au(111) surface and their activities for MOR, CO oxidation reaction, HOR and ORR were investigated. STM showed that Pt-Ru alloys with low coverage were monoatomic height. The surface coverage, size and height of Pt-Ru alloys were increased by repeating the cycle of Pt-Ru complex adsorption and heat treatment cycle on Au(111) surface. XPS showed that Pt-Ru complex was decomposed by the heat treatment at 300ºC under O_2 flow and Pt-Ru alloy composed of metallic Pt and RuO_2 was obtained. Pt-Ru alloy with a monoatomic height had no MOR activity in acidic but in alkaline solution. Pt-Ru alloys with a few atomic heights had MOR activity in acidic solution. Electrocatalytic activity of Pt-Ru alloy with high coverage prepared from Pt-Ru complex was compared with other electrodes. By repeating Pt-Ru complex adsorption and heat treatment cycle on Au(111) surface for 32 times, Pt-Ru alloy with higher MOR activity and durability than Pt-Ru alloy prepared from a mixture of K_2PtCl_4 and $RuCl_3$ was obtained. In alkaline solution, Au(111) modified with Pt showed higher MOR activity and durability than Pt-Ru alloy on Au(111) prepared from Pt-Ru complex. In alkaline solution, OH adsorption on Au probably accelerates MOR activity at Pt. CO stripping measurements were carried out to investigate CO tolerance of Pt-Ru alloy. The Pt-Ru alloy prepared from Pt-Ru complex showed poorer activity against CO oxidation reaction than Pt-Ru alloy prepared from the mixture of K_2PtCl_4 and $RuCl_3$ and poly Pt. RuO_2 in Pt-Ru alloy may be poisoned by CO and can not supply CO active oxygen species. The Pt-Ru alloy prepared from Pt-Ru complex showed higher ORR and HOR activity than the Pt-Ru alloy prepared from

108

the mixture of K_2PtCl_4 and $RuCl_3$, suggesting the difference of OH adsorption ability at Pt.

In chapter 4, XPS and Ru K edge XAFS measurements were performed to reveal the origin of enhancement of MOR activity and durability of Pt-Ru alloy prepared from Pt-Ru complex. XPS results showed that RuO_2 in Pt-Ru alloy prepared from the mixture of K_2PtCl_4 and $RuCl_3$ is similar to bulk RuO_2 but RuO_2 in the Pt-Ru alloy prepared from Pt-Ru complex has oxygen deficiency. Ru K edge XAFS measurements showed that the Ru–O distance of the Pt-Ru alloy prepared from Pt-Ru complex was longer than that of the latter, suggesting the presence of the weakly coordinated oxygen species, i.e., H_2O, in the Pt-Ru alloy prepared from Pt-Ru complex. H_2O coordinated to Ru can be an active oxidant, i.e., surface Ru–OH, under electrochemical conditions and enhance MOR activity and durability.

In chapter 5, nitrogen doped carbon materials which are expected to be metal-free ORR catalysts were prepared from organic molecules. In first example, nitrogen doped carbon materials were prepared form penta-2-(*p*-ethynylphenyl)-ethynylpyridine by the pyrolysis at various temperatures under Ar flow. XPS results showed that nitrogen doped carbon materials prepared from pepy consist of pyridine-like nitrogen. Nitrogen concentrations decreased as heat treatment temperature increased. Raman spectroscopy results showed that crystallinity of nitrogen doped carbon materials increased as heat treatment temperature increased. Penta-2-(*p*-ethynylphenyl)-ethynylpyridine heat treated at 600 and 700ºC under Ar flow with high nitrogen concentration and high crystallinity had high ORR activity. In second example, the preparation of graphene structures was tried by the heat-induced coupling and dehydrogenation reactions of polyaromatic molecules adsorbed on Au(111). Although an ordered molecular layer was prepared on Au(111) from 9,10-dibromoanthracene and 5,15-dibromo, 10,20-diphenylporphine, the ordered molecular layer was not converted to graphene ribbon structures. The STM, SERS, and XPS measurements showed that the molecules decomposed during heat treatment and the composites did not have high ORR activity.

In this thesis, electrocatalysts were prepared by bottom-up methods and characterized by various techniques. The careful analysis showed not only merits in preparing electrocatalysts by bottom-up methods but also problems of prepared electrocatalysts. Although Pt-Ru alloy with high MOR activity was

prepared from Pt-Ru complex on Au(111), the height and size of Pt-Ru alloy is heterogeneous. It is necessary to control the size of Pt-Ru alloy to improve the MOR activity of Pt-Ru alloy. Nitrogen doped carbon materials composed of pyridine-like C–N bonding configuration were prepared from penta-2-(*p*-ethynylphenyl)-ethynylpyridine. The studies on preparation of nitrogen doped carbon materials from polyaromatic molecules are limited. Novel molecules containing pyrrole and graphite-like nitrogen with large molecular weight should be synthesized and used as starting materials for preparation of nitrogen doped carbon materials. XPS and Raman results showed that not only nitrogen concentrations but also crystallinity of nitrogen doped carbon materials affects ORR activity. Development of new method to avoid nitrogen desorption at high temperature is required.